# Turbulent Convective Mass Transfer in Electrochemical Systems

by

François Gurniki

December 2000
Technical Reports from
Royal Institute of Technology
Department of Mechanics
S-100 44 Stockholm, Sweden

Typsatt i I $^{A}T_{E}X$ med KTH's thesis-style.
Akademisk avhandling som med tillstånd av Kungliga Tekniska Högskolan i Stockholm framlägges till offentlig granskning för avläggande av teknologie doktorsexamen fredagen den 1 december 2000 kl 10.15 i Kollegiesalen, Administrationsbyggnaden, Kungliga Tekniska Högskolan, Valhallavägen 79, Stockholm.
©François Gurniki 2000
Högskoletryckeriet, Stockholm 2000

# Turbulent Convective Mass Transfer in Electrochemical Systems

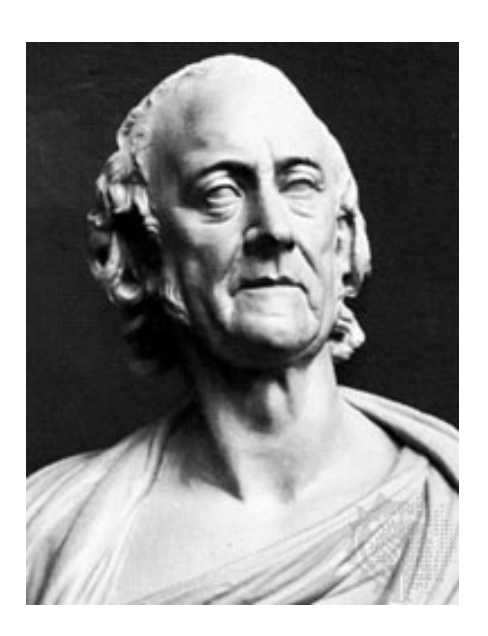
François Gurniki 2000

Department of Mechanics, Royal Institute of Technology S-100 44 Stockholm, Sweden

#### Abstract

Electrochemical mass transfer in turbulent flows and binary electrolytes is investigated. The primary objective is to provide information about mass transfer in the near-wall region between a solid boundary and a turbulent fluid flow at high Schmidt number. Natural and forced convections are investigated with two different methods; the turbulence model  $k - \epsilon$  and large-eddy simulations (LES). The  $k-\epsilon$  method does not solve the fluctuating part of the flow and assumes isotropic turbulence. LES solve only the large scales of the fluctuations. The computations made with natural convection reveal that the standard wall-functions give acceptable results for the velocity field, but not for the concentration. The Boussinesq approximation for the Reynolds-flux in the mass-transport equation and the wall-function for concentration in the logarithmic layer are shown to fail in the prediction of the turbulent mass transfer. A method for large-eddy simulations is developed to study the Reynolds-flux and mass-transfer in the near-electrode region. In order to make numerical integration of governing equations at high Schmidt number economic, a numerical scheme is developed in which two different meshes are used for hydrodynamic variables and the concentration field. With the help of a fringe technique the finest mesh used for the computation of mass transfer is reduced to the near-wall region only. A study of the electrical distribution along the electrode reveals that the intensity of the current influences the fluctuations of the concentration field but not the mean values in time. Some models for the Reynolds- flux validated for Sc=1 are successfully tested for Sc=3000. At high Schmidt number, a new model for the Reynolds-flux and a new wall-function for concentration are found.

**Descriptors:** electrolyte, mass transfer, turbulent channel flow, forced convection, natural convection, wall-functions, explicit algebraic modelling, large-eddy simulations.



 $\begin{tabular}{ll} Detail of a bronze bust of Volta~(1745-1827), professor of physics at the Royal \\ School of Como, Italy. \end{tabular}$ 

# Preface

This thesis considers passive scalar transport in turbulent flows. The thesis is based on the following papers.

- **Paper 1.** GURNIKI, F., ZAHRAI, S. & BARK, F. H. 1999 'Turbulent free convection in large electrochemical cells with a binary electrolyte' *Journal of Applied Electrochemistry* **29**, 27-34.
- **Paper 2.** GURNIKI, F., ZAHRAI, S. & BARK, F. H. 2000 'LES of turbulent channel flow of a binary electrolyte' *Journal of Applied Electrochemistry* **30**, 00-00.
- **Paper 3.** GURNIKI, F., ZAHRAI, S. & BARK, F. H. 2000 'Validation of the fringe region technique in LES of turbulent mass transfer at high Schmidt number' 3rd Int. Symp. on Turbulence, Heat and Mass Transfer April 2-6, Nagoya, Japan, **3**, 431-438.
- Paper 4. GURNIKI, F., ZAHRAI, S. & BARK, F. H. 2000 'Large-eddy simulation of electrochemical mass transfer' 4th Int. Conf. on Hydromagnetic Phenomena and Applications, Sept. 12-18, Giens, France, 1, 327-332.
- **Paper 5.** GURNIKI, F., ZAHRAI, S. & BARK, F. H. 2000 'On near-wall turbulent passive-scalar transfer at high Schmidt number', *submitted to Int. Journal of Heat and Mass Transfer*.
- **Paper 6.** GURNIKI, F. 2000 'On modelling of Reynolds-flux vector at high Schmidt number', submitted to Int. Journal of Heat and Mass Transfer.

The papers are here re-set in the present thesis format, and some minor corrections have been made as compared to published versions.

 $\mathbf{v}$ 

# Contents

Chapter 1. Introduction  Chapter 2. Electrochemical mass transfer 2.1. Governing equations 2.2. Mass fluctuations near the electrodes	1 4 6 9 12 13 14
<ul><li>2.1. Governing equations</li><li>2.2. Mass fluctuations near the electrodes</li></ul>	6 9 12 13
2.2. Mass fluctuations near the electrodes	9 12 13
	12 13
	13
Chapter 3. Turbulent mass transfer	
3.1. Sherwood number in forced convection	14
3.2. Sherwood number in natural convection	
Chapter 4. Turbulence models	16
4.1. Governing equations	16
4.2. The Boussinesq approximation	17
4.3. The wall-function problem	18
4.3.1. Limitation of the standard assumption	20
4.3.2. Limitation of the Kader assumption	21
4.3.3. An alternative wall-function for mass	23
4.4. Algebraic Reynolds stress models	25
Chapter 5. Large-eddy simulation	27
5.1. Subgrid-scale model	28
5.2. Discretization and mesh systems	31
5.3. The fringe region technique	34
Chapter 6. Summary of papers	37
Chapter 7. Outlook and critical review	42
${ m Acknowledgments}$	43
Bibliography	44
Paper 1. Turbulent free convection in large electrochemical cells with a binary electrolyte	49

Paper 2.	LES of turbulent channel flow of a binary electrolyte	69
Paper 3.	Validation of the fringe region technique in LES of turbulent mass transfer at high Schmidt number	87
Paper 4.	Large-eddy simulation of electrochemical mass transfer	99
Paper 5.	On near-wall turbulent passive-scalar transfer at high Schmidt number	107
Paper 6.	On modelling of Reynolds-flux vector at high Schmidt number	129

## Introduction

Electrochemistry is involved to a significant extent in the today's industrial economy. Examples are found in batteries, fuel cells or capacitors, for electric vehicles, portable devices or industrial productions of chemicals; in the production of chlorine, caustic soda, aluminium; in electroplating, electromachining, and electrorefining; and in corrosion. There are three significant types of power sources which produce electricity by reaction within electrochemical cells. The two types which use reactants stored within them are called primary cells and secondary cells. Groups of primary or secondary cells are called batteries, although the term battery has been extended to include also a single cell used as a power source. Secondary cells, unlike primary cells, can be driven in reverse or charged by external electrical power. The third type, fuel cells, employ reactants which are continuously supplied to the cell; products are also continuously removed. In primary and secondary cells, the reactants and products are contained within the cell.

The first steps in electrochemistry were made by Luigi Galvani who attributed in 1791 twiching of detached frog legs to animal electricity. The same year, Alessandro Volta asserted that the frog legs twitched because different metals brought into contact via a liquid produced electricity. In 1800, Volta built his first Voltaic pile. Thirty years later, Faraday established that the amount of chemical change is proportional to the quantity of electricity passed, and that for the same quantity of electricity the amounts of different substances deposited or dissolved are proportional to their chemical weights. He introduced the terms cathode, anode, electrode, ion, cation, anion, and electrolyte. Later in 1901, Thomas A. Edison and Waldemar Jungner invented the first alkaline rechargeable batteries. Finally, in 1977, Alan MacDiarmid and Alan Heeger discovered the electrical conductance of polyacetylene, leading to the construction with David MacInnes in 1981 of the first battery with no metallic constituents [1].

An important aspect of electrochemistry is the mass transfer taking place in the electrolyte and at the electrodes of electrochemical cells. The efficiency of the cell is highly dependent on the distribution of chemical reactants in the vicinity of these electrodes. One difficulty is to predict correctly the distributions of concentrations, that are, in most of the flows present in electrolytes, turbulent. Turbulence can be regarded as a particular state of a fluid in movement in which the flow fluctuates rapidly in time and space [2]. These fluctuations have already

1

been statistically studied, but many unknowns remain. In particular, it is today not well understood how the fluctuations vary in time and space at the electrodes or in the near-electrode region. In this region, not even the mean concentration field in time is well-known [3].

Some properties of the mass fluxes near the electrodes constitute an obstacle for their study. Here, it is important to introduce the concept of boundary layer for mass transport. The thickness of the boundary layer for temperature along a flat heating plate, also called the conductive boundary layer, is defined by Bejan [4] as the length-scale of a slender region adjacent to the wall, where the heatconduction phenomenon is at least as important as convection in the equation of transport. Since this equation is identical for mass transport, the same definition can used, where conductivity is replaced by diffusivity. In a channel flow, this definition is not relevant any longer because diffusion plays an important role everywhere. It remains neverthess a useful concept, because it is used to determine the relative thickness of the diffusive boundary layer,  $\delta_c$ , compared to the hydrodynamical,  $\delta_h$ . Levich [5], based on the analogy with laminar boundary layer, proposed that in a turbulent boundary layer the thickness of the diffusive layer would be of the order of magnitude of  $\delta_h \cdot Sc^{-1/3}$ . It has been verified experimentally in different studies, for example by Lin et al. [6]. Sc is here the Schmidt number, or the ratio between the diffusivity coefficient for mass and the viscosity of the fluid. Using this relation, it is consequently possible even in the near-wall region of a channel to give an approximation in viscous units of the diffusive,  $5 \cdot Sc^{-1/3}$ , and the logarithmic,  $(30-100) \cdot Sc^{-1/3}$ , sublayers in the diffusive boundary layer.

The high value of Schmidt number appearing in most of the practical electrochemical applications is one of the important factors resulting in thin diffusive boundary layers, and making experimental investigations of flows with mass transfer problematic. Unfortunately, although electrochemical systems seem to be suitable for experimental investigations, see e.g. [7], the measured data are usually in the form of integrated quantities rather than detailed information on the structure of the flow and its fluctuations in time and space. As examples, Fouad et al. [8] and Newman [9] studied mass transfer in electrochemical systems and reported global information on the process such as the total cell potential drop, the electrical current and the global density variation of ionic species. As a result, other tools must be used in order to provide detailed data on the structure of the flow. With improvement of digital computers and computational methods during the past years, computational simulations can today be used as an alternative to physical experiments.

This thesis is a study of mass transport in turbulent flows of electrochemical cells. The investigation is performed through numerical simulations. The mathematical models account both for turbulence and the properties of electrochemical mass transfer. Different models are tested for the electrochemical process at the

electrodes. Natural and forced convection are investigated. The electrolyte considered is binary. The transport equations for mass are consequently reduced to one equation only, and is identical to the transport equation for a passive scalar, or temperature. No volume reaction is considered. The major contribution of this work is the validation of a numerical method to compute turbulent mass transfer in near-electrode regions. A class of turbulence models with a fairly simple formulation is validated for electrochemical processes.

# Electrochemical mass transfer

The Swedish chemist Svante Arrhenius was the first to use the term electrolyte to describe a salt which in solution dissociates into ions. An ion is an atom or molecule which has acquired an electrical charge. An ion which carries a positive charge is called a cation and an ion which carries a negative charge is called an anion. Compounds, molecules, and atoms which are uncharged are referred to as neutral species. A solution which contains ions is called an electrolyte solution (sometimes simply an electrolyte). Electrolyte solutions conduct electricity because the charged ions can move through them. Electrolyte solutions are ionic conductors as distinguished from the electronic conductors, such as metallic wires, in which charge is carried by movement of electrons. An electrolyte solution may be used for this purpose alone. An example of this is the salt bridge, which electrochemists use to permit the flow of ionic charge between different electrolyte solutions. A salt bridge is a tube containing a relatively high concentration of an ionic salt such as potassium chloride. The electrolyte solution of the salt bridge may be held as a semisolid agar gel to make it easier to use.

Electrochemical cells are used in several industrial applications, such as copper refining cells and lead-acid batteries. In a copper refining cell, the anode is made up of raw copper, with small amounts of impurities while the cathode is made of highly purified copper. The electrolyte is an aqueous solution of copper sulphate with some added sulfuric acid, in order to reduce the ohmic losses of the process. During the purification process, the passage of electric current causes the copper ions to be dissolved at the anode and deposited onto the cathode, to form highly purified mass of copper. In lead-acid batteries, the positive electrode,  $PbO_2$ , and the negative electrode, Pb, are separated by a solution of sulfuric acid. During discharge, sulfuric acid is consumed and water is produced. Dilute acid close to the electrodes rises and the heavy acid in the bulk sinks. During recharge the process is reversed. Current conduction from the electrodes to the electrolyte in electrochemical cells takes place, due to chemical reactions, usually limited to a very thin sheath at the surface of the electrodes, and thereafter due to transport of ions in the bulk of the electrolyte. Positive ions are produced in the anodic sheath and, after transport through the electrolyte, are neutralized in the cathodic sheath. Diffusion, migration and convection are the main transport mechanisms through the electrolyte.

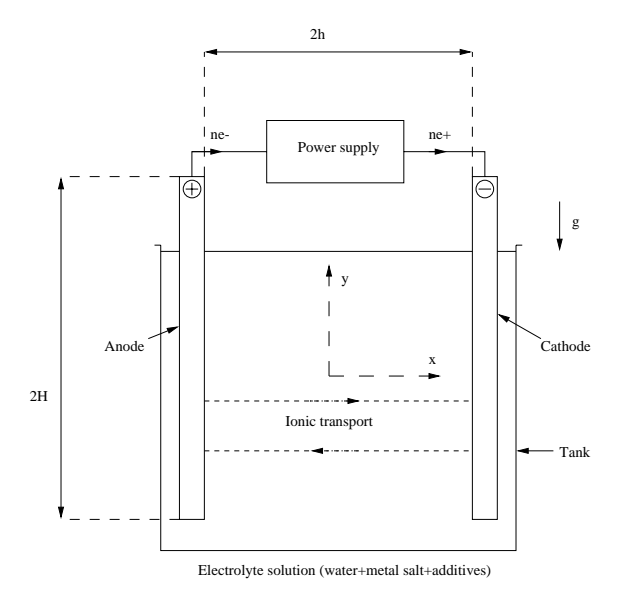


FIGURE 2.1 The geometry of the cell and the chosen coordinate system.

It turns out that between the different transport mechanisms mentioned above, the convection process is the most efficient in most applications. In this section, the mathematical formulation of electrochemical mass transfer is presented for a binary electrolyte in an electrochemical cell. More complex geometries are present among the industrial applications, but a simple geometry is enough to describe the basic concepts of electrochemical mechanisms.

Two electrodes made from the same metal are immersed in a dilute solution of a salt of the electrode metal providing a binary electrolyte in a rectangular cell. The cell, which is assumed to have its sides parallel to the direction of gravity, is shown in figure 2.1. If the cell is closed, as it is shown in figure 2.1, the convection in the cell is purely natural. If the cell is open at its bottom and its top, it can be seen as part of a vertical channel flow, and convection can be forced. The dissolution of metallic ions generally increases the density of the fluid near to the anode. Near the cathode, the reverse reaction takes place resulting in a lower density. Inhomogeneities in the density field set the fluid in motion with a convection pattern downwards near the anode and upwards near the cathode. Natural convection, which is driven by the chemical reactions at the electrodes, contributes to transport of ions and thereby influences the chemistry of the cell. In a case of strongly forced convection, the phenomenon of density variations can be usually neglected.

#### 2.1. Governing equations

Since the considered electrolyte is binary, the mathematical description concerns the transport of a metallic cation and its corresponding anion. All the equations presented below describe the behaviour of instantaneous variables. In a two-dimensional configuration, the hydrodynamic problem must be solved for 6 dependent variables: the concentrations  $c_1$  and  $c_2$ , where subscript 1 denotes the anion, and subscript 2, the corresponding cation, the velocity field,  $\mathbf{u}=(u,v,0)$ , the pressure field, p and the electrical potential,  $\phi$ . Apart from the very thin sheaths, called double layers, and adjacent to the electrodes, the electrolyte can be assumed to be electrically neutral, that is

$$z_1 c_1 + z_2 c_2 = 0, (1)$$

where z denotes the charge number of the species and the indices 1 and 2, the metallic and the non metallic ionic species, respectively. If the double layer is not to be explicitly accounted for, the mathematical problem can be formulated using a single variable for the concentration fields by defining

$$c = z_1 c_1 = -z_2 c_2, (2)$$

which satisfies the neutrality condition (1). The governing equation for c will then be read

$$\frac{\partial c}{\partial t} + \mathbf{u} \cdot \nabla c = D\Delta c,\tag{3}$$

where the positive quantity D is the salt diffusivity for the electrolyte and is related to mass diffusivity coefficients for species 1 and 2, according to

$$D = \frac{(z_1 - z_2)D_1D_2}{z_1D_1 - z_2D_2}. (4)$$

Here attention is restricted to systems where  $z_1 = -z_2 = 2$ , resulting in a salt diffusivity coefficient of

$$D = \frac{2D_1 D_2}{D_1 + D_2}. (5)$$

For an incompressible electrolyte, the velocity field satisfies

$$\nabla \cdot \mathbf{u} = 0. \tag{6}$$

Using equation (2), the equation of Navier-Stokes for an incompressible fluid in a gravitational field under Boussinesq approximation, is

$$\rho \frac{\partial \mathbf{u}}{\partial t} + \rho \mathbf{u} \cdot \nabla \mathbf{u} = -\nabla p + \mu \Delta \mathbf{u} - \beta' \rho g(c - c_o) \mathbf{e}_y, \tag{7}$$

where  $\rho$  and  $c_o$  denote the density of the electrolyte and the reference concentration, respectively.  $\beta'$  is the total volume expansion factor.  $\mu$  is the dynamic viscosity of the electrolyte,  $\mathbf{g}$  the gravitational acceleration and  $\mathbf{e}_y$  is the unit vector in the vertical direction.

A conservation equation for the electric potential must then be added to the conservation equations for momentum and mass, in order to have a set of well-posed equations. As mentioned above, the electrolyte is assumed to be electrically neutral resulting in a divergence-free current density everywhere in the cell. This can be used to obtain the governing equation for the electric potential,  $\phi$ . The total electric current density, which is the sum of the contributions from each species, can be written according to Faraday's law

$$\mathbf{i} = F \sum_{i=1}^{2} z_i \mathbf{N}_i, \tag{8}$$

where F is Faraday's constant,  $\mathbf{N}_i$  denotes the mass flux of the species i, and is equal to a sum with contributions from migration of charged species in the electric field, diffusive fluxes and convective fluxes related to different field variables, according to

$$\mathbf{N}_{i} = -\frac{z_{i}FD_{i}}{RT}c_{i}\nabla\phi - D_{i}\nabla c_{i} + c_{i}\mathbf{u}.$$
(9)

In the above formula, R and T denote the gas constant and the temperature field, respectively. After substitution of  $N_i$  by (9) in (8), and setting the divergence of (8) to zero, one finds

$$\frac{F\Gamma}{RT}\nabla \cdot (c\nabla\phi) + \nabla^2 c = 0, \tag{10}$$

where  $\Gamma = \frac{2(D_1 + D_2)}{D_1 - D_2}$ .

Boundary conditions must be specified for velocity, pressure, concentration and the electric potential. They form with the set of equations (3), (6), (7) and (10), a well-posed system that can be solved. Figure 2.2 shows the numerical prediction of the electric potential field in a closed cell and a laminar case.

For the velocity field the no-slip condition is to be applied on all four walls, if the cell is closed

$$\mathbf{u} = \mathbf{0} \text{ at } x = \pm h \text{ and } y = \pm H. \tag{11}$$

If convection is forced, a gradient can be prescribed for the mean pressure in the channel.

All chemical reactions take place in close vicinity to the surface of electrodes, that is in the double layers. Inside the double layers, which have a thickness of the order of 1 nm, electroneutrality is not valid but regions with free charges can be expected. The existence of free charges results in a fast variation of the electric potential over the thickness of the layers, see figure 2.3.  $\phi_m^A$  and  $\phi_s^C$  correspond to the electric potential before and after the double layer, respectively. The variation of the potential difference E can be seen as the driving force for electron transfer across the double layer. This variation is responsible for the current intensity at the electrode. As Bark and Alavyoon [10] did, the present



Figure 2.2 The iso-contours of the electric potential in an enclosed electrochemical cell. Calculations performed with CFX of a laminar case.  $-7.0 \cdot 10^{-2} \ V \le \Phi \le +7.0 \cdot 10^{-2} \ V$ .

study uses a semi-empirical Butler-Volmer law to model this driving force and the concentration gradient at the electrodes

$$\frac{\mathbf{e}_{x} \cdot \mathbf{i}}{2FD_{1}} = \begin{cases}
\frac{i_{0}}{2FD_{1}} \left[ e^{\frac{n\alpha_{a}F(V_{+} - \phi)}{RT}} - \frac{c}{c_{o}} e^{-\frac{n\alpha_{c}F(V_{+} - \phi)}{RT}} \right] & \text{at } x = -h \text{ (anode)} \\
\frac{i_{0}}{2FD_{1}} \left[ \frac{c}{c_{o}} e^{\frac{n\alpha_{c}F(\phi - V_{-})}{RT}} - e^{-\frac{n\alpha_{a}F(\phi - V_{-})}{RT}} \right] & \text{at } x = +h \text{ (cathode)}
\end{cases}$$
(12)

where  $n=\|z_1\|$  and  $\mathbf{e}_x$  is the unit vector in the horizontal direction.  $i_o$  is the exchange current density,  $V_\pm$  the electrode potentials, and  $\alpha_{a,c}=0.5$  the transfer coefficients.

A a simpler condition, which was proposed by Ziegler  $et\ al.$  [11], has also been used

$$\frac{\mathbf{e}_x \cdot \mathbf{i}}{2FD_1} = -\frac{\partial c}{\partial x} = \text{constant.} \tag{13}$$

If the cell is closed, no transfer of mass occurs at the horizontal walls, resulting in vanishing normal derivatives of the concentration field

$$\frac{\partial c}{\partial y} = 0 \text{ at } y = \pm H.$$
 (14)

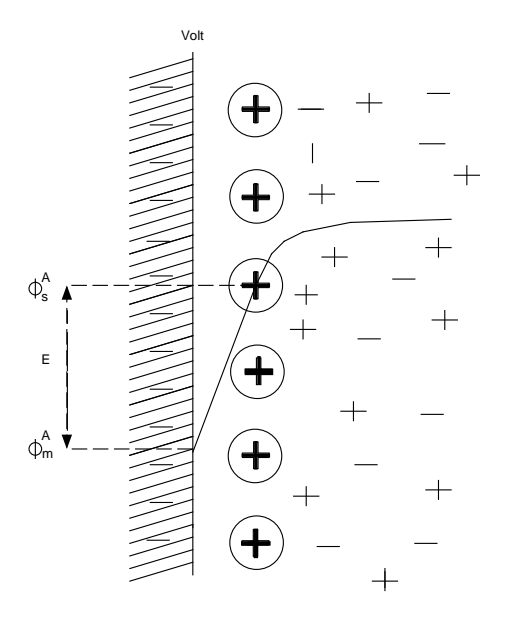


FIGURE 2.3 The double layer and variation of electric potential at the interface electrode-electrolyte.

Otherwise, the gradient for the equivalent concentration in many cases, can be set proportional to the concentration.

$$\frac{\partial c}{\partial y} = K_o \left( c - c_o \right) \text{ at } y = \pm H. \tag{15}$$

For the electric potential, because  $\mathbf{N}_2 \cdot \mathbf{e}_x = \mathbf{0}$  at  $x = \pm h$ , one finds

$$\frac{\partial \phi}{\partial x} = \frac{RT}{2Fc} \frac{\partial c}{\partial x} \text{ at } x = \pm h, \tag{16}$$

At the horizontal walls, since no chemical reaction takes place, one finds

$$\frac{\partial \phi}{\partial y} = 0 \text{ at } y = \pm H. \tag{17}$$

#### 2.2. Mass fluctuations near the electrodes

As mentioned above, major interest is shown for fluctuations of mass transfer at the electrodes of an electrochemical cell, because they influence the current distribution in the cell. Fluctuations in the concentration field are induced by the velocity field. In a previous study, Robinson et al. [12] concluded that the majority of the turbulence production in the entire hydrodynamical boundary layer occurs in the buffer region during outward ejections of low-speed fluid and during inrushes of high-speed fluid [12]. Sweeps (v < 0) and ejections (v > 0) are defined there by a negative local product of streamwise and wall-normal velocity fluctuations. The present study adopts here the same definitions.

An important characteristic of turbulent mass transfer at high Schmidt number is the influence of turbulence on the local mass transfer at the wall. So far, no clear direction or pattern has been identified for the fluctuating part of the mass flux in the diffusive sublayer. It is therefore necessary to find a detection criterion to discuss the influence of turbulence on electrode-mass-transfer. The present study considers here a case of forced convection in a electrochemical cell working as a three-dimensional channel flow, as it has been studied in all the papers except in paper 1. The reader is referred to one of these for the geometry. The walls of the channel are infinite (x-z) planes, periodic in the streamwise (x) and the spanwise (z) direction, and are the electrodes of the cell.

Sweeps and ejections in the buffer region of the hydrodynamical boundary layer are used here to detect the location of turbulence production. They can be characterized by a high level of wall-normal velocity fluctuations in absolute value. The present study uses a conditional sampling technique to determine the location of these events. Once these locations have been recorded, their positions in a (x-z) section are compared with the (x-z) positions of the detected large electrode-mass-transfer fluctuations. The two detections are made in the instantaneous field, at the same time, and at two different constant-y-surfaces. Figure 2.4 shows the averaged variance in space of the wall-normal velocity fluctuations, at  $y^+ = 12.74$  in the buffer region of the hydrodynamical boundary layer. This variance can be seen as the contribution of the wall-normal velocity to the instantaneous kinetic energy. The variance signal is calculated with a spatial counterpart (VISA technique) to the VITA technique used by Blackwelder et al. [13], that was validated by Johansson et al. [14]. The spatial averaging lies over a surface with a streamwise length of  $L^+=212$  and a spanwise length of  $L^{'+}=35.3$ , in viscous units. The VISA variance signal is then nondimensionalized by the square RMS intensity of the wall-normal velocity. The detection criterion is completed by using a threshold k equal to 1. Detection is triggered when the VISA variance signal exceeds k. Figure 2.4 shows also the fluctuating part of the wall-mass-transfer at the same (x-z) positions. The turbulent wall-mass-transfer is non-dimensionalized by the dimensionless mass transfer coefficient predicted at Schmidt number equal to 100 by Papavassiliou et al. [15]. A threshold k' is also used and is taken equal to 0.2.

At Sc=100, there seems to be a certain spatial correlation between high levels of VISA detected wall-normal velocity variance, and large wall-mass-transfer fluctuations, as shown in figure 2.4. This suggests that the fluctuations of the current density at the electrodes, which are proportional to the fluctuations of the concentration gradient [16], is correlated to the turbulence production events lying in the buffer region of the hydrodynamical boundary layer. Still, this result remains unsettled and should be investigated more intensively.

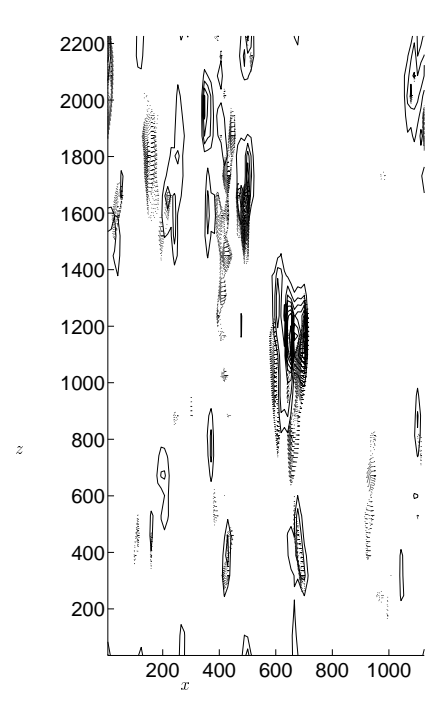


Figure 2.4 Sc=100 and in a (x-z) plane at  $y^+=12.74$ . Solid lines: The snapshot contour plots of the VISA-detected wall-normal velocity variance (detected with  $L^+=212$ ,  $L^{'+}=35.3$  and k=1.0). The increment in variance signal is 2. Dashed lines: The snapshot contour plots of the dimensionless concentration-gradient fluctuations at the wall, detected with  $k^{'}=0.2$ . The increment in concentration gradient is 0.01.

In paper 4, the study of frequencies of the electrode-mass-transfer confirmed the result of a previous study [17], showing that only low frequency velocity fluctuations were effective in causing concentration fluctuations. The spectra mass transfer was there shown to be proportional to the spectra for wall-normal velocity at the lowest frequencies. This result is not in contradiction with the typical timescale of turbulent production reported by McComb [18], and approximately equal to  $0.3 \cdot Re_{\tau}$  in viscous units, which is shown experimentally to correspond to the the lowest frequencies.

#### CHAPTER 3

## Turbulent mass transfer

Although numerous analytical and empirical methods have been developed for predicting rates of mass transfer in turbulent flows, a thorough understanding of the fundamental transfer mechanism is still very necessary for the design of various kinds of industrial processes [19], especially for electrochemical processes.

As shown by Colburn [20] and Sherwood [21], the processes of mass transfer and heat transfer are similar, and hence several theoretical principles treated previously for heat transfer may be regarded as applicable to mass transfer. The analogy between momentum and mass transfer was first deduced by Reynolds [22], postulating similarity between momentum exchange and material exchange. Unfortunately, it is only correct when Schmidt number is around one. Prandtl [23] and Taylor [24] later extended the analogy to include a laminar layer near the wall for mass transfer at all values of Schmidt number. For turbulent flows, von Kármán [25], Boelter et al. [26], and Reichardt [27] analyzed the problem more extensively on the basis of velocity distribution measurements in straight tubes. They found that the fluid is divided into three layers; namely, the very thin viscous sublayer adjacent to the wall, the turbulent core, and the buffer region between the core and the viscous sublayer. In the viscous sublayer, in which turbulence or the eddy diffusivity is small, material is transferred mainly by molecular motion. The velocity distribution and mass transfer in the turbulent core are controlled by eddy diffusivities of momentum and mass. In the buffer region, the combined action of molecular and eddy diffusivity determines velocity and mass transfer. The mathematical formulation of the buffer region in the diffusive boundary layer is necessary for predictions of mass transfer and of the distribution of chemical species near the electrodes. Unfortunately, at high Schmidt number the diffusive boundary layer is so thin that no data has so far been derived from experiments.

An aspect of turbulent mass transfer in electrochemistry, is the fluid flow conditions within an electrolyte. The fluid flow controls the magnitude and uniformity of mass transport of reactant species at the electrodes. It also promotes exchange of species between the bulk solution and the surface layers. Fluid motion is driven by the influence of a pressure gradient and diffusion. Two cases may be distinguished. Natural or free convection occurs when local variations in fluid density produce acceleration [28]. Forced convection is driven by the application of mechanical energy (as in the case of electrode movement), or by

the consumption of energy in a system (as in the case of a pressure drop through a pipe). Buoyancy-induced flows are complex because of the essential coupling between the flow and transport. The problems can be classified as either external or internal. It was pointed out by Ostrach [29] that internal problems are considerably more complex than external. The interactions between the boundary layer and the core constitute a central problem that has remained unsolved and is inherent to all confined convection configurations. In fact, the situation is even more intricate because it often appears that more than one global core flow is possible and flow subregions, such as cells and layers, may be imbedded in the core. This matter, which has been discussed more fully by Ostrach [30], is not merely a sublety for analysis, but has equal significance for numerical and experimental studies.

When there is the possibility of free convection superimposed on forced convection, the situation becomes essentially more complicated. Fortunately, it appears that one effect or the other predominates in the mass-transfer process, depending on the values of the Reynolds number, Re, and Rayleigh number, Ra. Ra is the non-dimensional ratio between forces of buoyancy and of viscosity. At horizontal electrodes, Tobias and Hickman [31] find that free convection predominates. Otherwise, forced convection does. Acrivos [32] has analyzed the combined effect of free and forced convection for surfaces that are not horizontal and found that the transition region between predominance of free and forced convection is usually narrow.

#### 3.1. Sherwood number in forced convection

Turbulent flow is characterized by rapid fluctuations of velocity, pressure, and concentration about their average values. Electrochemists usually are interested in these fluctuations only in a statistical sense. Forced convection in electrochemical systems has been extensively studied through experimental data in order to draw some generalization about the behaviour of the turbulent mass-transfer at the wall. It is dependent on the fluctuations in the near-wall-region and its importance can be justified by the fact that, as shown earlier in equation (13), the current distribution along the electrodes is directly proportional to the wall-mass-transfer. At Schmidt numbers greater than 0.5, Bejan [4] and Walsh [28] agree to consider the averaged non-dimensional wall-mass-transfer, the Sherwood number, as a function of the Reynolds number, Re, and Sc

$$Sh = 0.037Re^{4/5}Sc^{1/3}. (18)$$

Walsh found the coefficient of proportionality equal to 0.023. This difference can be due to the fact that Bejan considered a single plate along which a boundary layer had developed, when Walsh considered two parallel plates of an electrochemical cell working as a channel flow.

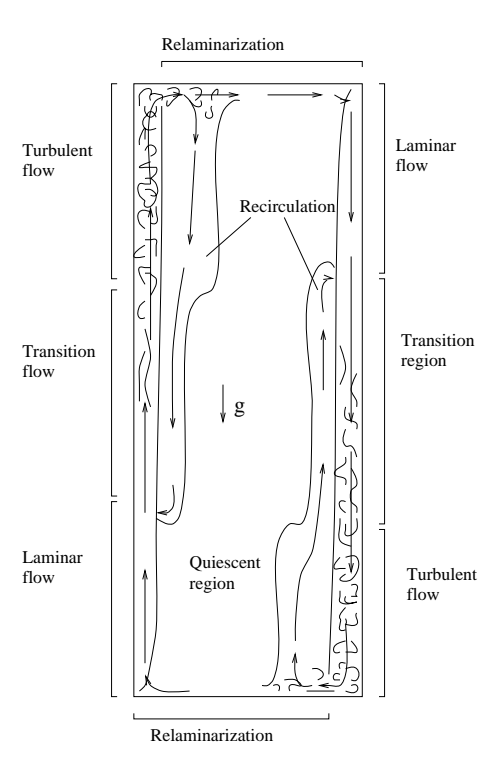


FIGURE 3.1 Schematic sketch of flow regions in an electrochemical cell.

#### 3.2. Sherwood number in natural convection

Natural convection in a two-dimensional cavity is one of many examples of turbulent flows whose geometrical simplicity conceals the full complexity of the real flow pattern. In spite of significant practical importance in many engineering applications and numerous research reports in literature, the problem has not been fully understood yet. There are still no reliable models or correlations which can be used with certainty for the prediction of mass transfer in cavities, in particular if the conditions are non-standard. A common practice to establish experimentally the wall-mass-transfer in form Sh = f(Ra, Sc) has so far not produced a consensus even for simple cases. Walsh [28] found Sh proportional to  $Ra^{0.28}$ , but Kitamura et al. [33] defined different zones in the hydrodynamic boundary along the electrodes of the cell where the turbulence intensities are not the same. As shown in figure 3.1, the flow is turbulent only in a small part of the vertical boundary layers. In the present cell, the electrodes are vertical, and generate in their vicinities density variations that create a circulation. In the turbulent flow, Kitamura found for the Sherwood number the following law

$$Sh = Ra^{1/4} + 37. (19)$$

The exponent was found to be equal to 1/5 in the transitional zone near the turbulent zone. These results are in good agreement with the law of dependency in the Rayleigh number for the Sherwood number, found in paper 2, where the exponent Ra was predicted equal to 1/5 in the transitional zone.

### Turbulence models

#### 4.1. Governing equations

The governing equations for an incompressible turbulent flow of a viscous fluid are the Navier-Stokes equations and the continuity equations (equations (6) and (7) in chapter 2.1)

$$\frac{\partial \tilde{u}_{i}}{\partial t} + \tilde{u}_{j} \frac{\partial \tilde{u}_{i}}{\partial x_{j}} = -\frac{1}{\rho} \frac{\partial \tilde{p}}{\partial x_{i}} + \nu \frac{\partial^{2} \tilde{u}_{i}}{\partial x_{i}^{2}} - \beta' g(\tilde{c} - c_{o}) \delta_{iy}$$
 (20a)

$$\frac{\partial \tilde{u}_i}{\partial x_i} = 0 \tag{20b}$$

where  $\tilde{u}_i$ ,  $\tilde{c}$  and  $\tilde{p}$  are the instantaneous velocity, concentration and pressure fields. The y-direction is considered here as the direction of gravitation. The Reynolds decomposition is defined as following;  $\tilde{u}_i = U_i + u_i$ ,  $\tilde{c} = C + c$  and  $\tilde{p} = P + p$ , where  $U_i$  and  $u_i$  are the mean and the fluctuating part of the velocity field, C and c are the mean and the fluctuating part of the concentration field, and P and p are the mean and the fluctuating part of the pressure. The mean variables are here time-averaged. Note that  $U_i$  can also be written  $\overline{u}_i$ ,  $C = \overline{c}$ , and  $P = \overline{p}$ . The Reynolds averaged Navier-Stokes equations are formed by taking the mean of the Navier-Stokes equations using the decomposition defined above

$$\frac{DU_{i}}{Dt} = -\frac{1}{\rho} \frac{\partial P}{\partial x_{i}} + \frac{\partial}{\partial x_{i}} \left( 2\nu S_{ij} - \overline{u_{i}u_{j}} \right) - \beta'(C - c_{o})\delta_{iy}$$
 (21a)

$$\frac{\partial U_i}{\partial x_i} = 0, \tag{21b}$$

where the mean strain rate tensor  $S_{ij} = (U_{i,j} + U_{j,i})/2$ . The notation  $D/Dt = \partial/\partial t + U_j \partial/\partial x_j$  is used to denote the rate of change following the mean flow. The term  $-\rho \overline{u_i u_j}$  is known as the Reynolds stress tensor and originates from the non-linear term of (20a). This tensor is responsible for the so called closure problem, because it creates extra unknowns that cannot be computed. If one considers the transport equations for these unknowns, new unknowns will appear as higher correlation terms for velocity components, so that it is not possible to obtain a closed set of equations.

The transport equations for the Reynolds stresses may be derived from the Navier-Stokes equations

$$\frac{\overline{Du_{i}u_{j}}}{Dt} = -\overline{u_{i}u_{l}}\frac{\partial U_{j}}{\partial x_{l}} - \overline{u_{j}u_{l}}\frac{\partial U_{i}}{\partial x_{l}} + \frac{\overline{p}}{\rho}\left(\frac{\partial u_{i}}{\partial x_{j}} + \frac{\partial u_{j}}{\partial x_{i}}\right) - 2\nu\frac{\overline{\partial u_{i}}}{\partial x_{l}}\frac{\partial u_{j}}{\partial x_{l}} \\
- \frac{\partial}{\partial x_{l}}\left(\overline{u_{i}u_{j}u_{l}} + \frac{\overline{p}}{\rho}\left(u_{i}\delta_{jl} + u_{j}\delta_{il}\right) - \nu\frac{\partial}{\partial x_{l}}\left(\overline{u_{i}u_{j}}\right)\right) \\
- \beta'g\overline{c(u_{i}\delta_{jy} + u_{j}\delta_{iy})}.$$
(22)

The first two terms on the right hand side are production due to mean field gradients. They are explicit in  $\overline{u_i u_j}$ , whereas the other terms need to be modelled. The next two terms are the pressure-strain correlation and viscous destruction. The next term is a diffusion term containing both turbulent and molecular diffusion. The first two terms inside the parenthesis of the diffusion term is the turbulent transport flux. The divergence of this flux is the rate of spatial redistribution among the different Reynolds stress components due to inhomogeneities in the flow field [2]. The last term is the contribution of free advection to turbulence.

In turbulent flows with mass transport, a velocity-concentration correlation  $\overline{u_ic}$  appears in the governing Reynolds averaged equation. Using the Reynolds decompositions for the velocity and the concentration, equation (3) becomes

$$\frac{\partial C}{\partial t} + U_j \frac{\partial C}{\partial x_j} = \frac{\partial}{\partial x_j} \left( D \frac{\partial C}{\partial x_j} - \overline{u_i c} \right). \tag{23}$$

The mass flux term  $\overline{u_ic}$ , or Reynolds-flux term in analogy with the Reynolds stress, is due to the non-linear advection term in equation (3) and leaves (23) unclosed. The transport equation for the turbulent mass-flux is given by

$$\frac{\overline{Du_ic}}{Dt} = -\overline{u_iu_l}\frac{\partial C}{\partial x_l} - \overline{u_lc}\frac{\partial U_i}{\partial x_l} + \overline{\frac{p}{\rho}}\frac{\partial c}{\partial x_i} - (D+\nu)\overline{\frac{\partial c}{\partial x_l}}\frac{\partial u_i}{\partial x_l} - \frac{\partial c}{\partial x_l}\overline{\frac{\partial c}{\partial x_l}} - D\overline{\frac{\partial c}{\partial x_l}}\overline{\frac{\partial c}{\partial x_l}} - D\overline{\frac{\partial c}{\partial x_l}}\overline{\frac{\partial c}{\partial x_l}}$$

$$-\beta' g\overline{c^2}\delta_{iy}. \tag{24}$$

The right hand side of the transport equation (24) contains two production terms due to mean field gradients, a pressure scalar-gradient correlation term, viscous and diffusive destruction, a transport term consisting of turbulent and molecular diffusion and a free convection contribution.

#### 4.2. The Boussinesq approximation

The analogy between the viscous stress generation caused by fluctuations on the molecular level and the generation of turbulent stresses caused by macroscopic velocity fluctuations leads to an eddy-viscosity formulation for the Reynolds stresses. The first attempt in that direction was made by Boussinesq [34] who

introduced an eddy viscosity,  $\nu_T$ , in complete analogy with the molecular viscosity for a Newtonian fluid. The Reynolds stress tensor is related to the mean flow as following

$$\overline{u_i u_j} = -2\nu_T S_{ij} + \frac{2}{3} k \cdot \delta_{ij}, \tag{25}$$

where k is the turbulent kinetic energy and is equal to  $\overline{u_i u_i}/2$ . The last term is often included in the pressure term. Then, introducing the dissipation per unit mass,  $\epsilon = \nu \frac{\partial u_i}{\partial x_j} \frac{\partial u_i}{\partial x_j}$ , the eddy viscosity can be estimated as proportional to  $k^2/\epsilon$ . This relation is developed only on the basis of dimensional arguments, and provided that k and  $\epsilon$  are strictly functions of the turbulence independent of natural fluid properties such as molecular viscosity [35].

In analogy with the eddy-viscosity concept the Reynolds-mass-flux may be obtained by a simple gradient diffusion model

$$\overline{u_i c} = -\frac{\nu_T}{S c_T} \frac{\partial C}{\partial x_i}.$$
 (26)

In a zero equation model an assumption of a constant turbulent Schmidt number,  $Sc_T$ , is made, but for many engineering applications this is not enough accurate. The turbulent Schmidt number is then modelled as a function of the ratio, r, between the mass,  $k_c/\epsilon_c$ , and dynamic,  $k/\epsilon$ , time-scales, where  $k_c$  denotes the mass variance and is equal to  $\overline{c^2}/2$ .  $\epsilon_c$  is the mass dissipation rate and is equal to  $D\frac{\partial c}{\partial x_j}\frac{\partial c}{\partial x_j}$ . Information about the time-scale ratio may be particularly important in situations when it differs significantly from one. As Kawamura  $et\ al.$  showed it [36], r tends to Sc when the electrode is approached. This result was also found in the numerical study made in paper 6.

As Wikström *et al.* note it in [2], it is quite well known today that the Boussinesq assumption is unable to always predict realistic values of Reynolds flux, since it assumes that the mass flux is aligned with the mean concentration gradient. In particular, in a fully developed channel flow, the streamwise gradient of the mean concentration is zero, but not  $\overline{uc}$ .

#### 4.3. The wall-function problem

Understanding and prediction of mass transfer between a solid boundary and a turbulent fluid flow is of great interest in many engineering problems. Many studies have been devoted to numerical and experimental investigations of this problem at various Reynolds and Schmidt numbers. The major issue of most of these studies is the prediction of average mass transfer coefficients and of mass profiles in the buffer region.

In this context, mass transfer at high Schmidt number is of particular importance for industrial concerns in the field of electrochemistry. Compared to the case of mass transfer at low or moderate Schmidt number, its study appears to be much more difficult: the diffusive layer lies entirely into the viscous sublayer, meaning that mass transfer efficiency is controlled by turbulent motions present

very close to the wall. Many previous scientific and industrial investigations have been carried out on that region close to the wall, as Kader [37] and Calmet [38] did. But by now, none of them considered non linear boundary conditions as Butler-Volmer laws.

In the case of natural convection, another crucial issue is to determine the importance and the nature of the buoyancy influence on the buffer region and possibly even in the viscous sublayer. However, recent calculations [16] showed that the wall functions proposed by Launder et al. [39] for the computation of uncoupled and fully turbulent flows, gave a good estimation of the viscous boundary layer even in the near-wall region. As a first step of comprehension, it is consequently reasonable to produce a series of results concerning the diffusive boundary layer in the near-wall region for a situation of forced convection.

Wall-functions are used to fill the gap between the wall and the region far enough from the wall, where the turbulence model is valid. In other words, wall-functions have the function of boundary conditions situated at a certain distance from the wall. The most used model among the turbulence models is the  $k-\epsilon$  model, which belongs to the class of the two-equation-models. These models provide not only for computation of k, but also for a turbulence length scale or equivalent. In the case of the  $k-\epsilon$  model, two transport equations are considered; one for the computation of the turbulent kinetic energy and one for the dissipation rate,  $\epsilon$ 

$$\rho \frac{\partial k}{\partial t} + \rho \nabla \cdot (k\mathbf{U}) - \nabla \cdot \left( \left( \mu + \frac{\mu_T}{\sigma_k} \right) \nabla k \right) = P + G - \rho \epsilon, \tag{27}$$

$$\rho \frac{\partial \epsilon}{\partial t} + \rho \nabla \cdot (\epsilon \mathbf{U}) - \nabla \cdot \left( \left( \mu + \frac{\mu_{\epsilon}}{\sigma_{\epsilon}} \right) \nabla \epsilon \right) = C_1 \frac{\epsilon}{k} P - C_2 \rho \frac{\epsilon^2}{k}, \tag{28}$$

where,

$$\mu_{T} = C_{\mu} \rho \frac{k^{2}}{\epsilon},$$

$$\mu_{eff} = \mu + \mu_{T},$$

$$P = \mu_{eff} \nabla \mathbf{U} \cdot \left( \mathbf{U} + (\mathbf{U})^{T} \right),$$

$$G = \frac{-\mu_{eff}}{\rho \cdot \sigma_{T}} \mathbf{g} \cdot \nabla \rho.$$

The model is closed by using the Boussinesq approximation for both the velocity and the concentration field.

A series of numerical simulations, carried out for the turbulent case of Ziegler et al. [11], proved that G does not influence the prediction of the mean velocity, and can be neglected in the transport equation for k. The constants are chosen as  $C_1 = 1.44$ ,  $C_2 = 1.92$ ,  $C_{\mu} = 0.09$ ,  $\sigma_T = 0.9$ ,  $\sigma_k = 1$  and  $\sigma_{\epsilon} = 1.2174$ .

The following two chapters expose the concept of wall-functions in details and explain the shortcomings of its standard form for mass transfer at very high

 $<sup>^1\</sup>mathrm{See}$  [40] for more details about the  $k-\epsilon$  model

Schmidt number. The third chapter gives an alternative wall-function for mass in electrochemical applications.

4.3.1. Limitation of the standard assumption. In this chapter and in the next two others, all variables are dimensionalized in viscous units. This choice has been made in order to determine more easily the positions of the different regions in the boundary layers. For any scalar  $\tilde{\phi}$  with a diffusivity  $D_{\phi}$ , the standard assumption for the non-dimensional profile of the mean value in the inner region, is formulated in [40] as following

$$\Phi^{+} = \begin{cases} Sc \ y^{+} & y^{+} \leq y_{o}^{+} \\ \frac{\sigma_{\phi}}{\kappa} \ ln(E_{\phi}y^{+}) & y^{+} \geq y_{o}^{+} \end{cases}$$
 (29)

where  $y_o^+=a_M\cdot Sc^{-1/3}$ ,  $\kappa$  is Kárman constant, Sc is Schmidt number  $\frac{\nu}{D_\phi}$ , and  $\sigma_\phi$  the turbulent Schmidt number for scalar  $\tilde{\phi}$ ,  $\frac{\nu_T}{D_{\phi,T}}=0.9$ . This last value is assumed constant in equation (29). It is worth noting that the actual turbulent Schmidt number varies in the fluid and is equal to  $\frac{\overline{uv}(\partial\Phi/\partial y)}{\overline{v}\phi(\partial U/\partial y)}$ . At Schmidt number equal to one,  $a_M$  is taken in previous studies [19, 37] equal to 11.25. The constant  $E_\phi$  is defined as

$$E_{\phi} = E \cdot exp \left[ 9\kappa \left( \left( \frac{Sc}{\sigma_{\phi}} \right)^{0.75} - 1 \right) \left( 1 + 0.28e^{-0.007 \frac{Sc}{\sigma_{\phi}}} \right) \right], \tag{30}$$

where E is the "loglayer" constant and is equal to 9.793 [40].

When Schmidt number is very large,  $E_{\phi}$  is approximately equal to  $\left(E \cdot exp\left[\frac{9\kappa}{\sigma_{\phi}^{3/4}}Sc^{3/4}\right]\right)$ . As a result,  $\Phi^+$  becomes extremely large in the log-layer. For instance, at Sc=900,  $E_{\phi}=9.3\cdot 10^{285}$ . The standard log-law as shown in equation (29) is thus not usable already at Schmidt number higher than a few hundreds.

In theory, the computational domain could be chosen refined enough near the wall in order to use the linear region of the wall-function (29) at the nearest node P of the grid from the wall. But in practice, for mass transfer in an electrochemical cell, this situation will require a huge computational domain, as it is demonstrated below, and the nowadays computational capacities impede the choice of a linear wall-function for mass transfer.

In a running cell with only one chemical reaction at the electrodes and a binary electrolyte, the maximum local excess of concentration is limited by the uniform concentration in the cell  $\Phi_o$  when there is no current set at the electrodes. This is verified because the present study considers cells at the equilibrium state only, and there is no variation of the total amount of mass in the cell. This inequality in viscous wall-units can be written  $\Phi_P^+ \leq \Phi_o^+$ , where  $\Phi_o^+$  is of the order of unity. Using the linear-law of equation (29), one obtains the condition

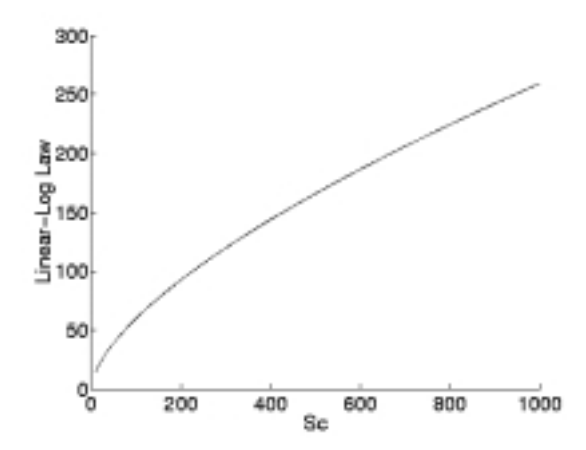


FIGURE 4.1 The difference (32) of the linear and the logarithmic law for the mean concentration in the inner region at  $y_1^+$ , as a function of Schmidt number. m=3.

 $y_P^+ \leq \frac{\Phi_o^+}{Sc}$ . This last condition requires an extremely refined grid, when Schmidt number is of the order of several thousands.

Hence, it seems necessary to formulate a new wall-function in the diffusive log-layer at high Schmidt numbers.

**4.3.2.** Limitation of the Kader assumption. Kader *et al.* [41] proposed a modified logarithmic law for mass transfer when  $Sc \geq 0.5$ 

$$\Phi^{+} = \begin{cases} Sc \ y^{+} & y^{+} \leq y_{1}^{+} \\ \alpha \ ln(y^{+}) + \frac{m^{2} + 1}{m^{2} - 1} a_{H}^{-1/m} Sc^{(m-1)/m} + \alpha \ ln(Sc) - 5.3 \ y^{+} \geq y_{1}^{+}, \end{cases}$$
(31)

where  $y_1^+ = (a_H S c)^{-1/m}$ .  $a_H$ , m, and  $\alpha$  are supposed constant, and are equal to 0.001, 3, and 2.12, respectively. There is no complete agreement about the value of m in previous studies; as an example Calmet  $et\ al.$  [38] found m=3.38. The log-layer of equation (31) was developed considering the eddy viscosity and diffusivity different from zero, even in the viscous sublayer. It was also assumed a three-layer model for the diffusive boundary layer, proposed by Levich [5], similar to the one found for the inner region of the viscous layer.

Figure 4.1 shows the difference (32) of the linear and the logarithmic law for the mean concentration in the inner region at  $y_1^+(Sc)$  when Schmidt number varies

$$\left(a_H^{-1/m} - \frac{m^2 + 1}{m^2 - 1}\right) Sc^{(m-1)/m} - \alpha \ln \left[a_H^{-1/m} Sc^{(m-1)/m}\right] + 5.3. \tag{32}$$

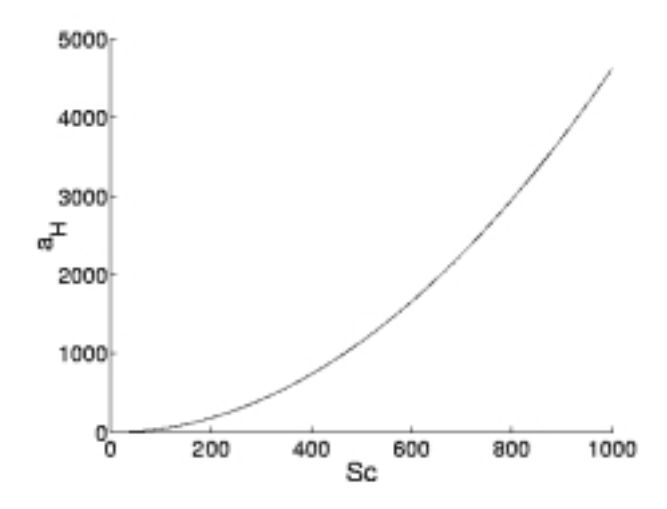


Figure 4.2  $a_H$  as a function of Schmidt number.  $a_H$  is computed in order to get the difference (32) equal to zero.

The difference is already greater than one when Schmidt number is equal to 10. If one wants to obtain a small value for the difference (32), it is then necessary to consider  $a_H$  as a function of Schmidt number. For simplicity, m is supposed here independent of Schmidt number. The order of variation of  $a_H$  with Schmidt number is evaluated below.

 $a_H$  and m are defined by the first term of a Taylor expansion of the eddy diffusivity  $D_{\phi,T}$  [41]. In the diffusive sublayer  $D_{\phi,T}$  can be approximated by

$$\nu a_H(y^+)^m. \tag{33}$$

 $a_H$ , shown in figure 4.2, varies over six orders of magnitude when Schmidt number varies between 1 and 1000. As a result, the eddy diffusivity  $D_{\phi,T}$  varies in magnitude of several orders in the near-wall region, when Schmidt number varies. For instance, at Schmidt number equal to 1000 and at  $y^+ = 1$ ,  $D_{\phi,T} = 4.624 \cdot 10^3$ .

In forced convection, the hydrodynamical boundary layer is decoupled from mass transport, and the eddy viscosity is consequently not a function of Schmidt number. The turbulent Schmidt number  $\frac{\nu_T}{D_{\phi,T}}$  predicted with the previous assumptions is then highly dependent of Schmidt number and tends to zero in the near-wall region when Schmidt number increases. This result is not in agreement with previous studies. Abe et al. [42] and Kawamura et al. [36] found that the turbulent Schmidt number tends to be independent of Schmidt number in the near-wall region when Schmidt number increases. The two last mentioned studies considered Schmidt number only between 0.025 and 5.0. They found almost the same turbulent Schmidt number of 1.1, in the near-wall region and at Schmidt number equal to 0.71 and 5.0. If one accepts their result at larger

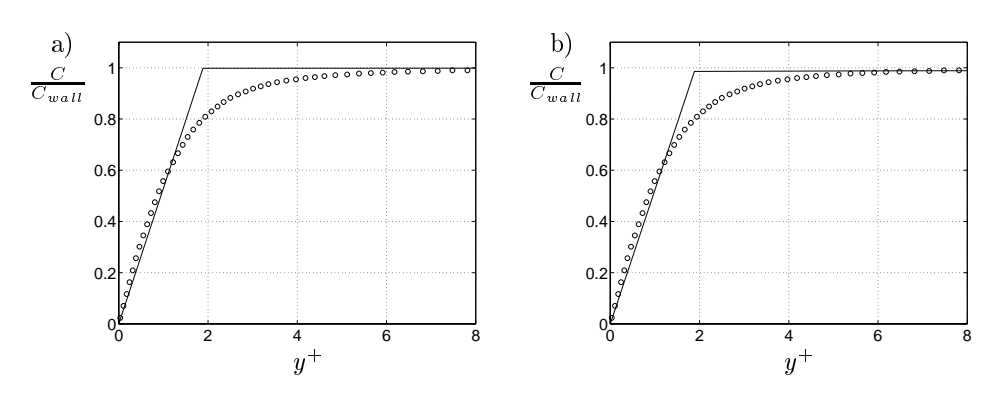


Figure 4.3 At Sc=3000, the mean concentration profile along the electrode-normal direction. Solid line:  $k-\epsilon$  model. Circles: large-eddy simulation (LES). a) Predicted with a linear wall-function. b) Predicted with a logarithmic wall-function.

Schmidt numbers, and since the eddy viscosity is not dependent of Schmidt number, the eddy diffusivity should not vary appreciably with Schmidt number in the near-wall region.

In Brief, supplementary information about the scaling of the diffusive boundary layer are required in order to validate the wall-function proposed by Kader *et al.* [41].

4.3.3. An alternative wall-function for mass. In this chapter, the wall-function proposed in paper 6 is tested with success with the  $k-\epsilon$  model. The concentration corresponds to an ionic species of a binary electrolyte, and convection is forced in an channel flow working as an electrochemical cell. The platform for the  $k-\epsilon$  is the commercial CFD code CFX developed by AEA Technology. The considered geometry is a 3D-channel flow made of two infinite plates in the streamwise, x, and the spanwise, z, direction. The computational domain is periodic in these two directions with periodicity lengths chosen long enough to respect the largest turbulent length-scales, see paper 2 for the dimensions and the geometry. Sc=3000 and the turbulent Reynolds number, based on the channel half-width, is equal to 180. The boundary condition for the concentration at the electrodes is a constant value, corresponding to the idealized electrochemical situation of a cell working at the limiting current.

Figures 4.3a and 4.3b show the concentration profile  $C(y^+)/C_{wall}$  predicted with the  $k-\epsilon$  model when using a linear and a log-law, according to equation (29). The predictions are compared with large-eddy simulations made in paper 4, 5 and 6, at the same Schmidt number. Figure 4.3b shows that the logarithmic profile does not improve the crude model of a pure diffusive profile shown in 4.3a.

If one considers the mass-conservation equation (3) for a fully developed flow, one obtains for a channel flow

$$\frac{1}{Sc}\frac{\partial C^{+}}{\partial y^{+}} - \overline{v^{+}c^{+}} = \tau_{o},\tag{34}$$

where  $\tau_o = -1$ . A simple model for the wall-normal component of the Reynolds-flux vector is considered in Paper 6, where  $\overline{v^+c^+} = a_v \cdot k^+ \cdot \tau^+ \cdot \frac{\partial C^+}{\partial y^+}$ , where  $\tau^+$  is a mixed time-scale between the two time-scales of chapter 4.2,  $\tau^+ = \sqrt{\frac{kk_c}{\epsilon\epsilon_c}}$ . Using this model, equation (34) becomes

$$\frac{\partial C^{+}}{\partial y^{+}} = -Sc - a_{c} \cdot k^{+} \cdot \tau^{+} \frac{\partial C^{+}}{\partial y^{+}} \quad , \tag{35}$$

where  $a_c$  is a positive constant, possibly dependent on Schmidt number. One can then derive an integral function for the mean passive scalar as a function of the wall-normal distance

$$C^{+}(y_{o}) = C_{wall}^{+} - Sc \cdot \int_{0}^{y_{o}} \frac{dy^{+}}{1 + a_{c}k^{+}\tau^{+}} .$$
(36)

This equation can be integrated in the near-wall region if one considers the Taylor series of the turbulent kinetic energy and the time-scale  $\tau^+$ . It can easily be shown that  $a_c \cdot k^+ \cdot \tau^+ = A_c(Sc) \cdot y^{+4} + \mathcal{O}(y^{+5})$  when the wall is approached. This result is obtained when one considers the limiting behaviour near the wall, of the velocity components and the concentration fluctuations [36]. Equation (36) can then be integrated with the help of this approximation, and  $C^+$  is found as a function of  $y^+$  as follows

$$C^{+}(y) = C_{wall}^{+} - \frac{Sc}{A_{c}^{1/4} 2\sqrt{2}} \left[ \frac{1}{2} ln \left( \frac{z^{2} + z\sqrt{2} + 1}{z^{2} - z\sqrt{2} + 1} \right) + arctan \left( \frac{z\sqrt{2}}{1 - z^{2}} \right) \right], \quad (37)$$

where  $z=y^+A_c^{1/4}$ . This equation was shown to give good results in the near-wall region, and surprisingly, even in the logarithmic region of the diffusive boundary layer, provided that another value for  $A_c$  is chosen, see figure 4.4. This result tends to prove that the asymptotic behaviour of  $k^+ \cdot \tau^+$  as  $y^{+4}$  is valid even outside the diffusive sublayer. This wall-function was then implemented in CFX and tested with the same geometry, and the same parameters. Figure 4.5 shows good agreement between the predictions of the present study with a large-eddy simulation (LES) and the  $k-\epsilon$  model. With  $y^+$  between 0 and  $5/Sc^{1/3}$ , the profile is linear. The nearest node from the electrode in the numerical domain for the  $k-\epsilon$  computation lies in the log-region of the diffusive layer  $(y^+ \approx 45/Sc^{1/3})$ .

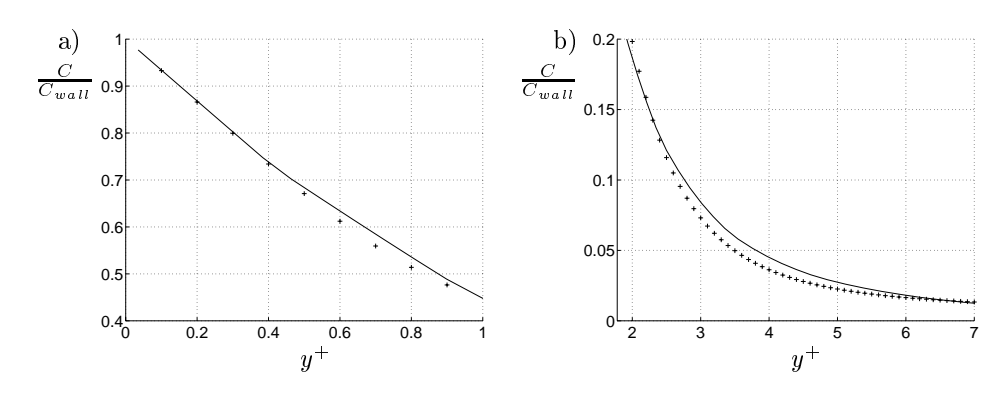


FIGURE 4.4 At Sc=3000, the mean profile of the passive scalar along the wall-normal distance. Solid line:  $C^{\rm LES}$ . ++++:  $C^{\rm model}$ . a) In the near-wall region.  $A_C=3/2$ . b) Outside In the 'logarithmic' region of the diffusive boundary layer.  $A_C=0.12$ .

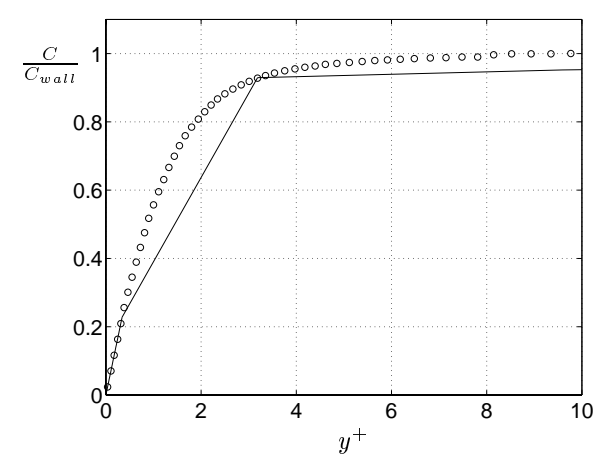


Figure 4.5 At Sc=3000, the mean concentration profile along the electrode-normal direction. Solid line: predicted with CFX and the new wall-function. Circles: predicted with LES.

#### 4.4. Algebraic Reynolds stress models

Nowadays, there is a renewed interest in algebraic models which are obtained from the transport equations using some equilibrium assumption. This interest can in a large extent be explained by the simplicity of the produced models. As Wallin  $et\ al.\ [43]$  notice it, they require a computational effort comparable to the one required for the  $k-\epsilon$  model, but are more reliable for flows in near-wall regions.

The classical algebraic Reynolds stress model was developed from the modelled Reynolds stress transport equation by assuming that advection minus the

diffusion of the individual Reynolds stresses can be expressed as the product of the corresponding quantity for the kinetic energy, k, and the individual Reynolds stresses normalized by k [43]. This results in an implicit relation between the stress components and the mean velocity gradient that replaces the Boussinesq hypothesis. The general form looks like as following

$$\overline{u_i u_j} = F_{ij} \left( \overline{u_k u_l}, S_{kl}, \Omega_{kl}, k, \epsilon, \overline{u_k c}, \overline{c^2} \right), \tag{38}$$

where  $\Omega_{ij} = (U_{i,j} - U_{j,i})/2$ . In the case of forced convection, Wallin *et al.* [43] developed an explicit version of an algebraic Reynolds stress model where the Reynolds stresses were explicitly related to the mean flow field.

The most common approach for the mass flux is the so called weak equilibrium assumption, where the advection and diffusion terms of the transport equation for the normalized mass flux is neglected [44]. A similar equation to (38) can then be produced for the Reynold-flux vector

$$\overline{u_i c} = G_i \left( \overline{u_k c}, \overline{u_k u_l}, \frac{\partial U_k}{\partial x_l}, \frac{\partial C}{\partial x_l}, k, k_c, \epsilon, \epsilon_c \right)$$
(39)

Provided some extra assumption, this relation can also become explicit, see [44]. In a case of forced convection,  $F_{ij}$  does not depend on the last two terms in equation (38), see [2, 44].

In paper 6 of this work, a new explicit algebraic model has been developed for the Reynolds-flux in a case of forced convection in a channel flow working as an electrochemical cell. This model was validated for a very high Schmidt number only, and was developed on the basis of an assumption found in paper 5 for the transport equation of the Reynolds flux at equilibrium. Equilibrium refers here to the state of the flow when all the statistics do not depend on time.

#### CHAPTER 5

# Large-eddy simulation

As widely known, the computation of turbulence in averaged sense involves resolution of extra terms of correlations between the fluctuating parts of the variables. The most popular method to model those unknown quantities is the  $k-\epsilon$  model, which is based on the mixing-length theory. In  $k-\epsilon$  model, the extra terms, called Reynolds stresses, are assumed to be proportional to the local gradient of the average velocity and to the turbulent viscosity. This viscosity has a local quantity, proportional to  $k^2/\epsilon$ , where k is the turbulent kinetic energy and  $\epsilon$  the dissipation rate. These two new unknowns are computed by introducing a transport equation for each, where the time-derivative and the convective terms balance at any time production and dissipation terms. Although the  $k-\epsilon$  model has the advantage to be numerically robust, it has the big inconvenience of not accounting for anisotropic effects, as the presence of a wall for instance. This neglect is of importance especially in the near-wall region.

An alternative strategy is the direct numerical solution (DNS), and consists in computing the turbulent flow by solving the discretized equations with a mesh fine enough to resolve even the smallest scales of motion expressed by the terms of fluctuations introduced above. This method does not rely on any model to compute turbulence, but the size of cells appears to be imposed by the smallest turbulence scales, the Kolmogorov scales, and consequently proportional to  $L/Re^{3/4}$ , where L is the size of the computational domain. In a three-dimensional computation, the number of nodes of the mesh will be proportional to  $Re^{9/4}$ . Thus, this approach is restricted to low Reynolds numbers due to memory limitations imposed by todays computers. An important issue with respect to the computational needs of a time accurate numerical simulation is that a high spatial resolution necessitates a high temporal resolution. Consequently, a larger number of time steps has to be computed for a given physical span of time when the discretization is very fine.

Large-eddy simulation (LES) is an intermediate technique between the direct simulation and modelling the Reynolds stresses. In LES the contribution of the large energy-carrying structures is computed exactly, and only the effect of the smallest scales of turbulence is modelled using subgrid scale models. Since the small scales turbulence tends to be more isotropic than the large, the use of isotropic models seems reasonable, and allow to solve the average Navier-Stokes equation on coarser meshes than those used in DNS.

The concept of LES mainly rests on two presumptions which appear plausible in view of both practical experience and theoretical considerations. The first of these is that small scales tend to depend only on viscosity, and may be somewhat universal. The large ones are affected very strongly by the boundary conditions, and in return, most global features of turbulent flows, like average mixing rates or averaged losses, are governed by the dynamics of the large scales and depend only little on the small-scale turbulence. Thus, in LES the contribution of large energy-carrying structures to momentum and energy transfer is computed exactly, and only the effect of the smallest scales of turbulence is modeled, by so-called subgrid-scale models.

Turbulence generation occurs mainly at the large scales of a flow and viscous dissipation occurs mainly at the small scales. The most important feature of a subgrid-scale model is then to provide adequate dissipation. Here, dissipation means transport of energy from the resolved grid scales to the unresolved subgrid scales, and the rate of dissipation  $\epsilon$  in this context represents the flux of energy from the large to the small scales. To illustrate the role of the subgrid-scale models it is useful to consider possible consequences if turbulence simulations are performed with insufficient resolution. An obvious implication of a too coarse resolution is that the viscous dissipation in the flow cannot properly be accounted for. This deficiency will typically result in an accumulation of energy at the highwavenumber end of the resolved spectrum, which reflects a distorted equilibrium state between the production and dissipation of turbulent kinetic energy. For sufficiently high Reynolds numbers (or conversely sufficiently coarse grids) the discrete representation of the flow even becomes essentially inviscid and the nonlinear transfer of energy can lead to an abnormal growth of turbulence intensities and eventually to numerical instability of the computation.

#### 5.1. Subgrid-scale model

In this work, except in paper 1, a large-eddy simulation approach is used to study the diffusive boundary layer in a turbulent channel flow. The numerical code is the continuation of the code used to produce the results reported in [45]. Model equations are formulated for the filtered velocity, mass and pressure fields. The filter function determines the size and structure of the smallest scales resolved without modelling. The most commonly-used filter functions are the sharp Fourier cutoff filter, the Gaussian filter and the tophat filter [46]. In the present work, the filter consists in averaging  $\tilde{f}$  in a cubic volume whose center is  $\mathbf{x}^M$ . M stands for the center of a given cell in a three-dimensional grid system,  $\mathbf{x}^M$  denotes the coordinates of M, and  $\Delta x_1^M$ ,  $\Delta x_2^M$  and  $\Delta x_3^M$  the side lengths of the cell, where 1, 2 and 3 stand for the indices of the three spatial directions. If a continuous function  $\tilde{f}(\mathbf{x})$  is considered,  $\overline{f}^M$  stands for the filtered version of  $\tilde{f}$  on space, at the center of cell M, whose volume is  $\Delta x_1^M \Delta x_2^M \Delta x_3^M$ . Note that

 $\overline{f}^M$  is an instantaneous variable. If  $\mathcal{T}^M$  stands for the filtering operator,  $\overline{f}^M = \mathcal{T}^M \left( \tilde{f}; \mathbf{x}^M \right)$ .

Similarly,  $S_i^M$  ( $\tilde{f}$ ;  $\mathbf{x}$ ) stands for the average of  $\tilde{f}$  over a plane surface element  $\Delta s_i^M$ , which is centered at  $\mathbf{x}$ , normal to  $\mathbf{e}_i$ , and whose size is  $\Delta x_j^M \Delta x_k^M$ , where j and k are different from i.

Finally, the volume average of the Navier-Stokes equation in cell M, assuming the fluid density  $\rho=1$ , is

$$\Delta v^{M} \frac{\partial \overline{u}_{i}^{M}}{\partial t} = \sum_{j=1}^{3} \Delta s_{j}^{M} \mathcal{S}_{j}^{M} \left( \left\{ -\tilde{u}_{i}\tilde{u}_{j} - \tilde{p}\delta_{ij} + \tilde{\tau}_{ij} \right\}, \mathbf{x}^{M} + \frac{1}{2} \Delta x_{j} \mathbf{e}_{j} \right)$$
$$- \sum_{j=1}^{3} \Delta s_{j}^{M} \mathcal{S}_{j}^{M} \left( \left\{ -\tilde{u}_{i}\tilde{u}_{j} - \tilde{p}\delta_{ij} + \tilde{\tau}_{ij} \right\}, \mathbf{x}^{M} - \frac{1}{2} \Delta x_{j} \mathbf{e}_{j} \right)$$
(40)

where  $\tau_{ij}$  is the viscous stress tensor, and  $\delta_{ij}$  the Kronecker delta.

As far as the linear terms are concerned (namely  $-\tilde{p}\delta_{ij}$  and  $\tilde{\tau_{ij}}$ ), the filtering of the momentum equation poses, in principle, no difficulties. On the contrary, the advective term of the last equation, i.e.  $\pm \sum_{j=1}^{3} \Delta s_{j}^{M} \mathcal{S}_{j}^{M} \left( \tilde{u}_{i}\tilde{u}_{j}; \mathbf{x}^{M} \pm \frac{1}{2}\Delta x_{j}\mathbf{e}_{j} \right)$ , needs to be modelled in terms of the resolved velocity field  $\overline{u}_{i}^{M}$ .

For that purpose,  $u_i^{(\pm j)M}$  is introduced as the unresolved part of the velocity field, evaluated on the cell surface whose centre is the vector  $\mathbf{x}^M \pm \frac{1}{2} \Delta x_j \mathbf{e}_j$ , and whose normal direction is  $\mathbf{e}_j$ , i.e.

$$u_i^{(\pm j)M} = \tilde{u}_i - \mathcal{S}_j^M \left( \tilde{u}_i; \mathbf{x}^M \pm \frac{1}{2} \Delta x_j \mathbf{e}_j \right). \tag{41}$$

Then, according to the definition of  $S_j$ , the total convective transport of momentum  $\tilde{u}_i \tilde{u}_j$  across the cell surface centered in  $\mathbf{x}^M \pm \frac{1}{2} \Delta x_j \mathbf{e}_j$  and parallel to  $\mathbf{e}_j$ , can be written

$$S_{j}^{M}\left(\tilde{u}_{i}\tilde{u}_{j};\mathbf{x}^{M}\pm\frac{1}{2}\Delta x_{j}\mathbf{e}_{j}\right) = S_{j}^{M}\left(\tilde{u}_{i};\mathbf{x}^{M}\pm\frac{1}{2}\Delta x_{j}\mathbf{e}_{j}\right)S_{j}^{M}\left(\tilde{u}_{j};\mathbf{x}^{M}\pm\frac{1}{2}\Delta x_{j}\mathbf{e}_{j}\right) + S_{j}^{M}\left(u_{i}^{(\pm j)M}u_{j}^{(\pm j)M};\mathbf{x}^{M}\pm\frac{1}{2}\Delta x_{j}\mathbf{e}_{j}\right)$$
(42)

The first term, the product of the surface averages of the total non-dimensional momentum  $\tilde{u}_i \tilde{u}_j$  is approximated by the mean of the volume averages in the cells on both sides of the surface. For the second term, on the other hand, which can be thought of as a Reynolds stress associated with the unresolved motion, a model has to be formulated. For notation convenience, this term is noted  $F_j(\tilde{u}_i)^{(\pm j)M}$ , and denotes the subgrid flux of momentum in the  $\mathbf{e}_i$ -direction through the surface centered at  $\mathbf{x}^M \pm \frac{1}{2} \Delta x_j \mathbf{e}_j$  and whose normal direction is  $\mathbf{e}_j$ . Following the classical Boussinesq eddy viscosity model, one may assume that the subgrid momentum flux through surfaces of computational cells is proportional to the eddy diffusion of momentum. However, as Zahrai [45] suggested, the eddy diffusivity

is assumed to depend on mesh sizes in different, through which the subgrid flux of momentum is to be estimated. For a computational mesh with significantly different spatial step sizes, the present subgrid model prescribes different magnitudes of subgrid transport in different directions. In order to account for this grid anisotropy, one may assume an expression of the following form

$$F_j(\tilde{u}_i)^{(\pm j)M} = -\nu_t^{(\pm j)M} S_{ij}^{(\pm j)M}, \tag{43}$$

where  $S_{ij}^{(\pm j)M}$  is the filtered quantity  $\overline{s}_{ij}^M$  evaluated on the cell surface under consideration, and  $\tilde{s}_{ij}$  is twice the instantaneous strain rate tensor. Its numerical computation involves the average of  $\overline{s}_{ij}^M$  between the two cells containing the surface.  $\nu_t^{(\pm j)M}$  is interpreted as a grid-dependent anisotropic eddy viscosity. Following Deardoff [47], Zahrai et al. assumed that the local eddy viscosity depends on the filtered dissipation  $\overline{\epsilon}^M$  and a cut-off length scale  $l_*^{(\pm j)M}$ . For dimensional reasons, one may then write  $\nu_t^{(\pm j)M} = (\overline{\epsilon}^M)^{1/3} (l_*^{(\pm j)M})^{4/3}$ . Again, following Deardorff for the estimation of  $\overline{\epsilon}^M$  and  $l_*^{(\pm j)M}$ , Zahrai showed that the original formulation of the Smagorinsky model for  $\overline{\epsilon}^M$  could be easily adapted to the present situation of a highly anisotropic grid. The cut-off length scale for subgrid eddy diffusion,  $l_*^{(\pm j)M}$ , is approximately  $\Delta x_j^M$ , since the smallest resolved length scale in the j-direction is  $\Delta x_j^M$ . Finally, collecting the assumptions done above, one arrives to the following expression

$$F_{j}(\tilde{u_{i}})^{(\pm j)M} = -\frac{1}{\sqrt{2}} \mathcal{C}^{2} \mathcal{L}_{j}^{2} \left| \overline{s}_{ij}^{M} \right|^{(\pm j)M} S_{ij}^{(\pm j)M}, \tag{44}$$

where  $\left|\overline{s}_{ij}^{M}\right| = \left(\sqrt{\sum_{i=1}^{3} \sum_{j=1}^{3} \overline{s}_{ij}^{M^{2}}}\right)$  and  $\mathcal{L}_{j}^{2} = (\Delta x_{1}^{M} \Delta x_{2}^{M} \Delta x_{3}^{M})^{2/9} (\Delta x_{j}^{M})^{4/3}$ .  $\mathcal{C}$  is taken equal to the Smagorinsky constant, 0.08, as suggested in [45].

Equation (40) becomes  $\Delta v^M \frac{\partial \overline{u}_i^M}{\partial t} = \sum_{j=1}^3 \Delta s_j^M \left[ -\left( \overline{u_i}^{(+j)M} \overline{u}_j^{(+j)M} - \overline{u}_i^{(-j)M} \overline{u}_j^{(-j)M} \right) \right] \\ - \sum_{j=1}^3 \Delta s_j^M \left[ \left( \overline{p}^{(+j)M} - \overline{p}^{(-j)M} \right) \delta_{ij} \right] \\ + \sum_{j=1}^3 \Delta s_j^M \left[ +\left( \overline{\tau}_{ij}^{(+j)M} - \overline{\tau}_{ij}^{(-j)M} \right) \right] \\ + \sum_{j=1}^3 \Delta s_j^M \left[ +\frac{1}{\sqrt{2}} \mathcal{C}^2 \mathcal{L}_j^2 \left( \left| \overline{s}_{ij}^M \right|^{(+j)M} \cdot \overline{s}_{ij}^{(+j)M} - \left| \overline{s}_{ij}^M \right|^{(-j)M} \cdot \overline{s}_{ij}^{(-j)M} \right) \right],$  and similarly, the filtered continuity equation gives

$$\sum_{i=1}^{3} \sum_{j=1}^{3} \Delta s_{j}^{M} \left[ \overline{u}_{i}^{(+j)M} - \overline{u}_{i}^{(-j)M} \right] = 0.$$
 (45)

Note that the superscript  $\overline{(\cdot\cdot\cdot)}^{(\pm j)M}$  denotes the filtered quantity evaluated on the cell surface whose center is the vector  $\mathbf{x}^M \pm \frac{1}{2} \Delta x_j^M \mathbf{e}_j$  and whose normal

direction is  $e_i$ . The Navier-Stokes equations can be manipulated to get a Poisson equation for the pressure correction. The SIMPLE algorithm is used here. The pressure correction technique is basically an iterative approach and the process is as follows. The iterative process is started by guessing the pressure field  $p^*$ . The Navier-Stokes equations are then solved with  $p^*$ . It results of a velocity field  $(u^*, v^*, w^*)$ . Since the velocity field is obtained with the guessed pressure, it does not satisfy the continuity equation. From the continuity equation an elliptic equation for the pressure correction p' is derived. The physical interpretation of the elliptic pressure equation is that a disturbance in the pressure at some point is instantaneously experienced everywhere. The corrected pressure,  $p = p^* + p$ , is then used to calculate the corresponding corrected velocity (u', v', w'). The velocity field is then updated. Note that the flow is driven by a body force, or by a pressure gradient constant in space and time. In other words, the pressure term is decomposed into a mean pressure gradient in the streamwise direction and equal to 1 in viscous units, and a fluctuating part which is to be solved together with the velocity field.

The governing equation for the concentration transport can also be filtered at each cell M, which can differ from those used for the velocity field

$$\Delta v^{M} \frac{\partial \overline{c}^{M}}{\partial t} = \sum_{k=1}^{3} \Delta s_{k}^{M} \left[ -\left(\overline{c}^{(+k)M} \overline{u}_{k}^{(+k)M} - \overline{c}^{(-k)M} \overline{u}_{k}^{(-k)M}\right) \right]$$

$$+ \sum_{k=1}^{3} \Delta s_{k}^{M} \left[ \left( \frac{1}{Sc} + \frac{\frac{1}{\sqrt{2}} \mathcal{C}^{2} \mathcal{L}_{k}^{2}}{Sc_{t}} \right) \left( \left| s_{ij}^{M} \right|^{(+k)M} \cdot \overline{j}_{k}^{(+k)M} - \left| s_{ij}^{M} \right|^{(-k)M} \cdot \overline{j}_{k}^{(-k)M} \right) \right], (46)$$

where  $j_k$  is the concentration gradient in the k-direction. The turbulent Schmidt number,  $Sc_t$ , was set to 0.25, which may be a reasonable value, since the turbulent Prandtl number,  $Pr_t$  in the cases of large eddy simulation with heat transfer is usually proposed to be between 1/2 and 1/3, see e.g. [48].

### 5.2. Discretization and mesh systems

Throughout the remainder of this section, all the variables are considered filtered. The discretization of the momentum equations are not described, since the present work has contributed to the numerical development of the mass transport equation only. A detailed description of the discretization of the conservation equation for mass is presented.

The Navier-Stokes equations can be written the following form

$$\tilde{u}_t + C\tilde{u} = \frac{1}{Re}V\tilde{u},$$

where  $C\tilde{u}$  contains the convection part and  $V\tilde{u}$  the pressure and viscous parts of the NS equations. An explicit time discretization is then introduced

$$\frac{u^{n+1} - u^n}{\Delta t} = Iu^n, (47)$$

where  $I\tilde{u} = -C\tilde{u} + V\tilde{u}$ .

The velocity field is then interpolated with a fourth order scheme, from the grid where it has been calculated, to a finer grid, notated  $(\cdots)^c$  in the rest of this chapter, where the concentration field is calculated. In each direction, the integer  $IPC_i$  represents the ratio between the number of nodes of the fine and the coarse mesh. In the present study, the grid associated to the concentration field is finer only in the normal direction of the walls.  $IPC_2$  and  $IPC_3$  are then equal to one, and the interpolation is only required in the normal direction of the walls.

Since the velocity is staggered in the three directions, the interpolation is performed with the vortices coordinates  $x_1$  for  $\tilde{u}_1$ , and with the coordinates of the cell-centers  $x_1^f$  for  $\tilde{u}_2$  and  $\tilde{u}_3$ . Here, the interpolation formula is defined indifferently for the three components, provided that the coordinates  $x_1$  and  $x_1^c$  in equation (48), represent the vortices  $x_1$  and  $x_1^c$  when i=1, and the cell-centers  $x_1^f$  and  $x_1^{c,f}$  when i=2 and 3. The interpolated velocity  $\tilde{u}_i^{c,f}$  is defined at the cell-centers of the fine grid as following

$$\tilde{u}_{i}^{c,f}(IC_{1},IC_{2},IC_{3}) = \sum_{k=-1}^{2} u_{i}(I-k,IC_{2},IC_{3}) \prod_{j \neq k} \frac{x_{1}^{c}(IC_{1}) - x_{1}(I-j)}{x_{1}(I-k) - x_{1}(I-j)}, \quad (48)$$

where I is the rounded  $IC_1/IPC_1$  to the nearest integer towards zero, for  $\tilde{u}_1^{c,f}$ , and the rounded  $((IPC_1-1)/2+IC_1)/IPC_1$  for  $\tilde{u}_2^{c,f}$  and  $\tilde{u}_3^{c,f}$ .  $IC_i$  are the indices in the computational domain and in the three directions of the cell M. They vary between 0 and  $MC_i+1$ , where  $MC_i+1$  is an integer and the maximum value of the index  $IC_i$ .

Similarly, the anisotropic eddy viscosity,  $\nu_t^{(\pm j)M} = \frac{1}{\sqrt{2}}\mathcal{C}^2\mathcal{L}_k^2 \left|s_{ij}^M\right|^{(\pm j)M}$ , is interpolated as

$$\nu_t^{(\pm j)M}(IC_1, IC_2, IC_3) = \sum_{k=-1}^{2} \nu_t^{(\pm j)M}(I - k, IC_2, IC_3) \prod_{j \neq k} \frac{x_1^{c,f}(IC_1) - x_1^f(I - j)}{x_1^f(I - k) - x_1^f(I - j)}.$$
(49)

If one considers a Taylor expansion at the second order in time of the first derivative of the concentration field at a fixed position, one gets

$$\frac{\partial \tilde{c}}{\partial t}(t_o + \Delta t) = \frac{\partial \tilde{c}}{\partial t}(t_o) + \frac{\Delta t}{2} \frac{\partial^2 \tilde{c}}{\partial t^2}(t_o) + \frac{\Delta t^2}{6} \frac{\partial^3 \tilde{c}}{\partial t^3}(t_o) + \mathcal{O}(\Delta t^2). \tag{50}$$

Now, considering the right-hand-side term  $rhs[\tilde{c}]$  in the mass transport equation (46) at a fixed cell, and at a given time  $t_o$ ,  $\frac{\partial \bar{c}}{\partial t}(t_o)$  can be written as

$$\begin{split} \frac{\partial \tilde{c}}{\partial t}(t_o) &= rhs[\tilde{c}] = \sum_{k=1}^3 \frac{\Delta s_k^M}{\Delta v^M} \left[ -\left(\overline{c}^{(+k)M} \overline{u}_k^{(+k)M} - \overline{c}^{(-k)M} \overline{u}_k^{(-k)M}\right) \right] \\ &+ \sum_{k=1}^3 \frac{\Delta s_k^M}{\Delta v^M} \left[ \left( \frac{1}{Sc} + \frac{\frac{1}{\sqrt{2}} \mathcal{C}^2 \mathcal{L}_k^2}{Sc_t} \right) \left( \left| s_{ij}^M \right|^{(+k)M} \cdot \overline{j}_k^{(+k)M} - \left| s_{ij}^M \right|^{(-k)M} \cdot \overline{j}_k^{(-k)M} \right) \right], (51) \\ \text{where } \frac{\Delta s_k^M}{\Delta v^M} &= \frac{1}{x_k^c (IC_k+1) - x_k^c (IC_k)}, \ j_k^{(\pm k)M} &= \frac{C(IC_k+1) - C(IC_k)}{x_k^{c,f} (IC_k+1) - x_k^{c,f} (IC_k)}, \text{ and where all the variables are considered at } t = t_o. \end{split}$$

As shown in equation (51), at a given cell M and at a given time  $t_o$ , the time derivative of  $\tilde{c}$  can be seen as a linear function of  $\tilde{c}$ ,  $rhs \equiv rhs [\tilde{c}]$ , and  $\frac{\partial^2 \tilde{c}}{\partial t^2}(t_o)$  can be written

$$\frac{\partial^2 \tilde{c}}{\partial t^2}(t_o) = \frac{\partial}{\partial t} \left[ \frac{\partial \tilde{c}}{\partial t}(t_o) \right] = rhs \left[ \frac{\partial c}{\partial t}(t_o) \right] = rhs \left[ rhs \left[ \tilde{c} \right] \right]. \tag{52}$$

Similarly, replacing  $\tilde{c}$  by  $\frac{\partial \tilde{c}}{\partial t}(t_o)$  in equation (52), one obtains

$$\frac{\partial^3 \tilde{c}}{\partial t^3}(t_o) = \frac{\partial}{\partial t} \left[ \frac{\partial^2 \tilde{c}}{\partial t^2}(t_o) \right] = rhs \left[ rhs \left[ \tilde{c} \right] \right]. \tag{53}$$

Using equations (51), (52) and (53), equation (50) is then discretized in time at the second order. One obtains the time-advancement for the concentration at any cell of the grid

$$\frac{c^{n+1}-c^n}{\Delta t} = rhs\left[c^n\right] + \frac{\Delta t}{2}rhs\left[rhs\left[c^n\right]\right] + \frac{\Delta t^2}{6}rhs\left[rhs\left[rhs\left[c^n\right]\right]\right],\tag{54}$$

where the index n is the time-label. Equation (54) can be seen as a Runge-Kutta-like time discretization.

The concentration field is defined at the cell-centers of the fine grid. The convection term  $\overline{c}^{(\pm i)M}\overline{u}_i^{(\pm i)M}$  is calculated with a method of third order in space, QUICK, and is equal to

$$\begin{array}{l} \bullet \ u_{i} > 0 \\ 2 \cdot \overline{c}^{(\pm i)M} \overline{u}_{i}^{(\pm i)M} = -u_{i}^{c,f} (IC_{1}, IC_{2}, IC_{3}) \times \left[ \frac{dx_{i}^{c}(IC_{i}) \cdot C(IC_{i}) + dx_{i}^{c}(IC_{i} - 1) \cdot C(IC_{i} + 1)}{dx_{i}^{c,f}(IC_{i})} \right] + \\ u_{i}^{c,f} (IC_{1}, IC_{2}, IC_{3}) \times \\ \left[ \frac{1}{4} \left[ C(IC_{i} + 1) - C(IC_{i}) - (C(IC_{i}) - C(IC_{i} - 1)) \frac{dx_{i}^{c,f}(IC_{i})}{dx_{i}^{c,f}(IC_{i} - 1)} \right] \right] \\ \bullet \ u_{i} \leq 0 \\ 2 \cdot \overline{c}^{(\pm i)M} \overline{u}_{i}^{(\pm i)M} = -u_{i}^{c,f} (IC_{1}, IC_{2}, IC_{3}) \times \left[ \frac{dx_{i}^{c}(IC_{i}) \cdot C(IC_{i}) + dx_{i}^{c}(IC_{i} - 1) \cdot C(IC_{i} + 1)}{dx_{i}^{c,f}(IC_{i})} \right] + \\ u_{i}^{c,f} (IC_{1}, IC_{2}, IC_{3}) \times \\ \left[ \frac{1}{4} \left[ -(C(IC_{i} + 1) - C(IC_{i})) + (C(IC_{i} + 2) - C(IC_{i} + 1)) \frac{dx_{i}^{c,f}(IC_{i})}{dx_{i}^{c,f}(IC_{i} + 1)} \right] \right], \end{array}$$

where  $dx_i^c(IC_i) = (x_i^c(IC_i+1) - x_i^c(IC_i))$ , and  $dx_i^{c,f}(IC_i) = (x_i^{c,f}(IC_i+1) - x_i^{c,f}(IC_i))$ . The capital letter  $C(IC_i)$  stands for the instantaneous concentration at the centre of the cell whose co-ordinates in the computational domain are  $(IC_i, IC_k, IC_l)$ . Since the grid is only stretched in the normal direction of the walls,  $\overline{c}^{(\pm i)M} \overline{u}_i^{(\pm i)M}$  for i=2 and 3, become simpler

$$\begin{split} &-u_i^{c,f}(IC_1,IC_2,IC_3) \times \\ &\left[\frac{3}{8} \cdot C(IC_i+1) + \frac{3}{4} \cdot C(IC_i) - \frac{1}{8} \cdot C(IC_i-1)\right] \text{ for } u_i > 0 \\ &-u_i^{c,f}(IC_1,IC_2,IC_3) \times \\ &\left[\frac{3}{8} \cdot C(IC_i) + \frac{3}{4} \cdot C(IC_i+1) - \frac{1}{8} \cdot C(IC_i+2)\right] \text{ for } u_i \leq 0 \\ &\text{Finally, } \left|s_{ij}^M\right|^{(+k)M} \text{ is equal to} \end{split}$$

$$\sum_{i=1}^{3} \left| s_{ii}^{M} \right|^{(+k)M} + 2 \times \left( \left| s_{12}^{M} \right|^{(+k)M} + \left| s_{23}^{M} \right|^{(+k)M} + \left| s_{13}^{M} \right|^{(+k)M} \right). \tag{55}$$

 $\left|s_{ii}^{M}\right|^{(+k)M}$  are calculated by a simple second order finite difference, when the three last terms are determined with a second-order scheme as following

$$s_{jk} = \frac{\frac{U_j(I_k+1,I_j) + U_j(I_k+1,I_j-1)}{2} - \frac{U_j(I_k-1,I_j) + U_j(I_k-1,I_j-1)}{2}}{x_k^f(I_k+1) - x_k^f(I_k-1)}$$

$$+\frac{\frac{U_{k}(I_{j}+1,I_{k})+U_{k}(I_{j}+1,I_{k}-1)}{2}-\frac{U_{k}(I_{j}-1,I_{k})+U_{k}(I_{j}-1,I_{k}-1)}{2}}{x_{j}^{f}(I_{j}+1)-x_{j}^{f}(I_{j}-1)}.$$
(56)

Here, the capital letter  $U_i(I_k)$  stands for the instantaneous velocity component in the i-direction at the centre of the cell whose co-ordinates are  $(I_k, I_l, I_p)$ .  $I_k$  are the indexes of the cells in the coarse grid.

### 5.3. The fringe region technique

In many numerical simulations the required computational domains are huge. This is typically the situation of the computation of turbulent mass transfer in a diffusive boundary layer at high Schmidt number along a plane surface. The boundary condition for mass must be set far enough from the wall for not disturbing turbulence in the near-wall region. This computational domain can nevertheless be reduced by an artificial boundary condition [49]. One can then consider a computational domain that contains the diffusive boundary layer only, and that is not extended to the farfield. The fringe region technique was originally introduced by Spalart [50], and has been later used in direct simulations of transitional and turbulent boundary layers, see Bertolotti et al. [51], Spalart et al. [52], Lundbladh et al. [53] and Berlin et al. [54]. The computational domain is divided into one useful region and one fringe region. An extra forcing function was added to the momentum equations in the fringe region to create a periodic

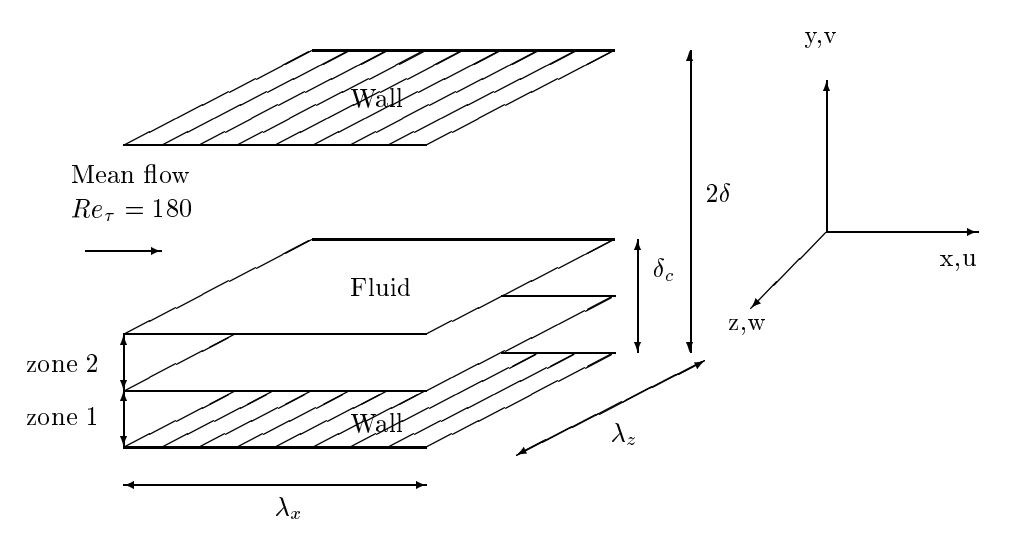


FIGURE 5.1 The geometry of the channel flow, the three regions of computation, and the chosen coordinate system.

problem. The fringe region technique has also been used to suppress the vorticity disturbances close to the outflow boundary in a transitional boundary layer by means of a weighting function [55]. Later, Gurniki et al. [56] used the same kind of weighting functions to suppress the concentration disturbances far from the large gradients of mass transfer in the vicinity of an electrode. Henningson et al. [49] applied this technique with DNS of a turbulent and viscous boundary layer. The fringe technique was used in combination with the Fourier method, and accurate numerical solutions were obtained. They concluded that the fringe region technique was a useful method for the DNS of a viscous boundary layer.

In an electrochemical cell, Schmidt number is very high, and the diffusive boundary layer is located very close to the electrodes. Outside this layer, the distribution of the mean concentration C is almost uniform. It is therefore of less interest to compute the concentrations everywhere in the cell. For that reason, the fringe region technique can be used to reduce the mathematical and the numerical domain of investigation to the near-wall region. This method is exemplified below with the treatment of a diffusive layer near the electrodes of a cell working as a channel flow. For details, the reader is referred to [56, 54]. The computational domain for mass, as shown in figure 5.1, lies between the electrode and an imaginary plane surface in the fluid, parallel to the wall and at a distance of  $\delta_c$  from it.  $\delta_c$  is sufficiently larger than the diffusive and the logarithmic sublayer for mass, and can be estimated as  $\delta_h/Sc^{1/3}$  [19], where  $\delta_h$ is the thickness of the hydrodynamic boundary layer. Here, since the flow is fully developed,  $\delta_h^+$  can be approximated as  $\delta_h^+ = Re_{\tau}$ , and  $\delta_c^+ = 12.5$ , since Sc=3000.  $Re_{ au}$  is here equal to the channel half-width in viscous units. Note that it is actually not possible to determine a diffusive boundary layer because

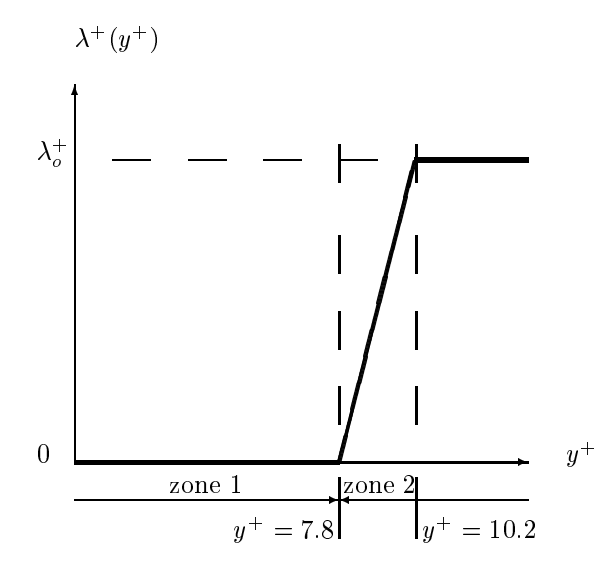


Figure 5.2 The  $\lambda$  function versus the wall-normal direction.

the flow is fully developed. This approximation is however useful to determine where in the near-wall region the gradients of the passive scalar are strongest. The domain is divided into the conservative zone 1 where  $|\nabla \tilde{c}^+| \neq 0$ , and zone 2 where a source term is added to the scalar conservation-equation to force  $\tilde{c}^+$  to approach a given value. This can be done as follows

$$\frac{\partial \tilde{c}^+}{\partial t^+} + \left(\tilde{\mathbf{u}}^+ \cdot \nabla^+\right) \tilde{c}^+ = \frac{1}{Sc} \nabla^{+,2} \tilde{c}^+ - \lambda^+(y^+) \cdot (\tilde{c}^+ - c_o^+),\tag{57}$$

where  $\mathbf{u}^+$  and  $c^+$  denote the instantaneous velocity and concentration fields, respectively.  $c_o^+$  is a constant. Equation (57) can be used for both zones by choosing properly the function  $\lambda^+$ , as shown in figure 5.2. The slope of the ramp function  $\lambda^+$  is here taken equal to 0.13 in viscous units. The source term works as a forcing function, imposing to the intantaneous concentration the fixed value of  $c_o^+$  in zone 2. The height of zone 1 is around the two thirds of  $\delta_c^+$ .

The fringe technique is here used in order to formulate a tractable boundary condition for the instantaneous concentration at the edge of the diffusive boundary layer. At this boundary, the turbulent velocity field induces fluctuations to the concentration. The fluctuating part of the concentration must then be modelled. In order to simplify this fastidious and hazardous task, a very crude model is chosen. The fringe region technique annihilates the fluctuating part of the concentration in the vicinity of the boundary of the reduced domain. It is bluntly assumed that the non-physical phenomena occuring in the fringe region do not invalidate the solution in the remaining part of the computational domain [49] (zone 1 in figures 5.1 and 5.2). This assumption has been verified by numerical experiments in [56].

### CHAPTER 6

# Summary of papers

In this chapter, all the dimensions are given in viscous units. The superscript '+' has been dropped for convenience.

**Paper 1**: Turbulent free convection in large electrochemical cells with a binary electrolyte.

In this paper, the laminar version of the mathematical model proposed by Bark et~al.~[10] for stable stratification in electrochemical enclosures, is extended and tested to two natural turbulent cases. The standard  $k-\epsilon$  model is used for modelling the influence of turbulent fluctuations on the average fields. The commercial code CFX F3D shows good convergence properties for these simulations, and good agreement with previous simulations [11, 57] is obtained. Such simulations include, in addition to the flow variables, velocity components and pressure field for an incompressible fluid, an additional scalar concentration and an elliptic equation for the electrical potential. The electrical potential and the concentration field are directly connected to each other at the electrodes by the boundary condition for mass transfer, and everywhere in the cell by the migration term in the local electroneutrality equation. The non-linear kinetics of the electrochemical reactions at the electrodes are simulated using a formula derived from a Butler-Volmer law. The formula is so far not modified to account for turbulent fluctuations.

For a turbulent case where Schmidt number is equal to 1280 [11], the model predicts a current density at the electrodes varying almost linearly with the vertical direction. In this simulation, the predicted Sherwood number is found to be approximately proportional to the Rayleigh number to the power 0.2.

A flow in a square cavity driven by a temperature difference between vertical walls is also considered. The flow is predicted in good agreement with available data from other investigations [58], which have already been used for benchmarking turbulence models and numerical schemes. Some difficulties for obtaining convergence are observed when the flow is simulated assuming a steady-state. The 'false time stepping' option can be used in order to accelerate the convergence.

**Paper 2**: LES of turbulent channel flow of a binary electrolyte.

The paper focuses on large-eddy simulations of the turbulent diffusive boundary layer in a binary electrolyte. Predictions are performed at Schmidt number equal to 1, 10 and 100. The flow is driven by a pressure gradient, and convection is consequently forced. The code uses an adjusted mesh for the mass conservation equation when Schmidt number varies, and is successfully validated by comparisons with available results found in literature. The Butler-Volmer-like boundary condition is shown to be mathematically equivalent to a constant flux set for concentration when the exchange current density is lower than  $10^{-4}A\ m^{-2}$ , and to a fixed value when the exchange current density is higher than  $10^{-2}A\ m^{-2}$ . For this reason, the calculations do not need to predict the electrical potential in the cell, or at the electrodes. This simplification is valid when considering electrolytes with small electrical potential gradients only.

At Schmidt number equal to one, the exchange current is shown to have no influence on the structure of the mean concentration, neither on the eddy diffusivity, and on the wall-normal turbulent heat flux. However, the RMS intensities, the streamwise turbulent heat flux, and the lateral dimensions of turbulence structures in the near-wall region are influenced.

**Paper 3**: Validation of the fringe region technique in LES of turbulent mass transfer at high Schmidt number.

Large-eddy simulations of mass transfer in a turbulent channel flow working as an electrochemical cell, are considered. The cell runs in the mass transport controlled region, and the electrolyte is binary. Schmidt number is equal to 100 and the turbulent Reynolds number based on the half-width channel to 180. The fringe region technique is tested and validated to reduce the numerical domain of computation to the diffusive boundary layer.

Two different numerical techniques are used for computation of the concentration field in the near-wall region. First, a refined mesh is used for the concentration field and the transport equation is integrated in the whole channel as in [59]. Secondly, in order to make the simulation more efficient, only the near-wall region is considered and the concentration field is damped in the outer region using the fringe technique and thereby the size of the grid is reduced. It turns out that simulations made with the reduced grid and the fringe region technique run approximately 5 times faster than with the complete grid between the two walls.

The mean concentration profile in the direction normal to the walls is computed. Good agreement is found with results from direct numerical simulations by Papavassiliou *et al.* [15].

The concentration profile in the logarithmic region was found to fit well with the logarithmic law of  $\overline{c} = 3.0 \cdot ln(y) + 285.0$  after y = 10.

The mean eddy diffusivity is computed and good agreement is found between the predictions of the present study, the DNS results, and the empirical profile found by Papavassiliou *et al.* [15]. The predictions of the present study with and without the fringe method technique are also in very good agreement.

Streamwise and wall-normal turbulent mass fluxes computed in this study are found in good agreement is found with the computations made by Kawamura et al. [36]

The two-point spanwise correlation coefficient of the concentration fluctuations is computed at y = 1.17. The concentration streak spacing can be estimated to 100. This value is in good agreement with that obtained by Calmet *et al.* [38].

Paper 4: Large-eddy simulation of electrochemical mass transfer.

Large-eddy simulations of mass transfer in a channel flow working as an electrochemical cell are considered. Schmidt number is equal to 3000 and the turbulent Reynolds number, based on the half-width channel, to 180.

The mean concentration profile in the direction normal to the walls is computed. The profile is compared with direct numerical simulations by Papavas-siliou et al. [15] at Sc=2400, and experiments done at Sc=900 by Lin et al. [19]. The concentration profile fits well in the logarithmic region with the law  $\overline{c}=3.0\cdot ln(y)+4485.0$ . At Schmidt number equal to 3000 the logarithmic law lies between y=2 and 10. As found by Kader et al. [41], at very high Schmidt number, the logarithmic law is damped by the constant value of the concentration in the core of the channel.

The mean eddy diffusivity is calculated and good agreement is found between the predictions of the present study, the DNS results of Papavassiliou *et al.* [15], and the empirical profile proposed by Shaw *et al.* [60], stating that  $E_c(y) = 0.000463 \cdot y^3$  in the near-wall region.

The average mass transfer coefficient is calculated. The result of the present study at Schmidt number equal to 3000 is found to be in good agreement with the DNS of Papavassiliou et al. [15], and the theoretical profile found by Shaw et al. [60] for Schmidt numbers between 600 and 32000. The present study finds the intensity of the fluctuations for the wall mass-tranfer coefficient  $\left(\overline{k^2}\right)^{1/2}/\overline{K}$  equal to 0.197. This result is in good agreement with Campbell et al. [17] at the same Schmidt number, where  $\left(\overline{k^2}\right)^{1/2}/\overline{K}$  is found equal to 0.23.

Streamwise and wall-normal turbulent mass fluxes are computed. The streamwise mass-flux is found 30 times larger than in the wall-normal direction. Good agreement is found with the asymptotic laws found by Kawamura *et al.* [36] for Schmidt number between 0.05 and 5.

The presence of well-known streaky structures elongated in the streamwise direction are clearly observed in (x-z) planes at the interface between the viscous and the buffer region of the diffusive boundary layer.

The spectral function of the mass transfer coefficient is computed at the anode. Among the large frequencies, the present study finds a dependency of the spectra proportional to the frequency to the power -3. This result is in very good agreement with an analytical result of Campbell *et al.* [17] based on a linear assumption for the mass-conservation equation.

**Paper 5**: On near-wall turbulent passive-scalar transfer at high Schmidt number.

Large-eddy simulations for turbulent transport of a passive scalar were made at Schmidt numbers equal to 1, 100 and 3000. The purpose of this work was to provide knowledge about the physics of the transport process as input to simplified models for the Reynolds-flux vector at high Schmidt number. The flow Reynolds number was 180. The accuracy of the present computations in the near-wall region was validated by comparisons with analytic expressions in the near-wall-region.

At Schmidt number equal to one, good agreement was found between previous studies and the predictions of the present study. At Schmidt number equal to 3000, the balance in the transport equations of the Reynolds-flux vector is dominated by  $\psi_i$  (the difference between the pressure scalar-gradient term and the diffusive destruction rate) and the transport term  $\mathcal{D}_i$ .  $\psi_x$  and  $\psi_z$  are dominated by the diffusive destruction rate and  $\psi_y$  by the pressure scalar-gradient term.

The transport equation for half the scalar variance and the corresponding dissipation were studied. At high Schmidt number the budget is dominated by the molecular and the turbulent diffusion term, and the production term. For transport equation of the scalar dissipation, no qualitative changes in the structure of the budget were found when Schmidt number varies. The dissipation rate and the turbulent production term dominate the budget, except in the nearwall region.

The numerical experiments made in this study showed that several useful simplifications can be made in the near-wall region for the budgets of the Reynolds-flux, the variance and the dissipation rate. They can be summarized as shown below

$$\begin{array}{ll} \frac{D\overline{u_1\theta}}{Dt} & = & -\epsilon_{\theta 1} + \mathcal{D}_1, \text{ when } y \leq 2. \\ \\ \frac{D\overline{u_2\theta}}{Dt} & = & \Pi_{\theta 2} + \mathcal{D}_2. \\ \\ \frac{D\overline{u_3\theta}}{Dt} & = & -\epsilon_{\theta 3} + \mathcal{D}_3. \\ \\ \frac{Dk_{\theta}}{Dt} & = & \mathcal{P}_{\theta} + \mathcal{D}_{k_{\theta}}. \\ \\ \frac{D\epsilon_{\theta}}{Dt} & = & \mathcal{D}_{\epsilon_{\theta}} + \mathcal{P}_{\epsilon_{\theta}}^1 + \mathcal{P}_{\epsilon_{\theta}}^2 + \mathcal{P}_{\epsilon_{\theta}}^3 - Y, \text{ no simplification.} \end{array}$$

Paper 6: On modelling of Reynolds-flux vector at high Schmidt number.

Large-eddy simulations for turbulent transport of a passive scalar are made at Schmidt numbers equal to 1, 100 and 3000. The flow Reynolds number is 180. The purpose of this work is to provide explicit algebraic models for the Reynolds-flux vector at high Schmidt number.

Two models from previous studies [62, 44] are tested, and one is developed on the basis of a previous work [56] for the budget of the scalar flux. The first model was developed by So *et al.* [62] and is described in tensor form as follows

$$-\overline{u_{i}\theta} = \alpha_{t} \frac{\partial \Theta}{\partial x_{i}} - \frac{\tau}{c_{T1}} \times \left\{ \left[ 2\nu_{t} + (1 - c_{T2})\alpha_{t}\right] S_{ik} + (1 - c_{T2})\alpha_{t}\Omega_{ik} \right\} \frac{\partial \Theta}{\partial x_{k}} ,$$

$$\nu_{t} = c_{T3} \frac{k^{2}}{\epsilon} \left( 1 + \frac{3.45}{\sqrt{Re_{t}}} \right) \tanh\left(\frac{y}{9}\right) , \qquad (58)$$

$$\alpha_{t} = c_{\lambda} \cdot k \cdot \tau \left[ \left( 1 - \left( 1 - e^{-\frac{y}{A}} \right)^{2} \right) \frac{c_{\lambda 1}}{Re_{t}^{1/4}} + \left( 1 - e^{-\frac{y}{A}} \right)^{2} \right] ,$$

where  $S_{ik}$  is the mean strain rate and  $\Omega_{ik}$  the mean rotation rate.

The second model was developed by Wikström *et al.* [44] and is described as follows

$$\frac{\overline{u_i\theta}}{\sqrt{kk_{\theta}}} = -(1 - c_{\theta 4})A_{ij}^{-1} \frac{\overline{u_j u_l}}{k} \Theta_{,l}, \tag{59}$$

where the inverse of the matrix  $\mathbf{A}$  is given by

$$\mathbf{A}^{-1} = \frac{(G^2 - \frac{1}{2}Q_1)\mathbf{I} - G(c_S\mathbf{S} + c_{\Omega}\Omega) + (c_S\mathbf{S} + c_{\Omega}\Omega)^2}{G^3 - \frac{1}{2}GQ_1 + \frac{1}{2}Q_2},$$
 (60)

and  $c_S = 1 - c_{\theta 2} - c_{\theta 3}$ ,  $c_{\Omega} = 1 - c_{\theta 2} + c_{\theta 3}$ .

The third model is developed in paper 6 and can be described as following

$$\begin{cases}
\overline{u\theta} = \frac{-c_{\theta 5}}{\tau^2 c_{\theta 2} c_{\theta 3}(U')^2 - c_{\theta 1}^2} \times \\
\left[ c_{\theta 1} \tau \left( \frac{d}{dy} (\overline{u}_{,y} \overline{\theta}) + c_{\theta 4} \overline{u} \overline{v} \cdot \Theta' \right) + c_{\theta 2} \tau^2 U' \left( \frac{d}{dy} (\overline{v}_{,y} \overline{\theta}) + c_{\theta 4} \overline{v}^2 \cdot \Theta' \right) \right] \\
\overline{v\theta} = \frac{-c_{\theta 6}}{\tau^2 c_{\theta 2} c_{\theta 3} (U')^2 - c_{\theta 1}^2} \times \\
\left[ c_{\theta 3} \tau^2 U' \left( \frac{d}{dy} (\overline{u}_{,y} \overline{\theta}) + c_{\theta 4} \overline{u} \overline{v} \cdot \Theta' \right) + c_{\theta 1} \tau \left( \frac{d}{dy} (\overline{v}_{,y} \overline{\theta}) + c_{\theta 4} \overline{v}^2 \cdot \Theta' \right) \right],
\end{cases}$$
where
$$-\overline{u}_{i,y} \overline{\theta} = \alpha'_{t} \frac{\partial \Theta}{\partial x_{i}} - \frac{\tau'}{c_{T1}} \left\{ \left[ 2\nu_{t} + (1 - c_{T2})\alpha_{t} \right] S_{ik} + (1 - c_{T2})\alpha_{t} \Omega_{ik} \right\} \frac{\partial \Theta}{\partial x_{k}} \\
- \frac{\tau}{c_{T1}} \left\{ \left[ 2\nu_{t} + (1 - c_{T2})\alpha_{t} \right] S_{ik} + (1 - c_{T2})\alpha_{t} \Omega_{ik} \right\}' \frac{\partial \Theta}{\partial x_{k}}.
\end{cases} (61)$$

The superscript ' is equivalent to the first derivative in the wall-normal direction. This last model is based on a simplification of the conservation equation for the Reynolds flux, stating that, at Sc=3000, the transport terms balance the pressure and the dissipation terms.

At Sc=3000 and 100, the model developed in paper 6 is shown to give better results than the two other models.

At Schmidt number equal to 3000, the wall-function of equation (37) in chapter 4.3.3 of this thesis, for the mean passive-scalar, is developed on the basis of a simple algebraic model examined in [61]. Very good agreement is found with the LES computations. This wall-function can be used with a model for the Reynolds-flux vector and a low Reynolds  $k-\epsilon$  model, in order to model mass transport at high Schmidt number.

### CHAPTER 7

## Outlook and critical review

In this work, three main aspects of mass transfer in electrochemical cells have been investigated. The effect of the electrical potential, the effect of natural convection on turbulence and its modelling, and finally the problem of analytically and numerically predicting a turbulent and diffusive boundary layer at very high Schmidt numbers. This last point has been widely studied when the two first were only briefly considered.

The implementation of the electrical potential in the equation system modelling mass transfer in a closed cell was made in paper 1. The turbulent fluctuations of the potential were assumed to be zero. This assumption should be considered in more details, although the methods of investigation to study the field of the electrical potential in an electrolyte are very difficult to carry out.

The study of the potential-fluctuations influence on the potential field require the development of a model for the correlation term between concentration and current fluctuations present in the conservation equation for electrical charges. A model can easily be achieved provided that the fluctuations of the total current (8) can be neglected. This assertion should also be investigated.

Some algebraic Reynolds-flux models have been tested in paper 6 for a flow characterized by forced convection. A similar investigation should be done with natural convection. In this context, the development of LES for buoyancy driven flows would be of great help.

A remaining issue is the modelling of the wall-mass-transfer fluctuations. This topic of importance for many industrial applications, like electroplating, where the uniformity of the metal layers is a condition for the quality of the products. The correlation between bursts events in the buffer layer and the mass-transfer fluctuations mentioned in chapter 2.2 of this study, should be more investigated in the future. In particular, the process by which fluctuations of the velocity field are induced to chemical species in the diffusive sublayer and at the electrodes surface, could be a field of research for a future work.

A new wall-function for mass has been examined in paper 6. Good agreement was found with a large-eddy simulation. In the future, this function should also be tested for a flow induced by natural convection.

# Acknowledgments

This project is carried out within the Faxén Laboratory at the Royal Institute of Technology (KTH). The financial support of the Swedish Nationial Board for Industrial and Technical Development (NUTEK), and the industrial sponsors within ABB and EKA Chemicals, is gratefully acknowledged. Special thanks to Rolf Karlsson at Vattenfall Utveckling in Älvkarlby for continuing interest in my work.

I want to thank my supervisors, Prof. Fritz Bark and Doc. Said Zahrai, for their constructive ideas, support and encouragement. Special thanks to Jesper Oppelstrup from NADA Institution at KTH for constructive discussions and active support in my research. Michael Vynnycky from the Faxén Laboratory was also of good help some couple of times, both technically and linguistically.

The author is very grateful for many valuable discussions with Dr. Ed Fontes and M.Sc. Phil Byrne on various matters that are dealt with in the present work. Finally, thanks to all my colleagues at the Department of Mechanics and at the Department of Applied Electrochemistry, for good compagny, especially to the French community, whose presence is infinitely pleasant; Gérald Audénis, Patrick Boissoneau, Jérôme Ferrari, Franck Grégoire, Nicolas Moch, and Pedro Olivas.

Special thanks to Kristine Andersson, Suzanne Fallqvist, Sven-Åke Heed, Staffan Lang and Tiina Rosenberg, who made me discover something called Sweden. Thanks to Sylvain Briens, Pierre Cuny and Antoine Labrosse, who convinced me, one evening 1993 to go to Sweden and take a look up there.

# **Bibliography**

- [1] M.E. Bowden, et al., Beckmen Center for the History of Chemistry, http://www.public.iastate.edu/ iachemed/FIPSE/RESOURCES/ELECTROCHEM/history.html
- [2] P.M. Wikström, Measurement, Direct Numerical Simulation and Modelling of Passive Scalar Transport in Turbulent Flows, Doctoral Thesis, ISRN KTH/MEK/TR-98/11-SE (1998), Royal Institute of Technology, Department of Mechanics, S-10044 Stockholm, Sweden.
- [3] R.M.C. So and T.P. Sommer, Int. J. Heat Mass Transfer, 39 (1996) 455.
- [4] A. Bejan, Convection heat transfer, a Wiley-Interscience publication, 2<sup>nd</sup> edition (1995)
- $[5]\ {\rm V.G.}\ {\rm Levich},\ Physicochemical\ hydrodynamics}\ {\rm Ed.\ Prentice-Hall}\ (1962)\ 293.$
- [6] C.S. Lin, R.W. Moulton and G.L. Putnam, Industrial and Engineering Chemistry 45 (1952) 636.
- [7] R.J Goldstein, H.D. Chiang and D.L. Lee, J. Fluid Mech. 213 (1990) 111.
- [8] M.G. Fouad and N. Ibl, Electrochimica Acta 3 (1960) 233.
- [9] J.S. Newman, Electrochemical systems, second Ed., University of California, Berkeley, Ed. Prentice Hall, ISBN 0-13-248758-6.
- [10] Bark F.H. and F. Alavyoon, J. Fluid Mech., 290 (1995) 1.
- [11] D. Ziegler and J.W. Evans, J. Electrochem. Soc., 133 (1986) 559.
- [12] S.K. Robinson, Annu. Rev. Fluid Mech. 23 (1991) 601.
- [13] R.F. Blackwelder and R.E. Kaplan, J. Fluid Mech., 76 (1976) 80.
- [14] V. Johansson, P.H. Alfredsson and J. Kim, J. Fluid Mech., 224 (1991) 579.
- [15] D.V. Papavassiliou and J. Thomas Hanratty, Int. J. Heat Mass Transfer, 40 (1997) 1303.
- [16] F. Gurniki, S. Zahrai and F.H. Bark, J. of Appl. Electrochemistry, 29 (1999) 27.
- [17] J.A. Campbell and T.J. Hanratty, A. I. Ch. E. Journal 29 (1983) 221.
- [18] W.D. McComb, The physics of fluid turbulence, Oxford University Press (1990).
- [19] C.S. Lin, R.W. Moulton and G.L. Putnam, Industrial and Engineering Chemistry, 45 (1953) 636.
- [20] A.P. Colburn, Ind. Eng. Chem., 22 (1930) 967.
- [21] T.K. Sherwood, Trans. Am. Inst. Chem. Engrs., 36 (1940) 817.
- [22] O. Reynolds, Manchester Literary and Philosophical Soc., 8 (1874).
- [23] L. Prandtl, Physik Z., 29 (1928) 487.
- [24] G.I. Taylor, Great Britain Advisory Comm. Aeronaut. Rept. Mem., 2272 (1917).
- [25] Kármán T. von, Trans. Am. Soc. Mech. Engrs., 61 (1935) 705.
- [26] L.M.K. Boelter, R.C. Martinelli and F. Jonassen, Trans. Am. Soc. Mech. Engrs., 63 (1941) 447.
- [27] R. Reichardt, Natl. Advisory Comm. Aeronaut. Tech. Mem., 1047 (1943).
- [28] F. Walsh (1993), A first course in electrochemical engineering, The Electrosynthesis Co Inc., Romsey, ISBN 0 9517307 1 1.
- [29] S. Ostrach (1968), Completely confined natural convection, Development in Mechanics, Vol.4, Proc. Tenth Midwestern Mechanics Conf., Johnson Publ. Co., Fort Collins, CO, 53.

- [30] S. Ostrach (1982), Natural convection heat transfer in cavities and cells, Proceedings of Seventh International heat Transfer Conference, Munich, Vol.1, Hemisphere Publishing Corp., Washington DC, 365.
- [31] Ch.W. Tobias and R.G Hickman, it Zeitschift für physikalische Chemie, 229 (1965) 145.
- [32] A. Acrivos, Chem. Eng. Sc., 21 (1966) 343.
- [33] K. Kitamura and F. Kimura, Int. J. Heat Mass Transfer, 38 (1995) 3149.
- [34] J. Boussinesq, Essai sur la théorie des eaux courantes, Mém. Prés. Acad. Sci., 3rd edition, Paris XXIII, 46 (1877).
- [35] D.C. Wilcox, Turbulence modeling for CFD, DCW Industries Inc. (1993).
- [36] H. Kawamura, K. Ohsaka, H.Abe and K. Yamamoto, Int. J. Heat Fluid Flow, 19 (1998) 482.
- [37] B.A. Kader, Int. J. Heat Mass Transfer 24 (1981) 1541.
- [38] I. Calmet and J. Magnaudet, Phys. Fluids, 9 (1997) 438.
- [39] B.E. Launder and D.B. Spalding (1973), Comp. Meth. in Appl. Mech. and Eng., Vol.3,
- [40] CFX-F3D release 3.3: User Manual, AEA Technology-Computational Fluid Dynamics Services, Building 8.19, Harwell Laboratory, Oxfordshire OX11 0RA, UK, 1994.
- [41] B.A. Kader and A.M. Yaglom, Int. J. Heat Mass Transfer, 15 (1972) 2329.
- [42] H. Abe, H. Kawamura and Y. Matsuo (1998), DNS of turbulent heat transfer in channel flow: near-wall turbulence quantities, Monash University, Melbourne, Australia, 13-18 december 1998
- [43] S. Wallin and A.V. Johansson, J. Fluid Mech., 403 (2000) 89.
- [44] P.M. Wikström, S. Wallin and A.V. johansson, it Phys. Fluids 12 (2000) 688.
- [45] S. Zahrai, F.H. Bark (1995), R.I Karlsson, Eur. J. Mech., B/Fluids, 14 (1995) 459.
- [46] Edited by M. Hallbäck, D.S. Henningson, A.V. Johansson and P.H. Alfredsson (1996), Department of Mechanics, Royal Institute of Technology, Stockholm, Sweden, *Turbulence and transition modelling*, Ercoftac series, Vol.2, 271.
- [47] J.W. Deardorff, J. Fluid Mech., 41 (1970) 453.
- [48] Y. Miyake, Computational Fluid Dynamics, Ed. M. Yasuhara & H. Daiguji, Chap.10, p.223, (1992) Univ. Tokyo Press.
- [49] J.Nordström, N. Nordin and D. Henningson, The fringe technique and the Fourier-method used in the direct numerical simulation of spatially evolving viscous flows, SIAM J. Sci. Comp. 20 (1999), 1365.
- [50] P.R.Spalart, Direct numerical study of leading edge contamination, in Fluid Dynamics of Three-Dimensional Turbulent Shear Flows and Transition, AGARD-CP-438, 1988, pp.5.1-5.13.
- [51] F.P. Bertolotti, Th. Hebert and P.R. Spalart, it J. Fluid Mech., 242 (1992) 441.
- [52] P.R. Spalart and J.H. Watmuff, J. Fluid Mech. 249 (1993) 337.
- [53] A. Lundbladh, P.J. Schmidt, S. Berlin and D.S. Henningson, Simulations of Bypass Transition for Spatially Evolving Disturbances, in Proceedings of AGARD Symposium on Applications of Direct and Large-eddy Simulation of Transition and Turbulence, AGARD-CP-551, 1994, pp.18.1-18.13.
- [54] S. Berlin, A. Lundbladh and D.S. Henningson, Phys. Fluid 6 (1994) 1949.
- [55] M. Kloker, U. Konzelmann and H. Fasel, AIAA J., 31 (1993) 620.
- [56] F. Gurniki, S. Zahrai and F.H. Bark, 3<sup>rd</sup> Symposium on Turbulence, Heat and Mass Transfer, Nagoya, april 2-6 2000, Y.Nagano, K.Hanjalić and T.Tsuji (Editors), © Aichi Shuppan.
- [57] J.W. Elder, J. Fluid Mech., 23 (1965) 99.
- [58] Henkes R.A. and Hoogendoorn C.J., Num. Heat Transfer, 28 (1995) 59.
- [59] F. Gurniki, S. Zahrai and F.H. Bark, J. of Applied Electrochemistry, 30 (1999) 0.
- [60] Shaw D.A. and Hanratty T.J., A. I. Ch. E. Journal 23 (1977) 160.

- [61] P.M. Wikström, M. Hallbäck and A.V. Johansson, Int. J. of Heat and Fluid Flow, 19 (1998) 556.
- $[62]\,$  R.M.C. So and T.P. Sommer, Int. J. Heat Mass Transfer, 39 (1996) 455.

# Paper 1

P1

# TURBULENT FREE CONVECTION IN LARGE ELECTROCHEMICAL CELLS WITH A BINARY ELECTROLYTE

François Gurniki<sup>1</sup>, Said Zahrai<sup>2</sup> and Fritz H. Bark<sup>1</sup>

- <sup>1</sup> Faxén Laboratory, KTH, Stockholm, S-10044 Sweden
- <sup>2</sup> ABB, Corporate Research, S-72178 Västerås, Sweden

Abstract. A mathematical model proposed by Bark and Alavyoon [1] for modelling laminar natural convection in electrochemical cells, with binary electrolytes, is extended to simulation of two-dimensional turbulent flows. The turbulence was modeled by a standard  $k - \epsilon$  model. The constants used in the model are the same as those used by Henkes and Hoogendoorn [3]. Steady state calculations were carried out in a square, differentially heated enclosure for  $Gr = 7 \times 10^{10}$  and Pr = 0.71. The turbulence model used could not predict the transition effect on the Nusselt number along the hot wall. Transient calculations performed in an enclosure with an aspect ratio of 35, for  $Gr = 6.4 \times 10^{11}$  and Sc = 2763, revealed large scale fluctuations in the boundary layers near the vertical walls. The model was able to predict qualitatively the velocity field for transitional flow for air induced by buoyancy at  $Gr_h = 8100$  and  $Gr_h = 22500$ . The correlation between the Sherwood and Rayleigh numbers was studied by modelling the mass transfer at the electrodes using a Butler-Volmer Law. The computed Sherwood number was found to be approximately proportional to the Rayleigh number to the power of 0.2 in the range of  $Ra_h$  between  $5 \times 10^8$  and  $10^{10}$ , and with an order of magnitude of  $10^5$ .

### 1. Introduction

Electrochemical cells appear in several industrial applications, such as copper refining cells and lead-acid batteries. It turns out that between the different transport mechanisms, convection, migration and diffusion, convection controls in most applications. The fact that the liquid moves due to buoyancy influences the process considerably. The efficiency of the transport mechanisms in turn directly influences the process of interest in the cell. Therefore, during the past few years, hydrodynamics of electrochemical cells have been subject to many scientific and industrial investigations.

Eklund et al. [2] studied the flow in a copper refining cell both numerically and experimentally. The concentration field was measured by Holographic Laser Interferometry and the velocity profiles using Laser-Doppler Velocimetry. The theoretical model was based on hydrodynamic conservation laws. Electrodes kinetics were modeled with a constant concentration flux for copper ions at the electrodes. Very good agreement between theoretical predictions and experimental measurements was found.

In a theoretical investigation, Bark and Alavyoon, [1], considered free convection in an electrochemical system with nonlinear reaction kinetics and a binary electrolyte. Unsteady electrolysis was investigated for large values of Rayleigh and Schmidt numbers. The charge transfer at the electrodes was mathematically quantified by a Butler-Volmer law. Using perturbation theory, the authors derived a simplified model for the evolution of the system. They found good agreement with results from numerical solutions of the full problem.

Computation of turbulent flow set up by inhomogeneities in the density field , in a closed cavity, is not free from difficulties. The case of flow in a differentially heated square cavity has recently been used as a test for turbulence models and numerical procedures. Henkes and Hoogendoorn [3] reported results of computation of turbulent natural convection in enclosures. The comparison, between different models and solution schemes, aimed at diminishing numerical inaccuracies and at obtaining a numerical reference solution for the differentially heated squared enclosures. To investigate numerical accuracy, a well-defined configuration was prescribed, and the standard  $k-\epsilon$  model was used as the reference model. Although results close to experimental data were presented, distinct inconsistencies were observed. Computational difficulties such as slow convergence were noted.

In the present work, attention has been paid to flows where turbulent transport has to be taken into account. The commercially available code, CFX F3D, is used for a more detailed investigation of the case studied by Ziegler and Evans [4]. Their work is extended by, first more accurate simulations and models. Secondly, a more sophisticated, non-linear Butler-Volmer law as the boundary condition at the electrodes, is used for the description of the electrodes kinetics. Detailed comparisons are made between predicted results and the literature, for two flow cases.

### 2. Problem formulation

Two electrodes made from same metal are immersed in a dilute solution of a salt of the electrode metal providing a binary electrolyte in a rectangular cell. The two-dimensional cell, which is assumed to have its sides parallel to the direction of gravity, is shown in figure 1. The dissolution of metallic ions generally increases the density of the fluid near the anode. Near the cathode, the reverse reaction takes place resulting in a lower density. Inhomogeneities in the density field set the fluid in motion with a convection pattern downwards near the anode and upwards near the cathode. Convection contributes to transport of ions and thereby influences the chemistry of the cell. The mathematical model considered by Bark and Alavyoon [1] is reviewed and extended to investigate the case of turbulent flows. The standard turbulence  $k - \epsilon$  model is used. The present study performed also numerical predictions for the case of Ziegler et al. [4] with the low-Reynolds number model. As reported by Jones and Launder [5]

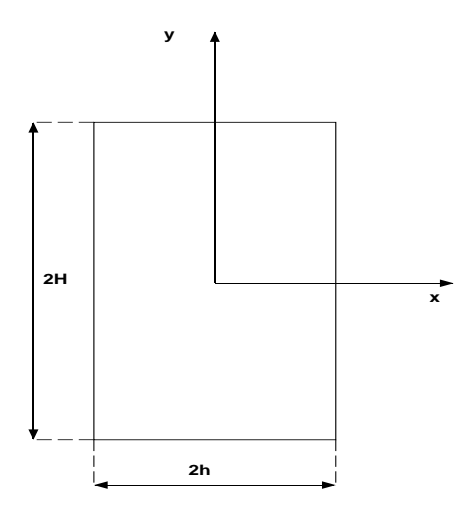


FIGURE 1. The geometry of the cell and the chosen coordinate system.

for a two-dimensional flow and natural convection, the low-Reynolds version was found to produce a numerically unstable solution. For that reason, the results with the low-Reynolds version are not shown in the present study. The hydrodynamic problem must be solved for 6 dependent variables in a two-dimensional configuration: the concentration fields,  $c_1$  and  $c_2$ , where subscript 1 denotes the anion, and subscript 2, the corresponding cation, the velocity field  $\vec{u} = (u, v, 0)$ , the pressure field p and the electric potential  $\phi$ . Apart from the double layers, the electrolyte can be assumed to be electrically neutral, that is  $z_1c_1 + z_2c_2 = 0$ , where z denotes the charge number of the species and the indices 1 and 2, the metallic and the non-metallic ionic species respectively. If the double layer is not to be explicitly accounted for, the mathematical problem can be formulated using a single variable for the concentration fields by defining  $c = z_1 c_1 = -z_2 c_2$ , which satisfies the neutrality condition. The governing equations for the above 5 independent variables assume however, for simulation of turbulent flows, additional terms and equations to take into account the effects of random temporal and spatial fluctuations. Introducing f as the time-average value of any variable, and f' its fluctuating part, and introducing the turbulent kinetic energy  $k = \frac{1}{2} \overline{u_i'^2}$ (  $m^2$   $s^{-2}$ ), and a rate of turbulent kinetic energy dissipation  $\epsilon$  (  $m^2$   $s^{-3}$ ), the following system of equations is obtained for  $z_1 = -z_2 = 2$ 

$$\frac{\partial \vec{u}}{\partial t} + Ra_h \vec{u} \cdot \nabla \vec{u} = Sc \left( -\nabla p + \nabla^2 \vec{u} - c\vec{e_y} \right) + \frac{1}{D} \nabla \cdot \left( \nu_T \left( \nabla \vec{u} + (\nabla \vec{u})^T \right) \right), \quad (1)$$

$$\nabla \cdot \vec{u} = 0, \tag{2}$$

$$\frac{\partial c}{\partial t} + Ra_h \vec{u} \cdot \nabla c = \nabla^2 c + \frac{1}{\sigma_T D} \nabla \cdot (\nu_T \nabla c), \qquad (3)$$

$$\Gamma \nabla \cdot (1+c) \,\nabla \phi + \nabla^2 c = 0,\tag{4}$$

$$\rho \frac{\partial k}{\partial t} + \rho \nabla \cdot (k\vec{u}) - \nabla \cdot \left( \left( \mu + \frac{\mu_T}{\sigma_k} \right) \nabla k \right) = P + G - \rho \epsilon, \tag{5}$$

$$\rho \frac{\partial \epsilon}{\partial t} + \rho \nabla \cdot (\epsilon \vec{u}) - \nabla \cdot \left( \left( \mu + \frac{\mu_T}{\sigma_{\epsilon}} \right) \nabla \epsilon \right) = C_1 \frac{\epsilon}{k} P - C_2 \rho \frac{\epsilon^2}{k}, \tag{6}$$

where,

$$\mu_T = C_{\mu} \rho \frac{k^2}{\epsilon}, \qquad \mu_{eff} = \mu + \mu_T,$$

$$P = \mu_{eff} \nabla \vec{u} \cdot \left( \vec{u} + (\vec{u})^T \right), \quad G = \frac{-\mu_{eff}}{\rho \cdot \sigma_T} \vec{g} \cdot \nabla \rho.$$

 $Ra_h$ , Sc, D and  $\Gamma$  are defined as

$$Ra_h = \frac{\rho_o Cgh^3(\alpha_1 + \alpha_2)}{2\mu D}, \quad Sc = \frac{\mu}{\rho_o D},$$
 (7)

$$D = \frac{2D_1 D_2}{D_1 + D_2}, \quad \Gamma = \frac{2(D_1 + D_2)}{D_1 - D_2}.$$
 (8)

C is defined as min  $\left[\frac{hi_0}{FD_1} \times \sinh\left[\frac{F}{RT}(V_+ - V_+)\right], c_o\right]$  [1], or min  $\left[\frac{hi}{2FD_1}, c_o\right]$  when  $\frac{\partial C}{\partial n}$  is set constant at the electrodes [4]. The above system is set for the non-dimensional variables  $\vec{x}^*$ ,  $\vec{v}^*$ ,  $t^*$ ,  $\phi^*$ ,  $\vec{i}^*$  and  $c^*$ , where \* superscripts are dropped. The non-dimensional variables can be defined as

$$\vec{x} = \vec{x}^* h, \quad \vec{v} = \frac{\rho_o C g h^2 (\alpha_1 + \alpha_2)}{2\mu} \vec{v}^*, \quad t = \frac{h^2}{D} t^*,$$
 (9)

$$\phi + \frac{V_{+} + V_{-}}{2} = \frac{RT}{F} \phi^{*}, \quad \vec{i} = i_{0} \vec{i}^{*}, \quad c^{*} = \frac{c - c_{o}}{C}.$$
 (10)

A series of numerical calculations, calculated for the turbulent case of Ziegler et al. [4], proved that G does not influence the prediction of the mean velocity, and can be neglected in the transport equation for k.

Ozoe [6] performed a sensitivity analysis for the constants of the  $k-\epsilon$  turbulent model and determined different values for  $C_1$  and  $\sigma_T$  rather than those listed below. However, since the applicability of these values for different geometric and boundary conditions is not known, they were not employed here. The turbulent constants are therefore chosen as Henkes [3], except for  $C_{\epsilon}$  in the buoyant term of the  $\epsilon$  equation, which was shown to have no significant influence on the solutions:  $C_1 = 1.44, C_2 = 1.92, C_{\epsilon} = 0, C_{\mu} = 0.09, \sigma_T = 0.9, \sigma_k = 1$  and  $\sigma_{\epsilon} = 1.3$ .

A turbulent contribution should also be taken into account for the calculation of the electrical potential. Here, it is assumed that the turbulent contribution is negligible.

Bark and Alavyoon [1] used a semi-empirical Butler-Volmer law and formulated the following non-dimensional boundary conditions at the anode and cathode

$$\frac{\partial c}{\partial x} = \begin{cases}
\frac{hi_0}{2FD_1C} \left[ e^{(V-\phi)} - (1+c)e^{(\phi-V)} \right] & \text{at x=-1, } |y| \leq H \text{ (anode)} \\
-\frac{hi_0}{2FD_1C} \left[ (1+c)e^{(\phi+V)} - e^{-(\phi+V)} \right] & \text{at x=+1, } |y| \leq H \text{ (cathode)}
\end{cases}$$
(11)

where  $V = \frac{F}{2RT}(V_+ - V_-)$ , and  $H = \frac{H}{h}$ . Here the formula was not modified to account for turbulent fluctuations. Ziegler and Evans [4], used a simpler condition

$$\frac{\partial c}{\partial x} = \text{constant.} \tag{12}$$

For the electrical potential, because  $\vec{N}_2 \cdot \vec{e}_x = \vec{0}$  at  $x = \pm 1$ ,

$$(1+c)\frac{\partial\phi}{\partial x} = \frac{1}{2}\frac{\partial c}{\partial x}$$
 at  $x = \pm 1, |y| \le H$  (anode, cathode) (13)

No transfer of mass occurs at the horizontal walls, resulting in vanishing normal derivatives of the concentration and potential fields

$$\frac{\partial c}{\partial y} = \frac{\partial \phi}{\partial y} = 0 \text{ at } y = \pm H, |x| \le 1.$$
 (14)

For the velocity field, no slip conditions are applied on all four walls, that is

$$\vec{u} = \vec{0} \text{ at } x = \pm 1 \text{ and } y = \pm H. \tag{15}$$

### 3. Methodology

The set of equations is solved numerically using the commercial code CFX F3D [7]. The solution methodology is based on the finite volume discretization of the transport equations and the continuity equation for an incompressible fluid. The numerical scheme is based on the pressure correction method. The pressure-correction equation is obtained by applying the SIMPLE algorithm [8] to the momentum equations. The Rhie and Chow [9] interpolation scheme is used to prevent chequerboard oscillations of pressure on the co-located grid. In the present computations, full field Stone's method was used to solve the velocity variables, concentration and the preconditioned conjugate gradients for pressure. The advection term was discretized using an upwind method for steady computation. During simulation of unsteady flow, in addition to the finer mesh, CCCT [10], which is a more stable formulation of the QUICK scheme, was used. The use of CCCT decreases numerical diffusions and makes a study of small fluctuations possible.

### 4. Results

In this section, results from numerical investigations of the two-dimensional flow in an electrochemical cell are presented. The Rayleigh and Grashof number are based on the half-width of the cell. The same parameters used by Ziegler and Evans [4], are first chosen so that the results can be compared with their theoretical and experimental investigations. The flow is then studied in more detail. The flow is assumed to take place in a cell with a width of 2.4~cm and a height of 85~cm. The Rayleigh number is  $5\times10^9$  and the Schmidt number 2763. The vertical walls of the cell form the anode and cathode, where mass flux is set constant. The horizontal walls are electrically isolated. A detailed set of the parameters involved in the simulation is given in table 1.

Quantity	Value	
Ionic metal	Cadmium, $Cd^{++}$	
Average salt diffusivity	$5.76 \times 10^{-10} \ m^2 s^{-1}$	
Average viscosity	$1.91 \times 10^{-3} kg \ (m.s)^{-1}$	
Average density	$1200 \ kg \ m^{-3}$	
Relative variation in density		
with solute fraction	1.97	
Reference concentration	0.0937 (mass fraction)	
Anode-cathode spacing	$0.024 \ m$	
Cell height	$0.85 \ m$	
Current density	$100~A~m^{-2}$	

TABLE 1: Physical parameters of the flow studied by Ziegler and Evans [4].

The simulation was started with a mesh similar to that used by Ziegler and

The simulation was started with a mesh similar to that used by Ziegler and Evans,  $32 \times 22$  mesh points in the vertical and horizontal directions, respectively. As in that work, the equations were solved assuming a steady state and the standard form of the  $k-\epsilon$  turbulence model. Figure 2 shows the mean vertical velocity at the mid-height of the cell. The predicted velocity profile agrees qualitatively well with the experimental data. The same calculation was repeated with a finer mesh using  $200 \times 50$  mesh points in the vertical and horizontal directions, respectively. In order to study the possible oscillations, after the initial transients are dampened out, the flow was first simulated under assumption of steady-state. Thereafter, the simulation was continued as a time dependent flow. Figure 3 shows a comparison between the predicted vertical velocity profile, as a function of time, and the measurements of Ziegler and Evans. The agreement with experimental data, compared to that of figure 2, is clearly improved. The thickness of the boundary layer on the wall is nicely predicted. Figure 4 shows the present simulation of the maximum velocity inside the boundary layer at the mid-height of the cell as a function of time. After about 20 s, regular fluctuations

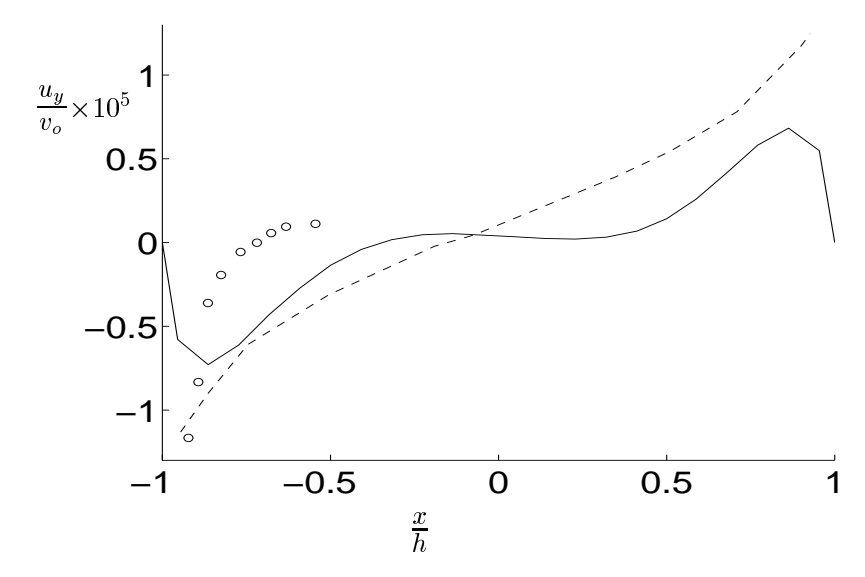


FIGURE 2. The vertical mean velocity at the mid-height of the cell. The result from the present computation, the solid line, is compared with theoretical, dashed line, and experimental data, dots, obtained by Ziegler and Evans.  $Ra_h = 5 \times 10^9, Sc = 2763$ .

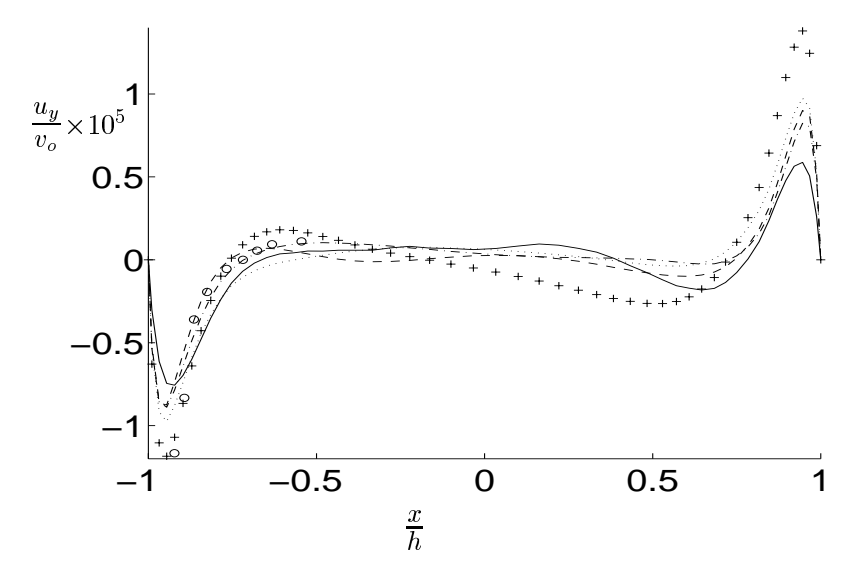


FIGURE 3. The vertical mean velocity at the mid-height of the cell, at different moments of time, for the first 20 seconds, at each 5 seconds. The dots represent the experimental data by Ziegler and Evans.  $Ra_h = 5 \times 10^9, Sc = 2763$ .

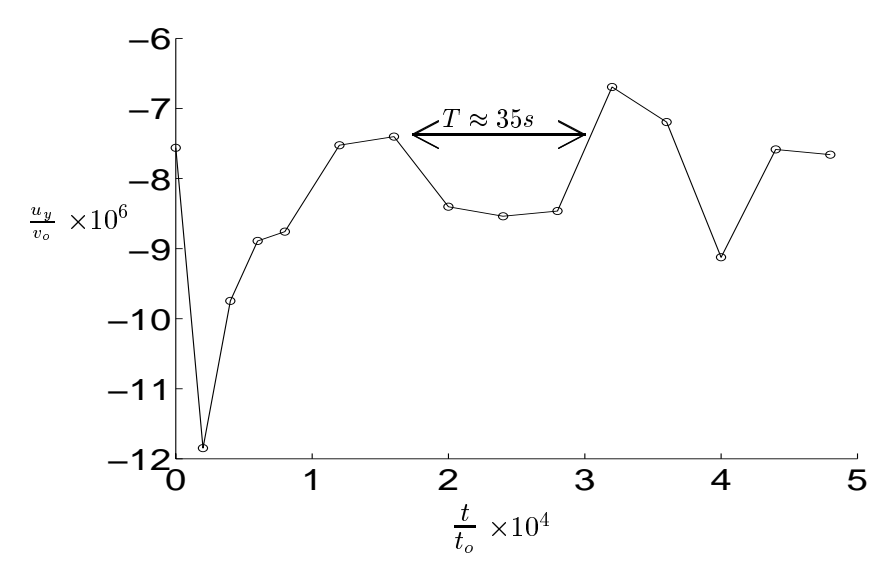


FIGURE 4. The maximal vertical mean velocity in the boundary layer near the anode, in an horizontal cross-section of the cell at its mid-height, as a function of time.  $Ra_h = 5 \times 10^9, Sc = 2763$ .

with a period of about 35 s, is observed. The magnitude of the fluctuations is less than 10% of the mean value.

The maximum mean velocity at the mid-height of the cell is  $-6.75 \times 10^{-4}~m~s^{-1}$ . By comparing this vertical velocity, with the period of fluctuations and the width of the cell, fluctuations in the velocity field can be attributed to advection of wave-like eddies whose size is of the same order of magnitude as the width of the cell. Figure 5 shows that a wavy structure can be found in the boundary layer, with a wavelength comparable to the width of the cell. The waves travel at a speed close to that of the maximum velocity in the wall-layer.

For the same geometry, with two heated vertical walls, a Prandtl number of 7 and Rayleigh numbers based on the half-width of the cell around  $7.234 \times 10^5$ , Elder [11] observed a similar wavy boundary layer structure and similar trend in the wavelength. Elder stated that the wall waves appeared when the flow was close to transition to turbulence and could be seen as instabilities in the boundary layer. The wave train lost its regularity as the turbulent state was approached.

At higher current densities, the flow becomes, loosely speaking, more like conventional turbulence, where small scale turbulent fluctuations become dominant, in comparison with large structures of sizes comparable to the width of the cell. Figure 6 shows the increase in mean velocity with current density. The calculations were run using a coarse grid, which, as previously shown, predicted the flows qualitatively well.

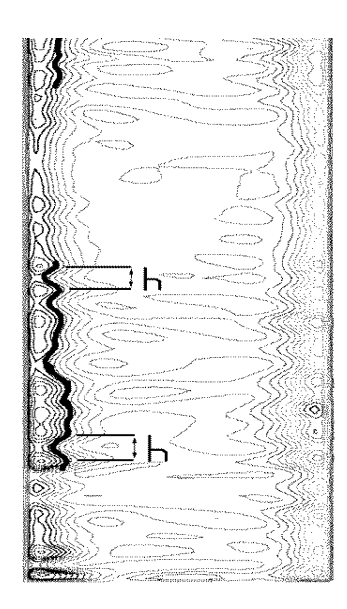


FIGURE 5. Iso-lines of vertical velocity. The horizontal dimension is expanded by a factor 10. Distances equal to the width of the cell are marked at two different vertical positions.  $Ra_h = 5 \times 10^9, Sc = 2763$ .

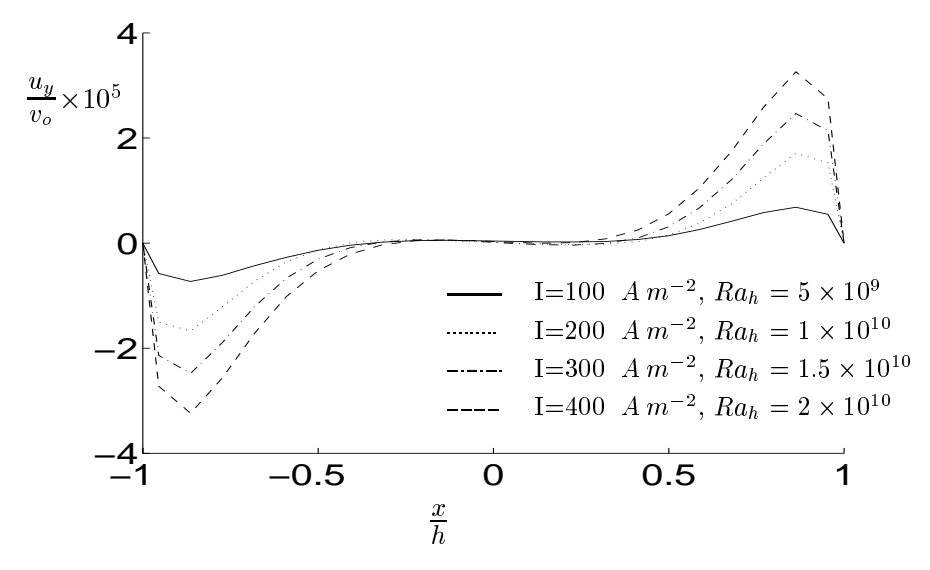


Figure 6. The influence of the current density on the velocity field for constant values of current density on the electrodes. Sc=2763.

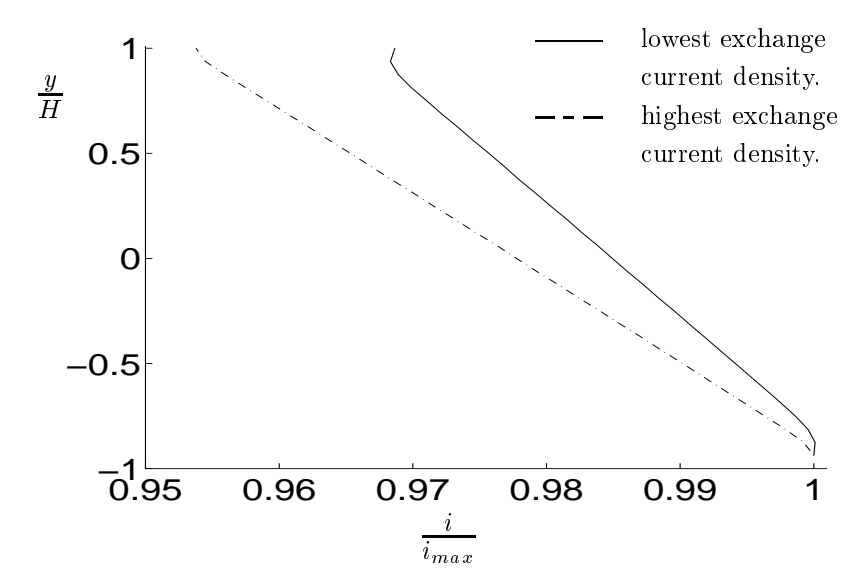


FIGURE 7. The predicted current density distribution using the Butler-Volmer law at two different exchange current densities. The current density is normalized by the maximal predicted value. The solid line corresponds to the lower value of the exchange current density,  $1 A m^{-2}$  and the dashed line to the case, 10 times higher.

It was found empirically on the basis of the computational effort of the present study, that the maximal mean velocity is approximately given by the relation

$$v_{max} = \lambda \times i^{0.51},\tag{16}$$

where  $v_{max}$  and i are given in  $m \ s^{-1}$  and  $A \ m^{-2}$ , respectively, and  $\lambda = 1.23 \times 10^{-4} \ m^{2.02} \ s^{-1} A^{-0.51}$ . This relation is in relative agreement with the one found out by Ziegler and Evans, who found  $\lambda = 2.33 \times 10^{-4} \ m^{2.02} \ s^{-1} A^{-0.51}$ . In accordance with Ziegler and Evans, a constant current density was imposed at the electrodes. An alternative way, of modelling the charge transfer at the electrodes, is use a Butler-Volmer law. It allows a study of the influence of current density distribution on flow. However, as discussed by Bark et al. [1], the use of it, due to numerical complexities, limits the computations to very low cell potential drops. Figure 7 shows the current density distribution along the cathode for two different exchange current densities. The computed current densities are normalized by dividing by their maximum value, which, according to figure 7, was found, as expected, at the bottom of the cell. The exchange current density was varied by a factor of 10, between the two cases, resulting in a maximal computed current density of about 3 times larger for the highest value. The current density varied linearly in the vertical direction apart from the close neighbourhood to the vertical boundaries. The imposed potential difference between anode and cathode was 0.014~V in the above simulation.

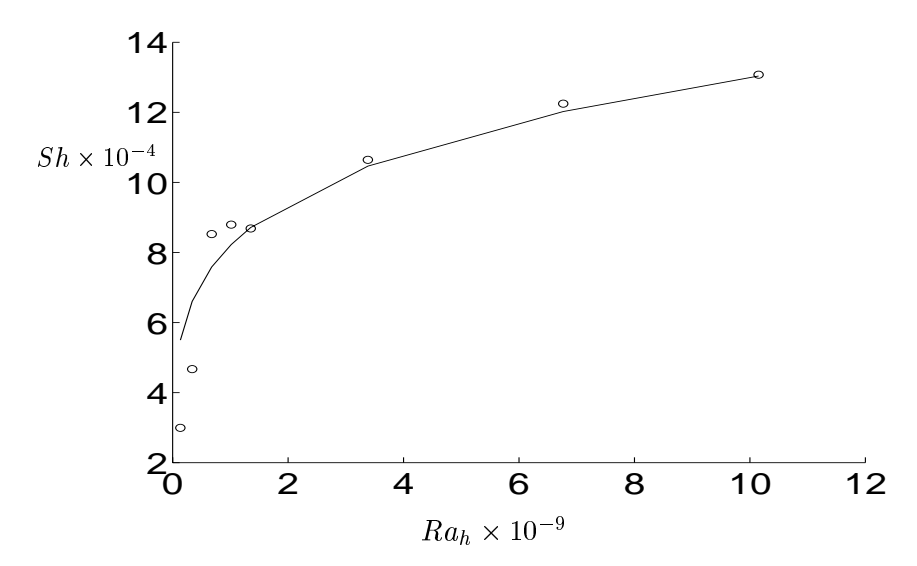


FIGURE 8. The variation of Sherwood number for different Rayleigh numbers. Diamonds show the predicted Sherwood numbers, while the solid line presents the empirical correlation curve  $Sh = Ra_h^{0.2}$ .

The Sherwood number is the non-dimensional mass flux at the electrodes, and is defined as  $\frac{H}{C_{wall}-C_{\infty}}\left[\frac{\partial C}{\partial n}\right]_{wall}$  [12]. Here attention is paid to the qualitative dependence of the Sherwood number on the Rayleigh number, and therefore, the details in the scaling procedure are of minor importance. Figure 8 shows the computed Sherwood number. This number is calculated at the cathode, at the mid-height of the cell which, due to the almost linear variation of the current density, equals the mean Sherwood number. The numerical predicted Sherwood number is found to be related to the Rayleigh number according to  $Sh \approx Ra_h^{0.2}$ . The Rayleigh number, in the above formula, is based on the width of the cell. The reader is referred to Elder [11] for details on the choice of the relevant scales.

Henkes [3] observed that the wall functions, used in the standard  $k-\epsilon$  model formulation, have been established for forced convection. This means that they are not adapted for natural convection and thus he proposed to impose a fixed and large value for  $\epsilon$  at the first mesh points. An imposed value for  $\epsilon$ , corresponds to a non-dimensional distance  $y_{wall}^+ = C_\mu/(0.41\nu k^2\epsilon)$  from the wall to the first mesh point. Henkes showed (see appendix A) that setting a high value of  $\epsilon$  gave good results and that the computed variables were found to be independent of the value, as soon as it is large enough. In other words, the results are not very sensitive to the non-dimensional distance between the first mesh point and the wall. Unfortunately, this is not the case for flows where the flux is given for the walls, for example in electrochemical systems. Figure 9 shows the sensitivity of the flow, to the imposed value  $y_{wall}^+$  at the first mesh points. Fortunately, as

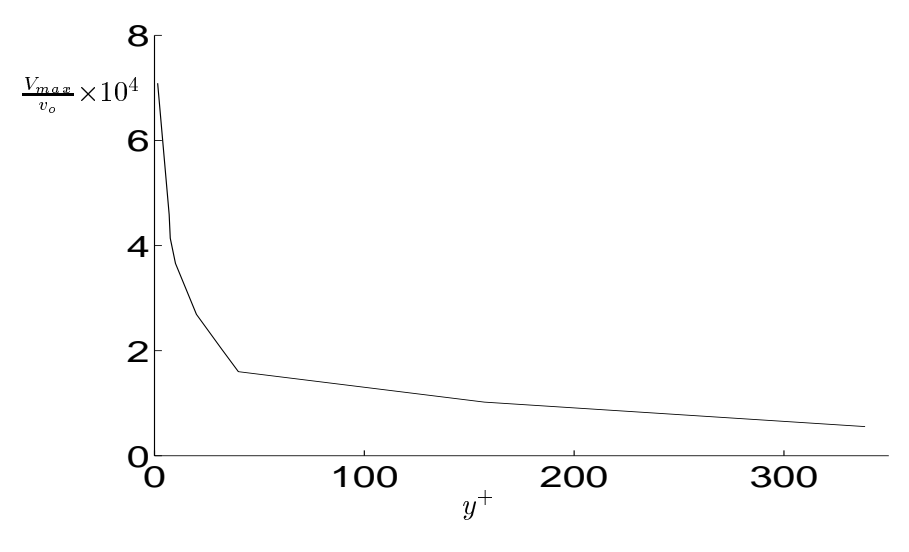


FIGURE 9.  $V_{max}$  versus  $y^{+}$ .  $Ra_{h} = 5 \times 10^{9}$ , Sc = 2763.

shown above, the traditional wall functions predict results in good agreement with the experimental data.

### 5. Conclusions

The study of the turbulent case considered by Ziegler and Evans [4] revealed the presence of large scale turbulent fluctuations, estimated close to the width of the cell, and indicating local sites of weak turbulence near the transitional state. The standard  $k-\epsilon$  model was used for the prediction of a transitional flow induced by natural convection, and good agreement was also obtained with previous direct simulations [13]. Results are shown in Appendix B. The nonlinear kinetics were simulated using a formula derived from a Butler-Volmer law. The predicted Sherwood number was found to be approximately proportional to the Rayleigh number to the power 0.2.

### 6. Appendices: Validation of the code

**6.1.** Appendix A: Turbulent free convection in a closed cavity. Turbulent free convection in a closed cavity has been a test case for turbulence models and numerical methods, see [3]. The flow to be computed takes place in a square cavity and can be assumed to be two-dimensional. The cavity contains air, resulting in a Prandtl number of 0.7. The flow is driven by a temperature difference between vertical walls, while the horizontal walls are assumed to be isolated. The Rayleigh number, based on the temperature difference and the width, or height, of the cavity, is set to  $Ra = 5 \times 10^{10}$ . The turbulence model used here is the standard  $k - \epsilon$  model without any modifications. As recommended by Henkes et al. [3], the value of  $\epsilon$  in the first cell near the vertical wall was set to

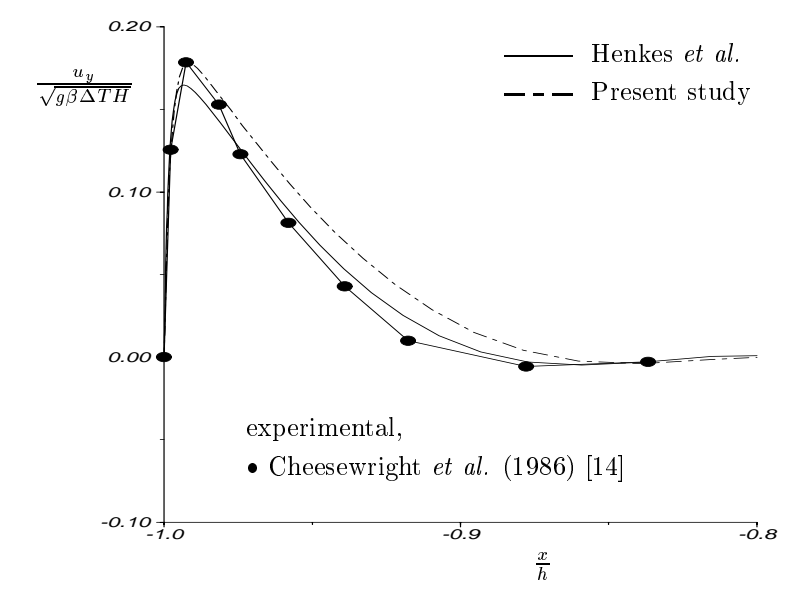


FIGURE 10. The mean non-dimensional vertical velocity profile at the mid-height of the cell.

a large value. The simulation was run using  $90 \times 90$  mesh points, with a higher concentration of grid points near the wall, than in the center of the cavity.

In figures 10 and 11, the non-dimensional vertical velocity and the turbulent kinetic energy, along a horizontal cross-section at the mid-height of the cell, are presented. In those figures, results from the present study are compared with those from numerical simulations reported by Henkes *et al.* and experimental data. The temperature variation, on a vertical cross-section in the midplane of the cell, is presented in figure 12.

Figure 13 shows a comparison between the computed non-dimensional heat flux, the Nusselt number, along the hot wall from the present simulation. It also shows the same prediction by Henkes *et al.* and experimental data. Figure 14 presents a similar comparison, for the non-dimensional shear stress along the hot wall. Fluxes at the wall are quantities, related to gradients of the field variables, and therefore less accuracy can be expected in their prediction. Similar deviations from experimental data have been observed in earlier numerical predictions, see [3].

The boundary conditions for the  $\epsilon$  equation has been discussed in different contributions. The numerical solution found by Henkes et~al. for the Nusselt at the hot wall, as shown in figure 13, reveals a local and abrupt decay of the Nusselt on the lower part of the wall. This decay is identified [3] as the transition point of the boundary layer to the turbulent regime. Such a transition point has not been observed here with the conventional  $k-\epsilon$  model.

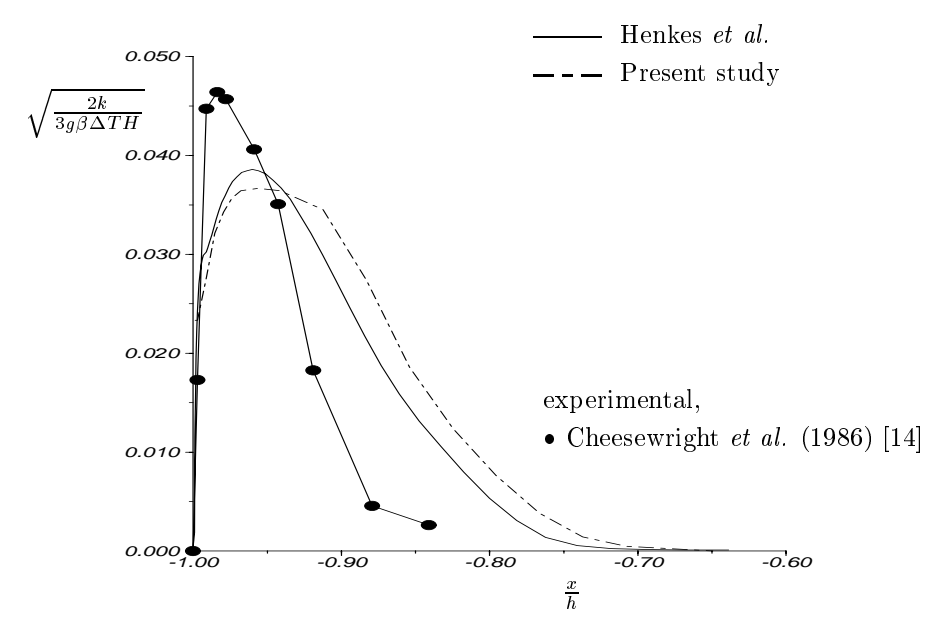


Figure 11. The mean turbulent kinetic energy near the wall, on a cross section at y=0.  $Ra=5\times 10^{10},\ Pr=0.71.$ 

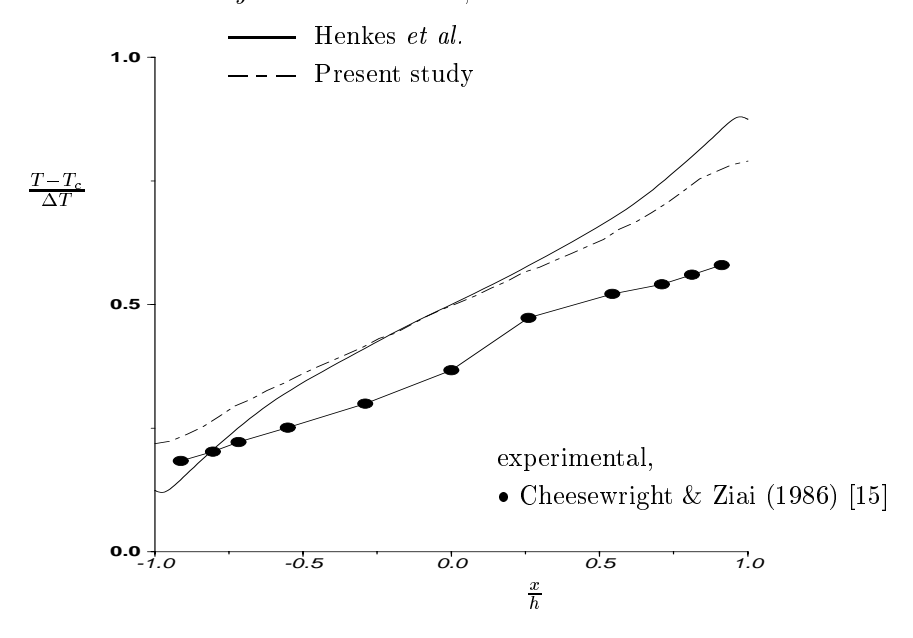


FIGURE 12. The non-dimensional temperature profile in the medium vertical cross-section of the cell.  $Ra = 5 \times 10^{10}$ , Pr = 0.71.

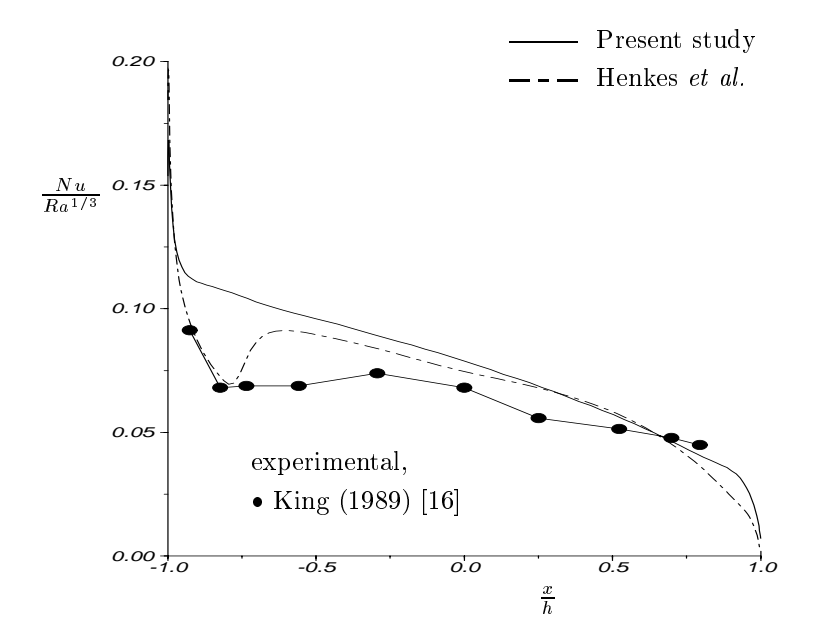


Figure 13. The non-dimensional wall heat transfer along the hot wall.  $Ra=5\times 10^{10},\, Pr=0.71.$ 

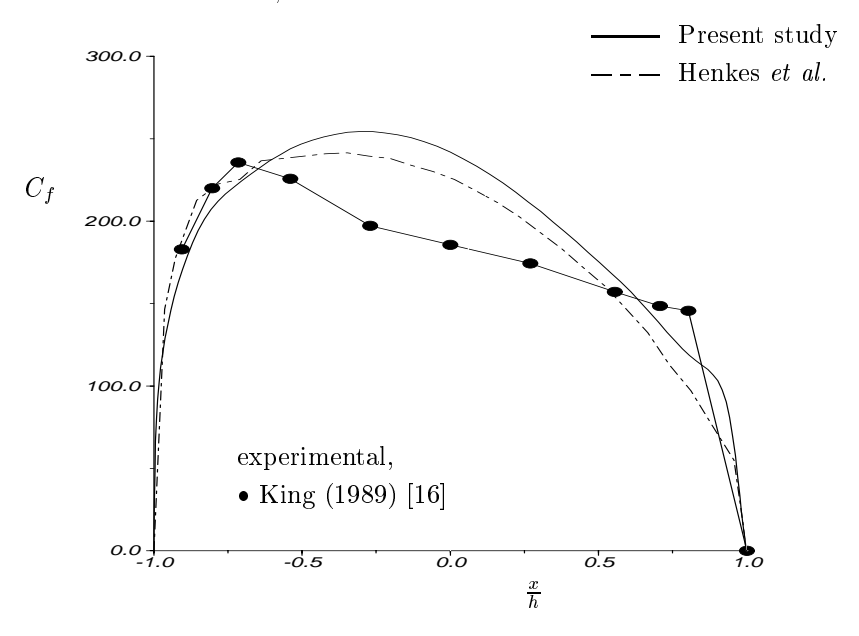


Figure 14. The non-dimensional wall shear stress along the hot wall.  $Ra=5\times 10^{10},\ Pr=0.71.$ 

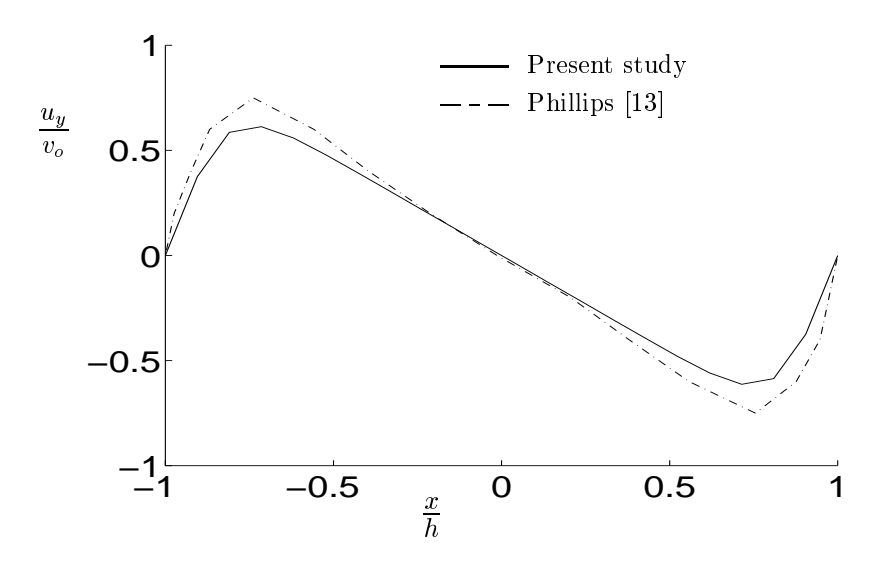


FIGURE 15. The non-dimensional velocity profile in an horizontal cross-section of the cell.  $Gr_h = 8100, Pr = 0.71.$ 

**6.2.** Appendix B: Turbulent unstratified natural convection in a vertical slot for Pr=0.71. The computed flow takes place in an infinite vertical canal, so that it is imposed periodic boundary conditions in the vertical direction. A fixed difference of normalized temperature is set to 1 between the two vertical walls. The Grashof number is set consecutively to 8100 and 22500, see figures 15 and 16. The Prandtl number is 0.71. Calculations performed by the present study were two-dimensional and used the  $k-\epsilon$  model in its standard version. The results are compared with the direct simulations performed by Phillips [13]. As Phillips reported, "at a Prandtl number of 0.7, the critical Grashof number is 8041". Figure 15 is then typically a case of transitional flow. The  $k-\epsilon$  model is nevertheless able to predict the velocity profile qualitatively well. For higher Grashof number, the prediction performed with the  $k-\epsilon$  model is still valid as the turbulent state is approached, see figure 16.

### References

- [1] F.H. Bark and F. Alavyoon, J. Fluid Mech. 290 (1995) 1.
- [2] A. Eklund, F. Alavyoon, D. Simonsson, R.I. Karlsson and F.H. Bark, *Electrochimica Acta* 36 (1991) 1345.
- [3] R.A. Henkes and C.J. Hoogendoorn, Num. Heat Transfer 28 (1995) 59.
- [4] D. Ziegler and J.W. Evans (1986), J. Electrochem. Soc. 133 (1986) 559.
- [5] W.P. Jones and B.E. Launder, Int. J. Heat Mass Transfer 15 (1972) 301.
- [6] H. Ozoe, A. Mouri, M. Ohmuro, S.W. Churchill and N. Lior, Int. J. Heat Mass Transfer 28 (1985) 125.

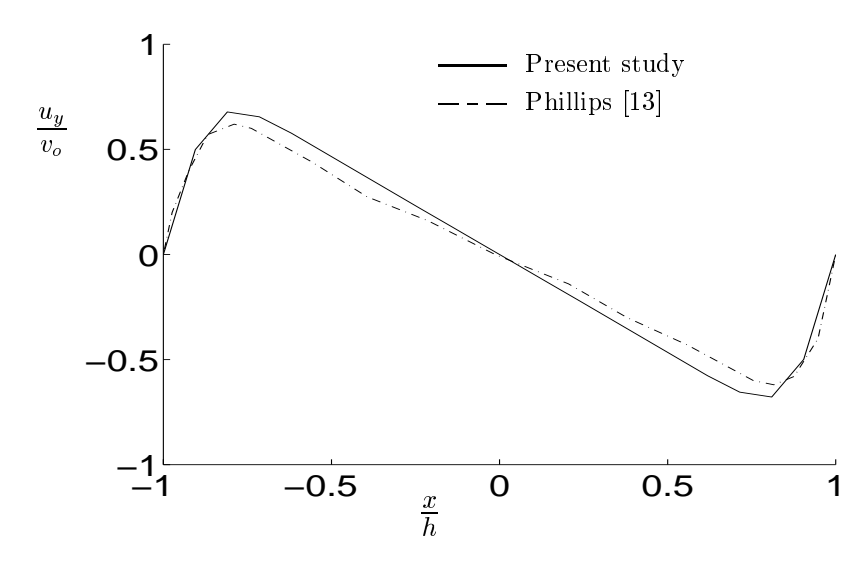


FIGURE 16. The non-dimensional velocity profile in an horizontal cross-section of the cell.  $Gr_h = 22500$ , Pr = 0.71.

- [7] CFX-F3D release 3.3: User Manual, AEA Technology-Computational Fluid Dynamics Services, Building 8.19, Harwell Laboratory, Oxfordshire OX11 0RA, UK, (1994).
- [8] S.V. Patankar and Spalding, Int. J. Heat Mass Transfer 15 (1972) 1787.
- [9] C.M. Rhie and W.L. Chow, American Institute of Aeronautics and Astronautics Journal 21 (1983) 1527.
- [10] P.H. Gaskell and A.K.C Lau, Proc. Conf. on Numerical Methods in Laminar and Turbulent Flow Montreal (1987).
- [11] J.W. Elder, J. Fluid Mech. 23 (1965) 99.
- [12] A. Bejan, Convection Heat Transfer 2nd Ed., Wiley, New York, (1995).
- [13] J.R. Phillips, Int. J. Heat. Mass transfer 39 (1996) 2485.
- [14] R. Cheesewright, K.J. King and S. Ziai, *Proc. ASME Meeting HTD* 60 (1986) 75.
- [15] R. Cheesewright and S. Ziai, *Proc. 8th Int. Heat Transfer Conf.* San Francisco, (1986) 1465.
- [16] K.J. King, Turbulent natural convection in rectangular air cavities, PhD. thesis Queen Mary College, London, U.K (1989).
- [17] V.G. Levich, *Physicochemical Hydrodynamics*, Ed. Prentice-Hall (1962) 293.
- [18] J.S. Newman, Electrochemical systems, Second Ed., University of California, Berkeley, Ed. Prentice Hall, ISBN 0-13-248758-6.
- [19] H. Tennekes and J.L. Lumley, A first course in turbulence, The Massachusetts Institute of Technology Press, ISBN 0 262 20019 8.

[20] F. Walsh, A first course in electrochemical engineering, The Electrochemical Consultancy, Printed in Great Britain by Alresford Press Ltd., ISBN 0 9517307 1 1.

# Paper 2

P2

## LES OF TURBULENT CHANNEL FLOW OF A BINARY ELECTROLYTE

François Gurniki  $^1$ , Koji Fukagata  $^{1\&3}$ , Said Zahrai  $^2$  and F.H. Bark  $^1$ 

- <sup>1</sup> Faxén Laboratory, KTH, Stockholm, S-10044 Sweden
- <sup>2</sup> ABB, Corporate Research, S-72178 Västerås, Sweden

**Abstract.** The turbulent diffusive boundary layer in a binary electrolyte was considered at Schmidt numbers of 1, 10 and 100 and exchange current densities between  $10^{-4}A$   $m^{-2}$  and  $10^{-2}A$   $m^{-2}$ . A numerical scheme was developed for efficient investigation of the dynamics by means of large eddy simulations. The methodology was examined by detailed comparisons with documented data from earlier large eddy and direct numerical simulations and good agreement was found. Application of the methodology to electrochemical mass transfer indicated that the exchange current density seems to have negligible effect on the mean concentration profile but it influences the structure of the fluctuating field in a visible manner.

#### 1. Introduction

Numerical simulations of turbulent flows for industrial use are usually made by considering average fields. In such simulations, influence of turbulent fluctuations on the transport of different quantities must be modelled. Models are usually constructed based on information on the statistical structure of the flow. Making use of experimental data is a usual approach for development and verification of models

Levich [1], based on the analogy with laminar boundary layer, proposed that in a turbulent boundary layer the thickness of the diffusive layer,  $\delta_c$ , would be of the order of magnitude of  $\delta_h \cdot Sc^{-1/3}$ . It has been verified experimentally in different studies, for example by Lin *et al.* [2]. The high value of Schmidt number appearing in most of the practical applications is one of the important factors resulting in thin diffusive boundary layer, and making experimental investigation of flows with mass transfer problematic.

Unfortunately, although electrochemical systems seem to be suitable for experimental investigations, see e.g. [3], the measured data are usually in the form of integrated quantities rather than detailed information on the structure of the flow. As examples, Fouad et al. [4] and Newman [5] studied mass transfer in electrochemical systems and reported global information on the process such as the total cell potential drop, electrical current and global density variation of ionic species. As a result, other tools must be used in order to provide detailed data on the structure of the flow.

<sup>&</sup>lt;sup>3</sup> Department of Quantum Engineering and Systems Science, University of Tokyo, 7-3-1 Hongo, Bunkyo-ku, Tokyo 113, Japan

With improvement of digital computers and computational methods during the past years, simulations could be used as an alternative to physical experiments. Study of turbulent channel flow, for example, has played an important role in modelling turbulence, in particular in the vicinity of a rigid wall. A pure numerical solution of the mathematical equations without a model is usually referred to as direct numerical simulation. Clearly, the advantage is that no models are involved at the cost of being limited to low Reynolds numbers. An alternative route is to use large eddy simulations, where only small eddies which have a more universal behaviour are modelled. Using large eddy simulations, higher Reynolds number can be studied.

In the earlier studies, boundary conditions for the passive scalar were such that direct use of presented data for modelling of mass transfer at the electrode in an electrochemical system were not possible. The goal of the present study is to provide detailed information about the statistical structure of a turbulent boundary layer with mass transfer using boundary conditions of interest for electrochemical systems. Statistical data presenting the structure of the boundary layer are to be obtained by performing large eddy simulations. The hydrodynamic part of the computation performed by Zahrai et al. [6] is completed in the present study to treat the mass conservation equation.

## 2. Formulation of the problem

In this study turbulent flow of a binary electrolyte outside the double layers in an infinitely large cell is considered. The electrodes are assumed to be at a distance of  $2\delta$  and the flow is driven by a constant pressure gradient, strong enough to make gravitational effects negligible. The coordinate system is chosen so that the electrodes are located at  $y=\pm\delta$ . The electrical neutrality of the electrolyte can be expressed as  $z_1c_1+z_2c_2=0$ , where  $c_i$  and  $z_i$  denote the concentration and the charge number of species i, respectively. The transport equations for the mass in a binary electrolyte can be reduced to one single diffusion-convection equation for a concentration field defined by  $c=z_1c_1=-z_2c_2$ . It can easily be shown that the charge neutrality will then be identically satisfied.

Under the above conditions, the flow can be described by the Navier-Stokes equations for an incompressible fluid, the law of conservation of mass for a fluid at constant density and a transport equation for the reduced concentration field. Using  $u_{\tau}$ , the friction velocity, as the characteristic velocity scale,  $l^* = \nu/u_{\tau}$ , the typical length scale in wall units, the continuity and Navier-Stokes equations can be written for the instantaneous velocity vector as

$$\nabla^+ \cdot \mathbf{u}^+ = 0 \tag{1}$$

and

$$\frac{\partial \mathbf{u}^{+}}{\partial t^{+}} + (\mathbf{u}^{+} \cdot \nabla^{+}) \mathbf{u}^{+} = -\nabla^{+} p^{+} + \Delta^{+} \mathbf{u}^{+}, \tag{2}$$

where **u** denotes the instantaneous velocity field and p is the instantaneous pressure field and is nondimensionalized by  $\rho u_{\tau}^2$ . The transport equation for the reduced instantaneous concentration field, using the above scales, can be written as

$$\frac{\partial c^{+}}{\partial t^{+}} + \left(\mathbf{u}^{+} \cdot \nabla^{+}\right) c^{+} = \frac{1}{Sc} \Delta^{+} c^{+}, \tag{3}$$

where Sc is the Schmidt number. The concentration field can be made dimensionless by using the mass flux at the wall, i.e.  $C^* = -\frac{D}{u_\tau} \left(\frac{\partial \overline{c}}{\partial y}\right)_{wall}$ , where  $\overline{c}$  corresponds to the averaged value of the instantaneous concentration. All quantities are thus scaled in wall units; therefore the superscript '+' will be dropped throughout the remainder of this paper. Nevertheless, for more clarity, the superscript can be maintained in the captions of the figures. For the hydrodynamic equations, the no-slip condition is used at the electrodes. Note that the non-dimensional half-channel width will be equal to  $Re_\tau$  in the wall units. For the concentration field different boundary conditions are considered. As a first step, in order to make comparisons with earlier numerical and experimental investigations, the case of mass transfer when the concentration is set to a given value at the wall is considered, i.e.

$$c(x, \pm Re_{\tau}, z, t) = \pm c_{wall}. \tag{4}$$

For electrochemical systems, other boundary conditions are also of interest. Here, two simplified conditions are used for modelling the mass flux from the electrodes:

$$\frac{\partial c}{\partial y}(x, \pm Re_{\tau}, z, t) = \pm J_{wall},\tag{5}$$

i.e. the flux is given at the electrodes, and finally a boundary condition which allows fluctuations of the flux with the value of the concentration at the electrodes,

$$\frac{\partial c}{\partial y}(x, \pm Re_{\tau}, z, t) = \pm K_o \left[ c(x, \pm Re_{\tau}, z, t) - C_o \right]. \tag{6}$$

In the above relations,  $C_o$ ,  $K_o$  and  $J_{wall}$  are given constants. The form of the boundary condition in (6) comes directly from the first term in a Taylor expansion of the Butler-Volmer mass transfer law, see e.g. [7].  $K_o$  is proportional to the exchange current density of the chemical reaction at the wall and is equal to

$$K_o = \frac{i_o}{2FD_1C_oRe_{\tau}},\tag{7}$$

where  $i_o$  is the exchange current density, F is the Faraday constant,  $D_1$  is the salt diffusivity constant for the metallic ionic species of the binary electrolyte, and  $C_o$  a reference value for the reduced concentration at equilibrium, which is the same as in the core of the channel. If an electrolyte with low electrical potential gradients is considered, the boundary condition (6) is a good approximation of the electrochemical mass transfer law at the electrodes. Experimentally, such

a configuration can be obtained with an additional ion that does not take part of the chemical reactions and reduces the electrical resistance of the electrolyte considerably [5]. Equation (6) can also be written as

$$\frac{\partial c}{\partial u}(x, \pm Re_{\tau}, z, t) = \pm \left[K_o \cdot c(x, \pm Re_{\tau}, z, t) - J_o\right],\tag{8}$$

where  $J_o = \frac{i_o}{2FD_1Re_{\tau}}$ . In this form, it is clear that for low values of  $K_o$ , this boundary condition approaches equation (5). It is worth noting that the exposed boundary conditions above are linear and remain the same when considering the time-averaged values.

#### 3. Numerical procedure

The methodology used for the fluid velocity field is taken from the earlier work on the simulation of turbulent channel flows by Zahrai et~al.~[6]. In this large eddy simulation, averaging over the volume of the computational cells is used as the filtering function. The subgrid model is an anisotropic version of the Smagorinsky eddy viscosity model. A rectangular computational cell, numbered M, has the width in the i-direction,  $\Delta x_i^M$ , the area of surface normal to i-direction,  $\Delta s_i^M = \Delta x_j^M \Delta x_k^M$ , and a volume size,  $\Delta v^M = \Delta x_1^M \Delta x_2^M \Delta x_3^M$ . The modelled Navier-Stokes equation (2) averaged over the volume using the cell M, which gives the dynamics of large eddies resolved on the given mesh, can be expressed as

$$\Delta v^M \frac{\partial \overline{u}_i^M}{\partial t} = \\ \sum_{j=1}^3 \Delta s_j^M \left[ -\left( u_i^{(+j)M} u_j^{(+j)M} - u_i^{(-j)M} u_j^{(-j)M} \right) - \left( p^{(+j)M} - p^{(-j)M} \right) \delta_{ij} \right] \\ + \sum_{j=1}^3 \Delta s_j^M \left[ \left( \tau_{ij}^{(+j)M} - \tau_{ij}^{(-j)M} \right) \right] \\ + \sum_{j=1}^3 \Delta s_j^M \left[ \frac{1}{\sqrt{2}} C^2 L_j^2 \left( \left| \overline{s}_{ij}^M \right|^{(+j)M} \cdot s_{ij}^{(+j)M} - \left| \overline{s}_{ij}^M \right|^{(-j)M} \cdot s_{ij}^{(-j)M} \right) \right] , \\ \text{where } \tau_{ij} \text{ is the resolved stress tensor, and } s_{ij} \text{ the deformation tensor, } \left| \overline{s}_{ij}^M \right| = \\ \left( \sqrt{\sum_{i=1}^3 \sum_{j=1}^3 \overline{s}_{ij}^M^2} \right), \text{ and } L_j^2 = (\Delta x_1^M \Delta x_2^M \Delta x_3^M)^{2/9} (\Delta x_j^M)^{4/3}. \text{ Considering an instantaneous function } f(\mathbf{x}), \overline{f}^M \text{ stands for the filtered version of } f \text{ at the center of cell M, whose volume is } \Delta v^M. \text{ The superscript } (\pm j)M \text{ denotes that the considered filtered quantity is evaluated on the cell surface whose center is }$$

the vector  $\mathbf{x}^M \pm \frac{1}{2} \Delta x_j^M \mathbf{e}_j$  and whose normal direction is  $\mathbf{e}_j$ . It is worth mentioning that the above equation is not differenced but only filtered by integrating the Navier-Stokes equations on a cell volume. The transport through the cell surfaces due to fluctuations of smaller sizes than the size of the cell are modelled by a Smagorinsky-like subgrid viscosity. The modified Smagorinsky model has the property of vanishing in the regions where the resolution is good enough in an anisotropic manner. As a result, in the wall-region where the mesh size is chosen so that the details of the flow can be studied, the

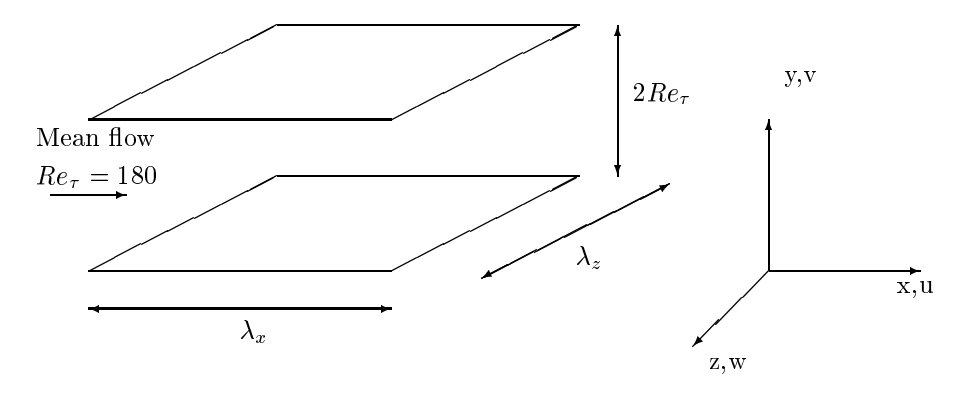


FIGURE 1. The geometry of the cell and the chosen coordinate system.

Table 1. Mesh specification.

	$N_x$	$N_y$	$N_z$	$\Delta x$	$\Delta z$	$\Delta y_{min}$	$\Delta y_{max}$
$\operatorname{Mesh} 1 \times 1 \times 1$	32	42	96	70.6858	11.781	1.4062	18.92
$Mesh 1 \times 2 \times 1$	32	84	96	70.6858	11.781	0.7031	9.46
$\operatorname{Mesh} 1 \times 6 \times 1$	32	252	96	70.6858	11.781	0.2344	3.16

influence of the model becomes weak without explicit damping. The fine resolution of the flow near the wall eliminates the need of wall functions. The model constant C was set to 0.08, as suggested in [6]. The flow is driven by a body force, or by a pressure gradient constant in space and time. In other words, the pressure term is decomposed into a mean pressure gradient, i.e. a given constant equal to 1 in wall units, and a fluctuating part which is to be solved together with the velocity field.

Similarly, the mass transport equation can be filtered at each cell M, which can differ from ones used for the velocity field. The turbulent Schmidt number,  $Sc_t$ , was set to 0.25, which may be a reasonable value, since the turbulent Prandtl number  $Pr_t$ , in the cases of large eddy simulation with heat transfer, is usually proposed to be between 1/2 and 1/3, see e.g. [8].

The computational domain is periodic in the streamwise and the spanwise directions with corresponding periodicity lengths,  $\lambda_x$  and  $\lambda_z$ . The distance between the channel walls is  $2Re_{\tau}$ .  $\lambda_x$  and  $\lambda_z$  are respectively  $4\times\pi\times Re_{\tau}$  and  $2\times\pi\times Re_{\tau}$ , see figure 1. Periodic boundary conditions are applied for the pressure fluctuations, the instantaneous velocity, and concentration in the streamwise and spanwise direction.

As a unique feature of this study, the use of different mesh systems for the fluid velocity field and the concentration field should be pointed out. Table 1 shows the characteristics of three meshes. The one denoted as Mesh  $1\times1\times1$  is used for the fluid velocity field. The meshes used for the concentration field

are Mesh  $1 \times 2 \times 1$ , and Mesh  $1 \times 6 \times 1$ . The finest mesh, Mesh  $1 \times 6 \times 1$ , was used for the the calculations performed at Sc=100 only. The grids are uniform in the mean flow direction. They are stretched in the direction normal to the wall, with the finest spacing at the walls. According to Calmet *et al.* [9], at least three mesh points in the wall-normal direction are required within the diffusive sublayer,  $y < \frac{5}{Sc^{1/3}}$ , to resolve the unlinear behavior near the wall. The mesh systems used in the study fulfill this requirement.

The initial profile in a cross section for the velocity was set parabolic. The mass transfer calculation was not added until the hydrodynamic simulation had reached statistically equilibrium state. The initial profile in a cross section for the reduced concentration was linear for the first calculation, at Sc=1 and with a fixed value as the boundary condition at the walls. The calculations with other boundary conditions or higher Sc were initialized with the calculated concentration field obtained with the highest available Schmidt number. The calculated variables were considered to be at equilibrium when variation of the statistical properties in time were small.

#### 4. Results

The flow is assumed to take place at Reynolds number of 180 based on the wall friction velocity and the channel half width. The conditions of computation of the velocity field are exactly the same as those reported in [6]. The present study focuses on the mean concentration field, RMS intensities, the eddy diffusivity, and the structure of the instantaneous concentration field. Transport equations are solved for the concentration field at Schmidt number 1,10 and 100.

In figure 2, the mean concentration profile in the direction normal to the walls is presented for flow at Schmidt number equal to one. Good agreement is found with results from direct numerical simulations by Lyons et al. [10] and Papavassiliou et al. [11]. The methodology and subgrid-scale model used in the present study are consequently found to be accurate enough to model the turbulence mass transport on small scales. Figure 3 indicates similar variation of the mean concentration profile in the logarithmic diagram. With increasing  $y^+$ , the concentration profile exhibits a buffer layer character, followed by a logarithmic region. As shown on figure 3, the concentration profile in the outer region fits well with the logarithmic law of  $\overline{c}^+ = 3.6 \cdot ln(y^+) + 1.7$  after  $y^+ = 30$ . The constants of the logarithmic law found in the present study agree well with the mean profiles predicted by Lyons et al. [10] and Papavassiliou et al. [11].

Figures 2 and 3 present also the average concentration calculated with the Butler-Volmer-like boundary condition (6) and the three different values of  $K_o$ . No influence of  $K_o$ , or the exchange current density, can be observed on the mean concentration profiles.

The RMS levels for the concentration field are calculated at Schmidt numbers and  $K_o$  mentioned above, and presented in figure 4. Very good agreement is

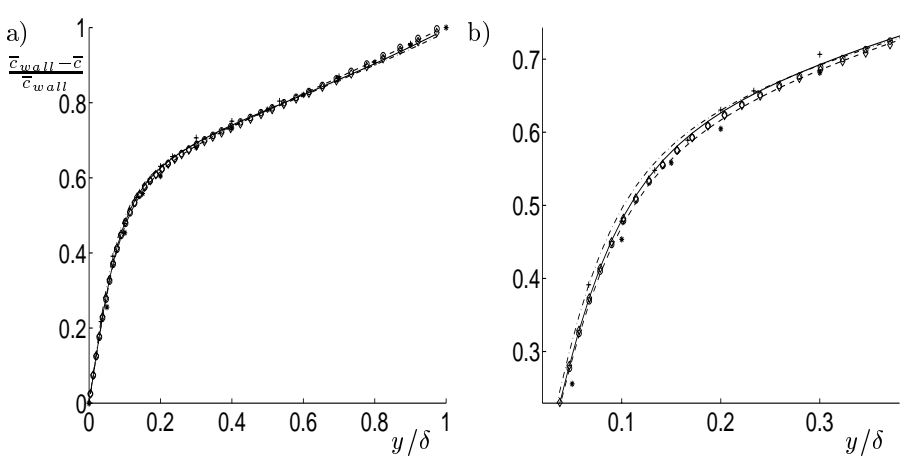


Figure 2. a) The mean concentration at Sc=1 in the normal direction to the walls. \_ . \_ : Present study, LES,  $Re_{\tau}=180$ ,  $c_{wall}=\pm 1/C^*$ . \_ \_ : Present study,  $\left(\frac{\partial c}{\partial y}\right)_{wall}=\pm J_{wall}$ . Diamonds : Present study,  $K_o=1/Re_{\tau}$ . \_ : Present study,  $K_o=10/Re_{\tau}$ .  $\circ \circ \circ$ : Present study,  $K_o=100/Re_{\tau}$ . \* \* \* \*: Lyons [10], DNS,  $Re_{\tau}=150$ . + + + +: Papavassiliou [11], DNS,  $Re_{\tau}=150$ . b) Same as in a) zoomed on the near-wall region.

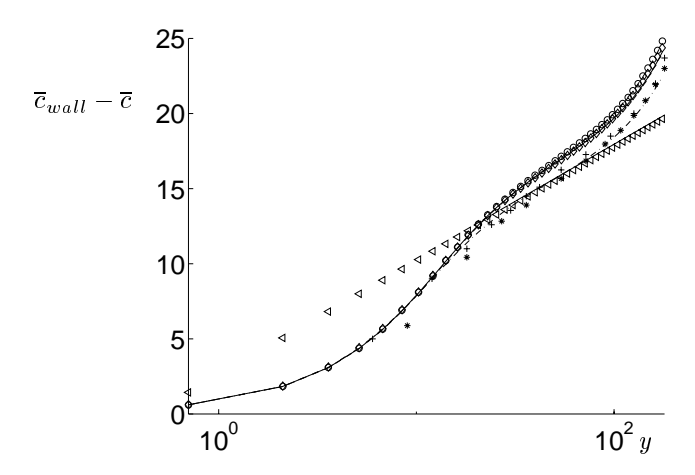
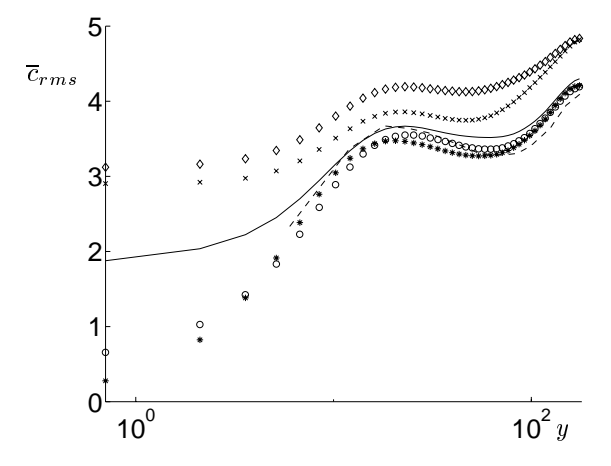


FIGURE 3. The mean concentration at Sc=1 in the normal direction to the walls and in the near-wall region. \_ . \_: Present study,  $c_{wall}=\pm 1/C^*$ . \_ \_: Present study,  $\left(\frac{\partial c}{\partial y}\right)_{wall}=\pm J_{wall}$ . Diamonds: Present study,  $K_o=1/Re_{\tau}$ . \_ : Present study,  $K_o=10/Re_{\tau}$ .  $\circ \circ \circ$ : Present study,  $K_o=100/Re_{\tau}$ .  $\lhd \circ \lhd : \overline{c}^+=3.6 \cdot ln(y^+)+1.7$ . \* \* \* \* Lyons [10], DNS,  $Re_{\tau}=150$ . + + + +: Papavassiliou [11], DNS,  $Re_{\tau}=150$ .



obtained with the results presented by Lyons et al. [10], performed with a fixed value of concentration set at the walls. Moreover, RMS levels computed with the boundary condition (6) and  $K_o = 10/Re_{\tau}$ , have intermediary values between the two results obtained with  $K_o = 1/Re_{\tau}$  ( $i_o = 10^{-4}A~m^{-2}$ ) and  $K_o = 100/Re_{\tau}$  ( $i_o = 10^{-2}A~m^{-2}$ ). Therefore, at Schmidt number equal to one, RMS levels close to the wall are likely to be a monotone function of  $K_o$ , or  $i_o$ , and seem to decrease when the exchange current density increases.

An issue of interest could be the assymptotic behavior of the Butler-Volmerlike, equation (6), with respect to variations of  $K_o$ , defined in (7). At high values of  $K_o$ , or at high exchange current densities, the right hand side of (6) becomes dominant. The system becomes sensitive to small variations of the concentration at the wall and tends to balance them fast. In the limiting case where  $K_o$  approaches infinity, equation (6) becomes equivalent to equation (4), i.e. the system acts as one with a fixed value set for concentration at the wall. At low values of  $K_o$ , the fluctuations of the concentration gradient at the wall are damped and the behaviour of equation (6) becomes similar to a constant flux at the wall. As a result, the diffusive boundary layer simulated with the Butler-Volmer-like boundary condition (6) at a low exchange current density, is expected to have similar behavior as that with a constant flux for the boundary condition, and at a high exchange current density, similar to the case with a fixed value at the walls. A comparison between profiles found with different values of  $K_0$  in figure 4, confirms the proposed behavior. Figures 5 and 6 show RMS intensities calculated with equation (4) and (5), at Schmidt number equal to 10 and 100,

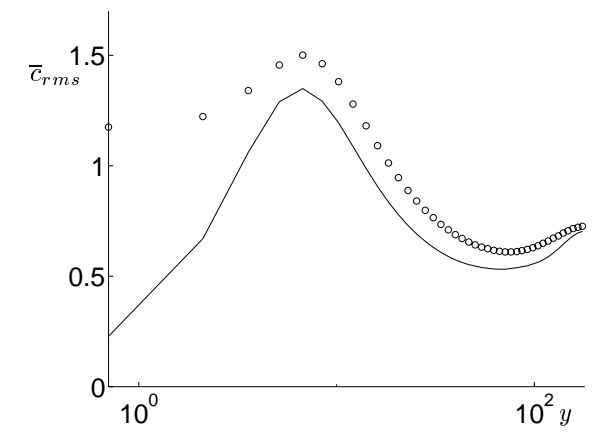


FIGURE 5. RMS levels of the concentration field at Sc=10 in the normal direction of the walls.  $\_$ : Present study,  $c_{wall}=\pm 1/C^*$ .  $\circ \circ$   $\circ$ : Present study,  $\left(\frac{\partial c}{\partial y}\right)_{wall}=\pm J_{wall}$ .

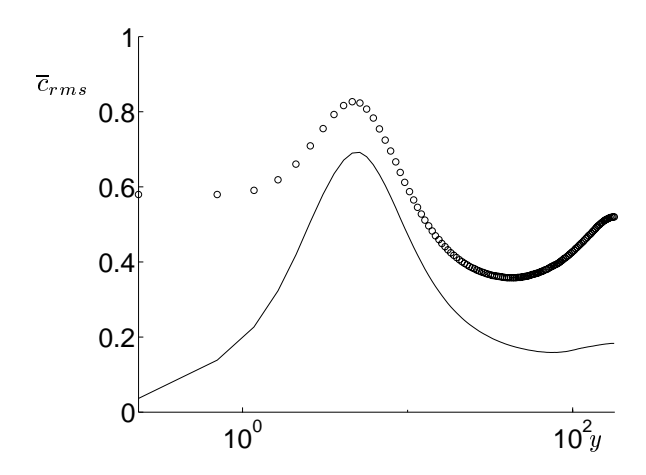


FIGURE 6. RMS levels of the concentration field at Sc=100 in the normal direction of the walls.  $\_$ : Present study,  $c_{wall}=\pm 1/C^*$ .  $\circ \circ$   $\circ$ : Present study,  $\left(\frac{\partial c}{\partial y}\right)_{wall}=\pm J_{wall}$ .

respectively. As expected, values predicted with a fixed value set at the walls, are lower than RMS intensities predicted with a constant flux. Similar behavior was predicted at Schmidt number equal to one. Since the above discussion does not account for values of Schmidt number, it is possible, at any Schmidt number, to draw conclusions about the effect of very low and very high exchange current densities on RMS intensities, on the basis of calculations made only with a fixed value and a constant flux set at the walls. The mean eddy diffusivity, defined as

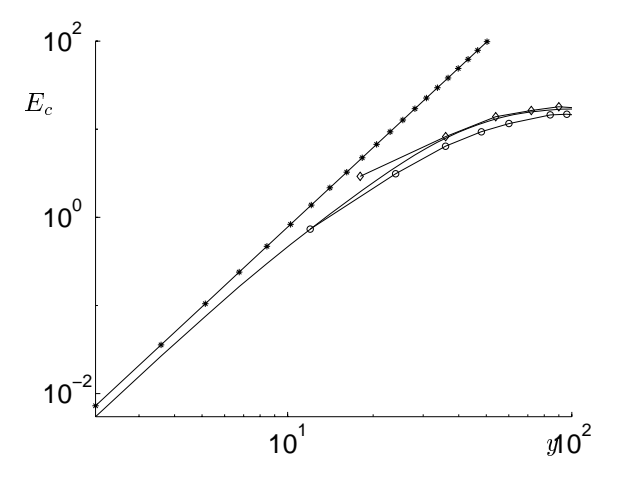


FIGURE 7. The mean eddy diffusivity in the near-wall region at Sc=1. -\*-\*-:  $E_c=0.000775y^3$  [11].  $\_$ : Present study,  $c_{wall}=\pm 1/C^*$ .  $\circ \circ \circ$ : Papavassiliou [11]. Diamonds: Lyons [10].

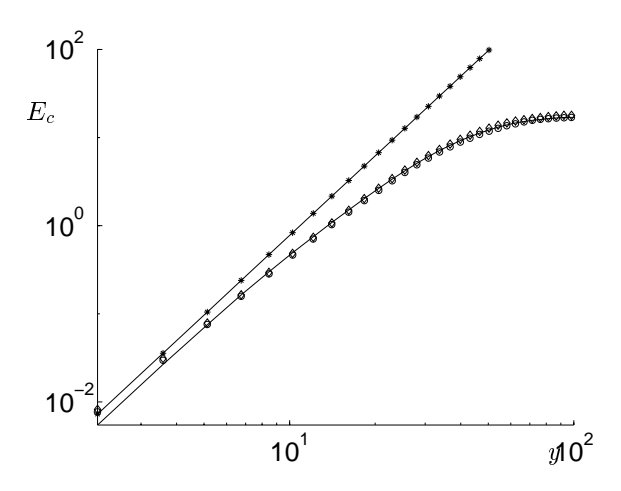


Figure 8. The mean eddy diffusivity in the near-wall region at Sc=1. -\*-\*-:  $E_c=0.000775y^3$  [11]. \_:  $c_{wall}=\pm 1/C^*$ .  $\circ \circ \circ : \left(\frac{\partial c}{\partial y}\right)_{wall}=\pm J_{wall}$ . Diamonds:  $\left(\frac{\partial c}{\partial y}\right)_{wall}=\pm \left(\frac{c_{wall}}{Re_{\tau}}-J_o\right)$ .

 $E_c = -\frac{\overline{vc}}{\left(\frac{d\overline{v}}{dy}\right)}$ , is presented for different cases in figures 7, 8 and 9. Figure 7 shows good agreement between the prediction of the present study, the prediction of Papavassiliou et al. [11], and the empirical profile proposed by Papavassiliou et al. [11]. Figures 8 and 9 indicate that the eddy diffusivity is not influenced by the values of  $K_o$ , or the exchange current density  $i_o$ . The fact that the eddy-diffusivity is found to be independent of  $K_o$  can be related to the same observation for the mean concentration profile, see figures 2 and 3.

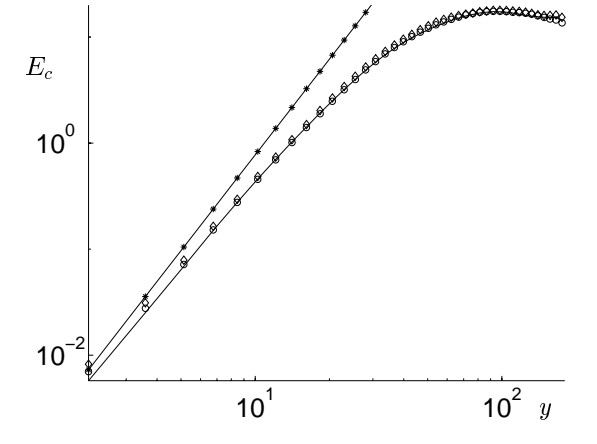


FIGURE 9. The mean eddy diffusivity in the near-wall region at Sc=1.  $\_$ :  $K_o=100/Re_{\tau}$ .  $\circ \circ \circ$ :  $K_o=10/Re_{\tau}$ . Diamonds:  $K_o=1/Re_{\tau}$ .

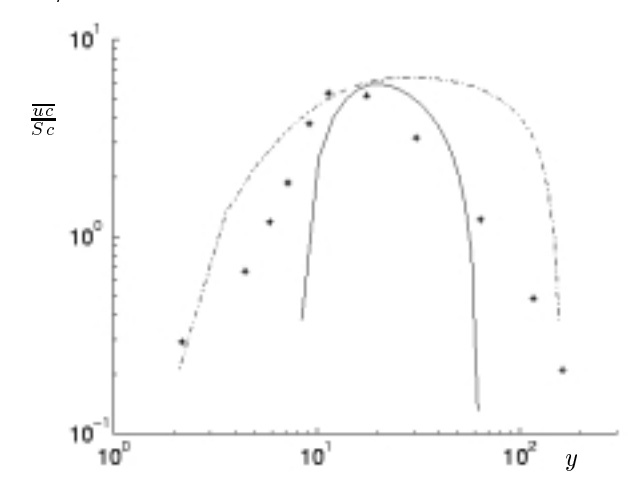


FIGURE 10. At Sc=1, the streamwise turbulent heat flux. Results computed with the Butler-Volmer-like boundary condition. Solid line,  $K_o=10/Re_{\tau}$ . Dashed lines,  $K_o=100/Re_{\tau}$ . The stars account for the numerical results of Kawamura et~al.~[12], with  $Re_{\tau}=180$  and Sc=1.5.

Streamwise and wall-normal turbulent passive mass flux are presented in figures 10 and 11.

Good agreement is found with the direct numerical simulation of Kawamura et al. [12]. No data from previous results were available for comparison with the predictions of the present study at Schmidt number higher than 5. The present study finds, as the last mentioned study, that the scalar fluctuations correlate

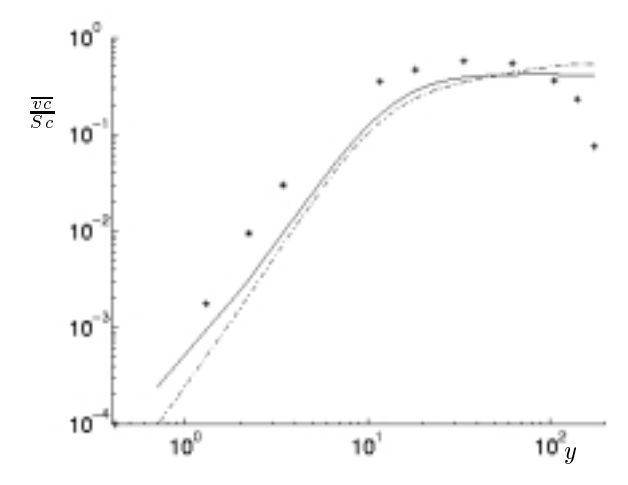


FIGURE 11. At Sc=1, the wall-normal turbulent heat flux. Results computed with the Butler-Volmer-like boundary condition. Solid line,  $K_o=10/Re_{\tau}$ . Dashed lines,  $K_o=100/Re_{\tau}$ . The stars account for the numerical results of Kawamura *et al.* [12], with  $Re_{\tau}=180$  and Sc=1.5.

more strongly with the streamwise velocity than with its normal-wall component. Figure 10 shows that the exchange current seems to influence the range of strong correlation between the streamwise velocity and the scalar fluctuations. Inversely, no influence of the exchange current is noticed on the correlation between the wall-normal velocity and the scalar fluctuations, see figure 11.

Iso-lines of the instantaneous concentration fluctuations for Schmidt number equal to one in a (x-z) section at  $y^+ = 6.76$  are presented in figure 12. The presence of well-known streaky structures elongated in the streamwise direction is clearly observed. Such structures are typical for turbulent flows in the viscous sublayer [13].

To compute the results in figure 12, the Butler-Volmer-like law has been used. The influence of the exchange current on the streaks is studied, by comparing 12.a, which presents a field computed with  $K_o = 10/Re_{\tau}$ , and 12.b which corresponds to  $K_o = 100/Re_{\tau}$ . Even if it is not possible here to give a clear quantitative approximation of the spacing, it seems that the spanwise spacing decreases with the increasing exchange current. This result is confirmed by the computation of the two-point spanwise correlation coefficients of the concentration fluctuations, see figure 13. Considering the normal distance from the wall to the first local minimum of the spanwise correlation coefficient as the mean streak half-spacing, Calmet et al. found  $r_z^+ = 100$ . With the same method, the present study found at Schmidt number equal to one,  $r_z^+$  around 65 with an intermediary exchange current, and around 55 with a high exchange current,

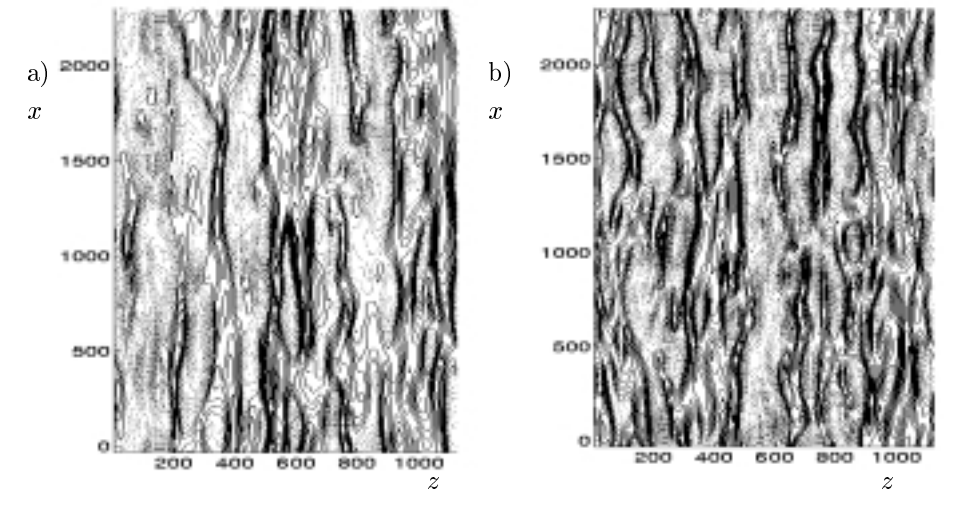


FIGURE 12. At Sc=1, snapshot contour plots of the concentration fluctuations in a (x-z) plane at  $y^+=6.76$ . Results computed with the Butler-Volmer-like boundary condition. The increment in scalar is 0.02. Solid lines represent  $0.0 \le c^{'} \le c^{'}_{max}$ . Dashed lines  $c^{'}_{min} \le c^{'} \le 0.0$ . a)  $K_o=10/Re_{\tau}$ .  $c^{'}_{min}=-0.323$ ,  $c^{'}_{max}=+0.21$ . b)  $K_o=100/Re_{\tau}$ .  $c^{'}_{min}=-0.457$ ,  $c^{'}_{max}=+0.186$ .

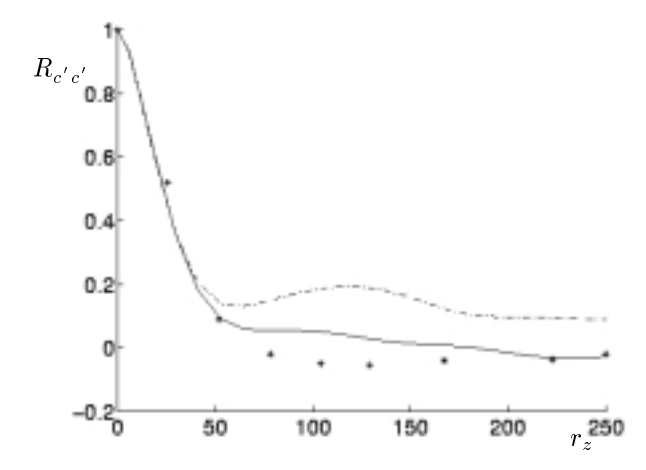


FIGURE 13. At Sc=1, spanwise two-point correlation coefficients at  $y^+=6.76$ . Results computed with the Butler-Volmer-like boundary condition. Solid line,  $K_o=10/Re_{\tau}$ . Dashed lines,  $K_o=100/Re_{\tau}$ . The stars account for the numerical results of Calmet *et al.* [9] at  $y^+=1.7$ ,  $Re_{\tau}=640$ , and a Dirichlet boundary condition at the walls.

see figure 13. These two last results are in good agreement with the computed spacing found by Kline et al. [13].

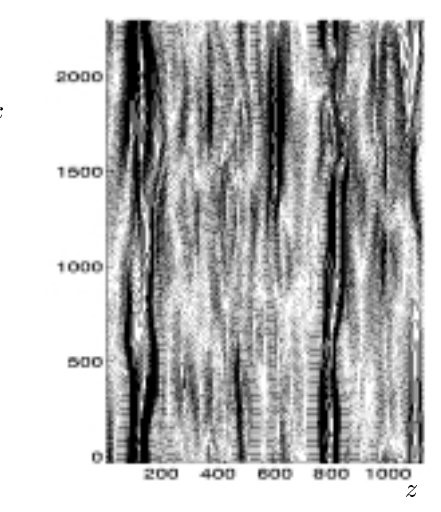


FIGURE 14. At Sc=100, snapshot contour plots of the concentration fluctuations in a (x-z) plane at  $y^+=1.17$ . Results computed with a constant flux for concentration at the walls. The increment in scalar is 0.02. Solid lines represent  $0.0 \le c^{'} \le c^{'}_{max}$ . Dashed lines  $c^{'}_{min} \le c^{'} \le 0.0$ .  $c^{'}_{min} = -0.687$ ,  $c^{'}_{max} = 0.379$ .

At Schmidt number equal to 100, the concentration fluctuations are plotted in the viscous sublayer in a section (x-z) at  $y^+ = 6.76/Sc^{1/3} = 1.17$ , see figure 14. Again, the streaky structure of fluctuations are clearly observed.

Figure 15 presents the instantaneous concentration fluctuations in the logarithmic region at  $y^+ = 54.1$ . The streaky structures are not visible any more. Here,  $K_o$  is taken equal to 10 and 100 only. At these values, the exchange current density has not influenced the wall-normal location of the streaky structures. This was expected, since the streaky structures are traditionally observed in the diffusive sublayer [9]. But supplementary computations with different values of exchange current would allow to confirm this result, and extend it to a bigger range of exchange currents.

## 5. Conclusions

A model problem for studying the mechanisms of turbulent mass transfer in an electrochemical system by means of large eddy simulations is proposed. Firstly, it was shown that the methodology was able to successfully reproduce documented literature results. Both mean profiles and fluctuations were predicted accurately. The influence of the exchange current density on the turbulent diffusive boundary layer was investigated at Schmidt numbers of 1, 10 and 100. The studied range of the exchange current density was between  $i_o = 10^{-4} A \ m^{-2}$  and  $i_o = 10^{-2} A \ m^{-2}$ . Three different boundary conditions for the concentration field were used at the walls, i.e. a linearized Butler-Volmer-like condition, a given value and a given flux. At Schmidt number equal to one, the exchange current was shown

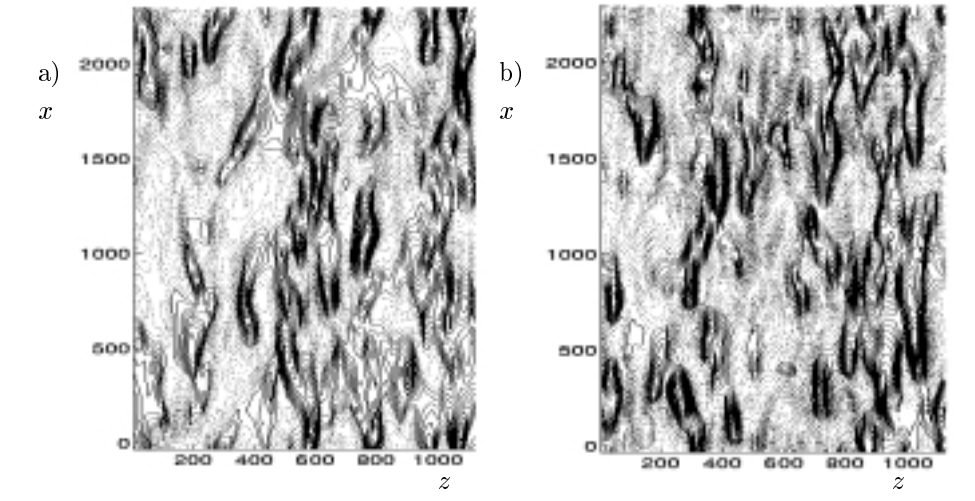


FIGURE 15. At Sc=1, snapshot contour plots of the concentration fluctuations in a (x-z) plane at  $y^+=54.1$ . Results computed with the Butler-Volmer-like boundary condition. The increment in scalar is 0.02. Solid lines represent  $0.0 \le c^{'} \le c^{'}_{max}$ . Dashed lines  $c^{'}_{min} \le c^{'} \le 0.0$ . a)  $K_o=10/Re_{\tau}$ .  $c^{'}_{min}=-0.43$ ,  $c^{'}_{max}=+0.262$ . b)  $K_o=100/Re_{\tau}$ .  $c^{'}_{min}=-0.575$ ,  $c^{'}_{max}=+0.325$ .

to have no influence on the structure of the mean concentration, neither on the eddy diffusivity, nor on the wall-normal turbulent heat flux. However, the RMS intensities, the streamwise turbulent heat flux, and the lateral dimensions of turbulence structures in the near-wall region were influenced. The Butler-Volmer-like boundary condition predicts results close to those obtained with a given value at the wall if the exchange current density is high, and close to those obtained with a given flux if the exchange current density is low.

### References

- [1] V.G. Levich, *Physicochemical hydrodynamics* Ed. Prentice-Hall (1962) 293.
- [2] C.S. Lin, R.W. Moulton and G.L. Putnam, *Industrial and Engineering Chemistry* 45 (1952) 636.
- [3] R.J Goldstein, H.D. Chiang and D.L. Lee, J. Fluid Mech. 213 (1990) 111.
- [4] M.G. Fouad and N. Ibl, Electrochimica Acta 3 (1960) 233.
- [5] J.S. Newman, *Electrochemical systems*, second Ed., University of California, Berkeley, Ed. Prentice Hall, ISBN 0-13-248758-6.
- [6] S. Zahrai, F.H. Bark, R.I. Karlsson, Eur. J. Mech., B/Fluids 14 (1995) 459.
- [7] F.H. Bark and F. Alavyoon, J. Fluid Mech. 290 (1995) 1.
- [8] Y. Miyake, Computational Fluid Dynamics, Ed. M.Yasuhara & H. Daiguji, Chap. 10, p.223, (1992) Univ. Tokyo Press.
- [9] I. Calmet and J. Magnaudet, Phys. Fluids 9 (1997) 438.

- [10] S.L. Lyons, T.J. Hanratty and J.B. McLaughlin, Int. J. Num. Methods in Fluids 13 (1991) 999.
- [11] D.V. Papavassiliou and J. Thomas Hanratty, Int. J. Heat Mass Transfer 40 (1997) 1303.
- [12] H. Kawamura, K. Ohsaka, H. Abe and K. Yamamoto, Int. J. Heat and Fluid Flow 19 (1998) 482.
- [13] S.J. Kline, W.C. Reynolds, F.A. Schraub and P.W. Runstadler, J. Fluid Mech. 30 (1967) 741.

# Paper 3

P3

## VALIDATION OF THE FRINGE REGION TECHNIQUE IN LES OF TURBULENT MASS TRANSFER AT HIGH SCHMIDT NUMBER

François Gurniki<sup>1</sup>, Said Zahrai<sup>2</sup> and Fritz H. Bark<sup>1</sup>

<sup>1</sup>Faxén Laboratory, KTH, S-100 44, Stockholm, Sweden

Abstract. Large-eddy simulations of mass transfer in a turbulent channel flow are considered. Schmidt number is equal to 100 and the turbulent Reynolds number based on the half-width channel to 180. The fringe region technique is tested and validated to reduce the numerical domain of computation to the diffusive boundary layer. Very good agreement is found for the mean and the fluctuating field predicted in this study, with data from earlier numerical simulations. The agreement is also good between computations of the concentration field made in the all channel, and computations reduced to the near-wall region with the help of the fringe technique.

#### 1. Introduction

The process of mass transfer in a diffusive boundary layer becomes very complex in a turbulent flow field. In absence of other effects such as buoyancy, the velocity field induces fluctuations in the mass or concentration field and thereby influences the rate of mass transfer. A thorough understanding of the fundamental transfer mechanisms involved is usually a necessity for the design of various kinds of industrial processes [1].

Although numerous empirical methods have been developed for predicting of rates of mass transfer, see e.g. [2], the general understanding of the underlying physics is still unsatisfactory. To understand the physics of mass transfer in a turbulent velocity field, concentration and velocity fluctuations must be measured in the diffusive boundary layer and correlations between them must be computed. The thickness of the diffusive boundary layer is proportional to the thickness of the hydrodynamic boundary layer ( $\delta_h$ ) divided by Schmidt number to the power one-third [2]. Obviously, for a case of flow at high Reynolds number and high Schmidt number, which is usually of practical interest, the region of importance will be very thin. That makes experimental investigations very difficult, if not impossible. As a result, there is a lack of experimental data describing physics of mass transfer in a turbulent field.

Recent fast advances in computing science and the capacity of computer have created the possibility of performing numerical experiments instead of physical ones. Although numerical simulations of turbulent flows are not free of difficulties, they give, where they can be applied, an accurate and detailed insight on the dynamics of the flow.

<sup>&</sup>lt;sup>2</sup>ABB Corporate Research, SE-721 78, Västerås, Sweden

A possible approach is to make use of models in order to reduce the number of turbulence scales involved. In conventional turbulence models, only the largest scale, comparable to the geometrical size of the region where the flow takes place, are considered. Since a large part of the dynamics is eliminated, elaborate models are needed to make accurate predictions. In large eddy simulations, on the other hand, only the smallest scales, comparable with the size of the mesh, are modeled. These scales are likely to have a more universal dynamics and therefore allow accurate predictions with relatively simple models.

The fringe technique, originally introduced by Spalart [3] can be used for forcing the solution to approach a given value. Fringe technique has been used as an artificial boundary condition in direct simulations of transitional and turbulent viscous boundary layers [4, 5]. Henningson et al. [6] also applied this technique in direct numerical simulation of a turbulent and viscous boundary layer. For the case of mass transfer from a wall at high Schmidt number the fringe technique can force the concentration field to have a given value at a position sufficiently far from the wall without destroying the structure of turbulent field near the wall. In that case, only the near-wall region can be considered for the concentration field. Using such a method may make numerical experimentation of turbulent mass transfer from a reacting wall possible, and provide necessary data for more accurate modeling.

The main goal of this study is to investigate the possibility of application of fringe technique for simulation of turbulent channel flow at high Schmidt number. The paper is organized in the following way: the mathematical problem and the numerical procedure are formulated in section 2. Results from numerical studies are presented in section 3, and the results and conclusions are summarized in section 4.

## 2. Theory

**2.1. Governing equations.** In this study, turbulent flow in an infinitely large channel flow is considered. The walls are assumed to be at a distance of  $2\delta$  (see figure 1) and the flow is driven by a constant pressure gradient, strong enough to make gravitational effects negligible. The coordinate system is chosen so that the walls will be located at  $y = \pm \delta$ .

The flow can be described by the Navier-Stokes equations for an incompressible fluid, the continuity equation, and a mass-transport equation. The equations are adimensionalized by  $u_{\tau}$ , the friction velocity,  $l^* = \nu/u_{\tau}$ , the typical length scale in wall units, and  $l^*/u_{\tau}$  as the typical time scale.

At very high Schmidt number, the diffusive boundary layer is located very near the wall. It is therefore useless to compute the concentration everywhere in the channel flow. For that reason, it is proposed below a method to reduce the mathematical and the numerical domain of investigation to the near-wall region. The domain, as shown in figure 1, lies between the wall and an imaginary plane

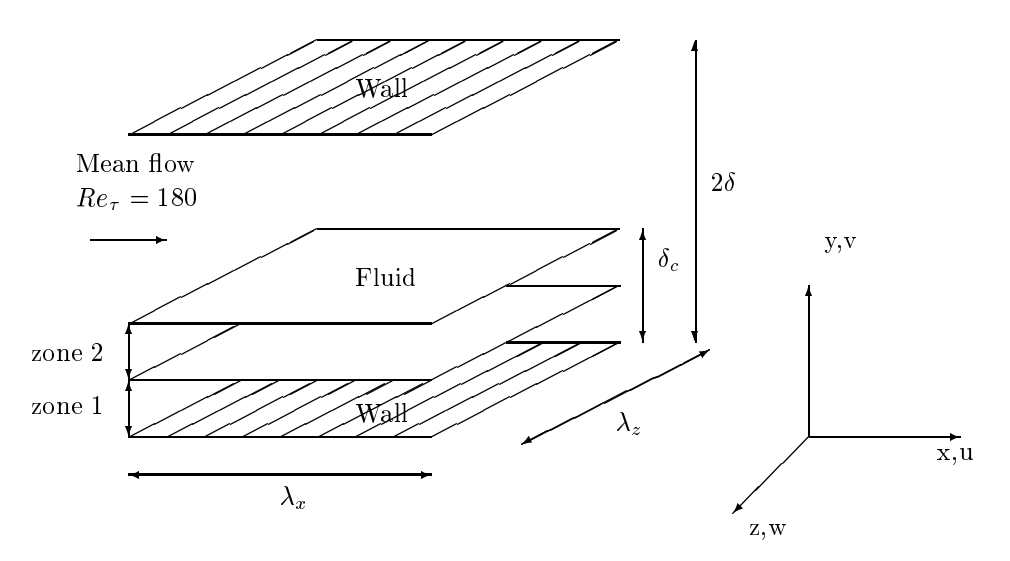


FIGURE 1. The geometry of the cell, the chosen coordinate system and the three regions of computations.

surface in the fluid, parallel to the wall and at a distance of  $\delta_c$  from it.  $\delta_c$  is the approximated thickness of the diffusive boundary layer, and is equal to  $\delta_h/Sc^{1/3}$  [2]. The domain is divided into one conservative region (zone 1), and one region (zone 2) where a source term is added to the mass conservation equation, as shown below

$$\frac{\partial c^{+}}{\partial t^{+}} + (\mathbf{u}^{+} \cdot \nabla^{+}) c^{+} = \frac{1}{Sc} \nabla^{+,2} c^{+} - \lambda^{+} (y^{+}) \cdot (c^{+} - c_{o}^{+}), \tag{1}$$

where  ${\bf u}^+$  denotes the instantaneous velocity field,  $c_o^+$  is a constant, and Sc is the Schmidt number. The concentration field can be made dimensionless by using the mass flux at the wall, i.e.  $c^* = -\frac{D}{u_\tau} \left(\frac{\partial \overline{c}}{\partial y}\right)_{wall}$ , where  $\overline{c}$  corresponds to the averaged value of the instantaneous concentration. All quantities are scaled in wall units. The superscript '+' can therefore be dropped throughout the remainder of this paper. Equation (1) can be used for both regions by choosing properly the function  $\lambda$ , as shown in figure 2. The conservative and the nonconservative region are named zone 1 and 2, respectively. The source term works as a forcing function, imposing to the intantaneous concentration the fixed value of  $c_o$  in zone 2. Throughout the remainder of this paper, the domain containing only zone 1 and 2 will be called the reduced domain.

This technique is here used in order to resolve the problem of the boundary condition for the instantaneous concentration where the boundary of the domain lies in the viscous boundary layer. At this boundary, the velocity field induces turbulence to concentration. The fluctuating part of concentration must then be modelled. In order to avoid this fastidious and hazardous task, the fringe region technique allows to damp to zero the fluctuating part of the passive scalar in

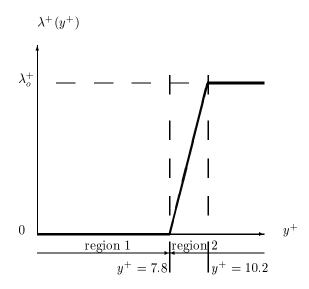


Figure 2. The  $\lambda$  function versus the wall-normal direction.

the vicinity of the boundary of the domain lying in the fluid. It is assumed that the non-physical phenomena occurring in the fringe region do not invalidate the solution in the remaining part (zone 1 in figures 1 and 2) of the computational domain [6]. This assumption will be verified experimentally in this study.

For the hydrodynamical equations, a no-slip condition is used at the walls. The velocity field is always computed in a computational domain that contains both walls of the turbulent channel, and whose width in non-viscous units is  $2\delta$ , see figure 1. As a first step, in order to make comparisons with earlier numerical and experimental investigations, the case of mass transfer when the concentration is set to a given value at the wall is considered. When the domain is reduced to the diffusive boundary layer, one boundary condition is the wall-concentration set to a given value. The other is set in the fluid at the limit of zone 2, with a mixed condition

$$\frac{\partial c}{\partial y}(x, \delta_c, z, t) = c(x, \delta_c, z, t) - c_o. \tag{2}$$

Equation (2) is a non-reflecting boundary condition. It guarantees that error waves travelling from the wall to the centre of the channel are damped, and are not reflected towards the wall [7].

**2.2.** Numerical Procedure. In this large eddy simulation, averaging over the volume of the computational cells is used as the filtering function. The SGS model is here an anisotropic version of the Smagorinsky model, and has been validated in a previous work [8]. A rectangular computational cell, numbered M, has the width in i-direction,  $\Delta x_i^M$ , the area of surface normal to i-direction,  $\Delta s_i^M = \Delta x_j^M \Delta x_k^M$ , and a volume size,  $\Delta v^M = \Delta x_1^M \Delta x_2^M \Delta x_3^M$ . The modelled

Table 1. Specifications of the meshes used without the fringe region technique.

	$N_x$	$N_y$	$N_z$	$\Delta x$	$\Delta z$	$\Delta y_{min}$	$\Delta y_{max}$
$Mesh 1 \times 1 \times 1$	32	42	96	70.6858	11.781	1.4062	18.92
$\mathrm{Mesh}\ 1\times 6\times 1$	32	252	96	70.6858	11.781	0.2344	3.16

Navier-Stokes equation averaged over the volume using the cell M, which gives the dynamics of large eddies resolved on the given mesh, can be expressed as

$$\begin{split} &\Delta v^M \, \frac{\partial \overline{u}_i^M}{\partial t} = \\ &\sum_{j=1}^3 \, \Delta s_j^M \, \left[ - \left( u_i^{(+j)M} \, u_j^{(+j)M} - u_i^{(-j)M} \, u_j^{(-j)M} \right) - \left( p^{(+j)M} - p^{(-j)M} \right) \, \delta_{ij} \right] \\ &+ \sum_{j=1}^3 \, \Delta s_j^M \, \left[ \left( \tau_{ij}^{(+j)M} - \tau_{ij}^{(-j)M} \right) \right] \\ &+ \sum_{j=1}^3 \, \Delta s_j^M \, \left[ \frac{1}{\sqrt{2}} C^2 L_j^2 \left( \left| \overline{s}_{ij}^M \right|^{(+j)M} \cdot s_{ij}^{(+j)M} - \left| \overline{s}_{ij}^M \right|^{(-j)M} \cdot s_{ij}^{(-j)M} \right) \right] \,, \end{split}$$
 error we is the received stress tensor and an twice the instantaneous rate.

where  $\tau_{ij}$  is the resolved stress tensor, and  $s_{ij}$  twice the instantaneous rate of strain tensor  $\left(\frac{\partial u_i}{\partial x_j} + \frac{\partial u_j}{\partial x_i}\right)$ .  $\left|\overline{s}_{ij}^M\right| = \left(\sqrt{\sum_{i=1}^3 \sum_{j=1}^3 \overline{s}_{ij}^{M^2}}\right)$  and  $L_j^2 =$ 

 $(\Delta x_1^M \Delta x_2^M \Delta x_3^M)^{2/9} (\Delta x_j^M)^{4/3}$ . Considering an instantaneous function  $f(\underline{x})$ ,  $\overline{f}^M$  stands for the filtered version of f at the center of cell M, whose volume is  $\Delta v^M$ . The superscript  $(\pm j)M$  denotes that the considered filtered quantity is evaluated on the cell surface whose center is the vector  $\underline{x}^M \pm \frac{1}{2} \Delta x_j^M \underline{e}_j$  and whose normal direction is  $\underline{e}_j$ . The model constant C was set to 0.08, as suggested in [8]. For more detailed information the interested reader is referred to Zahrai  $et\ al\ [8]$ . The mass transport equation is similarly filtered at each cell M.

The computational domain is periodic in the streamwise and the spanwise directions with corresponding periodicity lengths,  $\lambda_x$  and  $\lambda_z$ . The distance between the channel walls is  $2Re_\tau$  in wall-units.  $\lambda_x$  and  $\lambda_z$  are respectively  $4\times\pi\times Re_\tau$  and  $2\times\pi\times Re_\tau$  in wall-units, see figure 1. Periodic boundary conditions are applied for the velocity, the fluctuations of pressure and the concentration in the streamwise and spanwise direction. As a feature of this study, the use of different mesh systems for the fluid velocity field and the concentration field should be pointed out. Table 1 shows the characteristics of two meshes used without the fringe region technique, i.e. with a computational domain extended from a wall to the other and considering the all cross-section of the channel flow. The grid denoted as Mesh  $1\times1\times1$  is used to compute the fluid velocity field. The mesh used to compute the concentration is Mesh  $1\times6\times1$ . When the fringe region technique is used with Mesh  $1\times6\times1$ ,  $N_y=54$ . The grid is uniform in the mean flow direction, and is stretched in the direction normal to the wall, with the finest spacing at the walls.

The turbulent velocity and the concentration were computed successively in the following way: First, the volume average Navier-Stokes equation is solved, and then the fluid velocity field and the eddy diffusivity are interpolated to the mesh system used for the concentration field. With the known velocity field, the volume average mass transport equation is solved. This procedure is repeated by returning to the first step and computation for the next time step.

A fourth order Lagrangian interpolation scheme is used to ensure a sufficient accuracy in interpolation of turbulent velocity field, see e.g. Wang & Squires [9]. The filtered mass transport equation is integrated using a three step, third order tensor viscosity scheme, [10, 11]. The advection term in the right hand side of the filtered equation was approximated with QUICK scheme [12] to keep a second order spatial accuracy and a numerical stability at the same time. The diffusion term was discretized using central differentiation.

The initial profile in a cross section for the velocity was set parabolic. The mass transfer calculation was not added until the hydrodynamic simulation had reached statistically equilibrium state. The initial profile in a cross section for concentration was set proportional to  $y^{-1/5}$  for the calculations made with the fringe region technique. It was set identical to the profile obtained at Sc=1 in [13] for the calculations made without the fringe technique. The calculated variables were considered to be at equilibrium when variation of the statistical properties in time were small.

#### 3. Results

In this section results from numerical studies of turbulent mass transfer in a channel are presented. The flow is assumed to take place at Reynolds number equal to 180 based on the wall-friction velocity and the channel half width and Schmidt number equal to 100. The conditions of computation of the velocity field are exactly the same as those reported in [8], and correspond to case 2 presented in table 1 of that paper. The cell is assumed to be infinite in the streamwise and the spanwise directions, which are simulated by periodic boundary conditions. The main focus is made on the near-wall region and the dynamics of mass Two different numerical techniques are used for computation of the concentration field in the near-wall region. First, a refined mesh is used for the concentration field and the transport equation is integrated in the whole channel as in [13]. Secondly, in order to make the simulation more efficient, only the near-wall region is considered and the concentration field is damped in the outer region using the fringe technique and thereby the size of the grid is reduced. It turns out that simulations made with the reduced grid and the fringe region technique run approximately 5 times faster than with the complete grid between the two walls. After an adimensional time-period of  $60 \cdot Re_{\tau}$  smooth turbulence statistics were obtained with the two numerical techniques. The statistics were then produced during an adimensional integration time of  $8 \cdot Re_{\tau}$  with the fringe region technique, and of  $16 \cdot Re_{\tau}$  with the technique considering the whole channel. In this last case, statistics were still time-dependent after an integration time of  $8 \cdot Re_{\tau}$ .

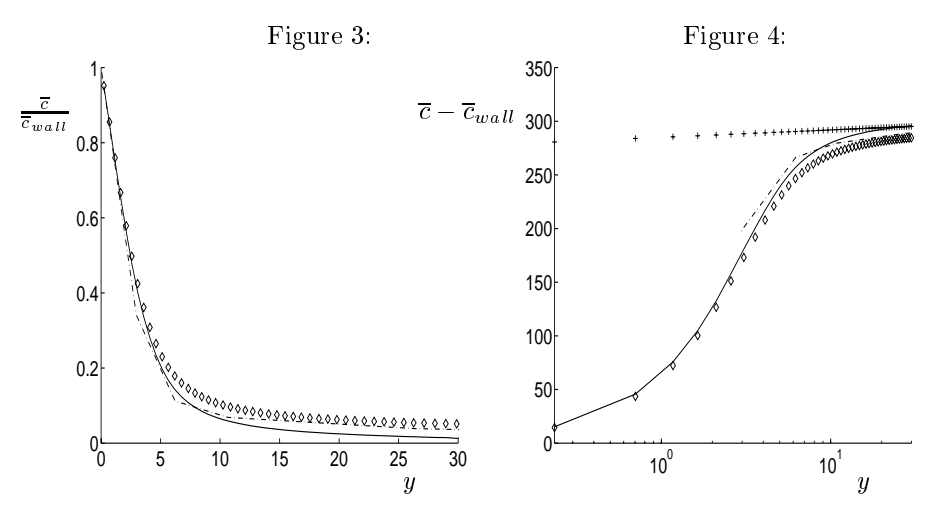


FIGURE 3. The mean concentration at Sc=100 in the wall-normal direction. \_ . \_: Papavassiliou [14], DNS,  $Re_{\tau}=150$ , without fringe region technique. Solid line: Present study, LES,  $Re_{\tau}=180$ , with fringe region technique. Diamonds : Present study, LES,  $Re_{\tau}=180$ , without fringe region technique.

FIGURE 4. The mean concentration at Sc=100 in the wall-normal direction.  $\_$ .  $\_$ : Papavassiliou [14], DNS,  $Re_{\tau}=150$ , without fringe region technique. Solid line: Present study, LES,  $Re_{\tau}=180$ , with fringe region technique. Diamonds: Present study, LES,  $Re_{\tau}=180$ , without fringe region technique.  $++++:c^{+}=3.0 \cdot ln(y^{+})+285.0$ 

The mean concentration profile in the direction normal to the walls is presented figure 3. The concentration is made dimensionless by using reference concentration,  $c^*$ , defined by  $c^* = -\frac{D}{u_\tau} \left( \frac{\partial \overline{c}}{\partial y} \right)_w$ . As can be found in figure 3, good agreement is found with results from direct numerical simulations by Papavassiliou et al. [14]. The slight difference between simulations with and without fringe technique at y around 30 are likely to be due to the differences in the averaging time over which the statistics are computed.

Figure 4 shows the mean concentration profile in a logarithmic diagram. With increasing y, the concentration profile exhibits a buffer layer character, followed by a logarithmic region. As shown in figure 4, the concentration profile fits well with the logarithmic law of  $\overline{c} = 3.0 \cdot ln(y) + 285.0$  after y = 10. The logarithmic profile has been calculated with the same reference concentration as in Papavassiliou *et al.* [14].

Lin et al. [2], estimated the ratio between the hydrodynamic and mass transfer boundary layer thicknesses to be proportional to the third root of the Schmidt number. Thus, the observation made above, i.e. transition to a logarithmic profile at value y=10 is in good agreement with that estimate since the logarithmic region for the velocity profile starts around y=30 [15]. Moreover, the constant

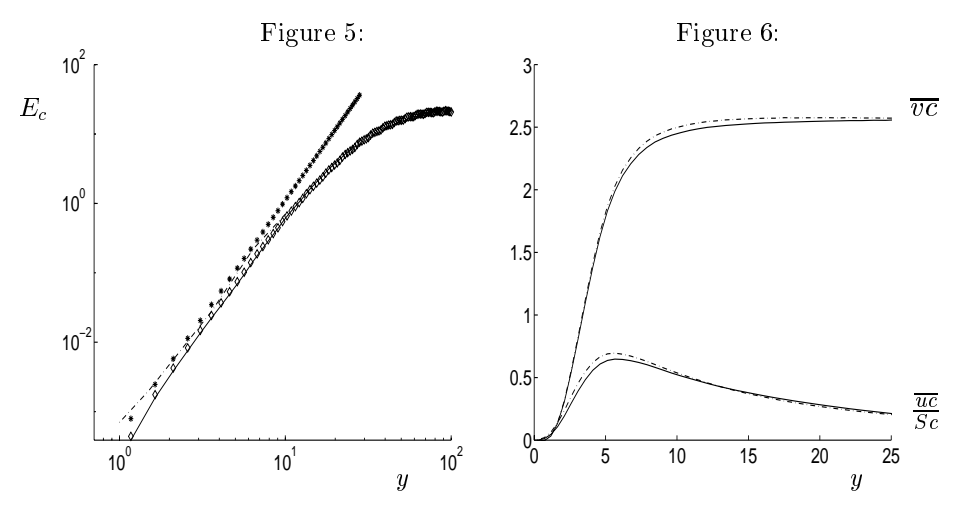


FIGURE 5. The mean eddy diffusivity in the near-wall region at  $Sc=100.****: E_c=0.000463 \cdot y^3$  [14]. \_: Present study with fringe region technique. \_ . \_:Papavassiliou [14], DNS. Diamonds: Present study without fringe region technique.

Figure 6. At Sc=100, the turbulent mass-fluxes. Solid line: Present study, with fringe region technique. Dashed lines: Present study, without fringe region technique.

of proportionality, 3.0, for the logarithmic law found in the present study is close to the values found by Calmet *et al.* [16] and Kader *et al.* [17]. Kader *et al.* [17] found a good fit with a logarithmic law as  $2.12 \cdot ln(y) + \beta(Sc)$ , with  $\beta(Sc) = (3.85 \cdot Sc^{1/3} - 1.3)^2 + 2.12 \cdot ln(Sc)$ , which gives  $\beta(100) = 284.33$ .

 $\beta(Sc) = (3.85 \cdot Sc^{1/3} - 1.3)^2 + 2.12 \cdot ln(Sc)$ , which gives  $\beta(100) = 284.33$ .

The mean eddy diffusivity, defined as  $E_c = -\overline{vc} \left(\frac{d\overline{c}}{dy}\right)^{-1}$ , is presented in figure 5. A good agreement is found between the predictions of the present study, the DNS results of Papavassiliou *et al.* [14], and the empirical profile proposed by Papavassiliou *et al.* [14]. The predictions of the present study with and without the fringe method technique are also in very good agreement.

Streamwise and wall-normal turbulent mass fluxes are presented in figures 6. Good agreement is found between the two predictions of the present study. The present study finds, in agreement with the observation by Kawamura et al. [18], that the concentration fluctuations correlate more strongly with the streamwise velocity than with its normal-wall component. The ratio between the components of the mass-flux vector is of the order of Schmidt number. The RMS levels for the concentration field are calculated and shown in figure 7. The predictions of the present study with and without the fringe region technique are in very good agreement.

The two-point spanwise correlation coefficient of the concentration fluctuations is computed at y = 1.17 and is presented in figure 8. After reaching a

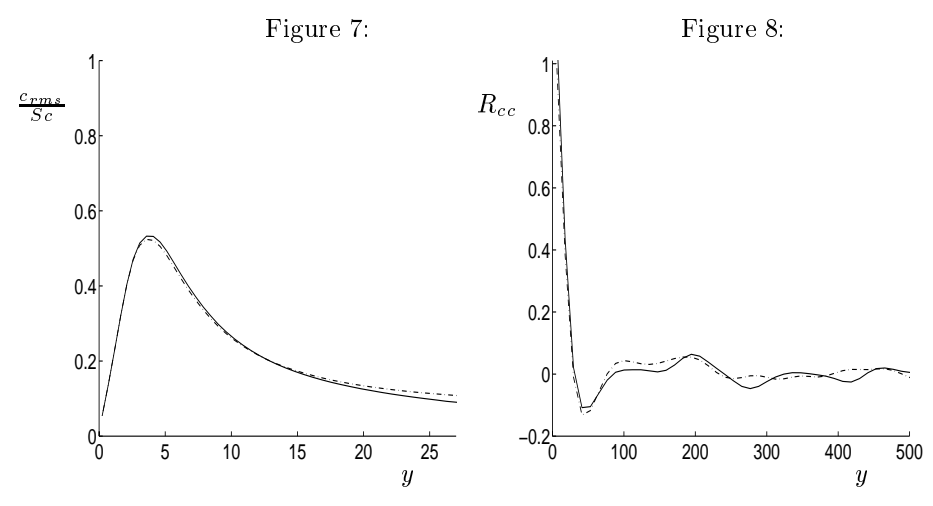


FIGURE 7. RMS levels of the concentration field at Sc=100 in the wall-normal direction. Solid line: Present study, with fringe region technique. Dashed lines: Present study, without fringe region technique.

FIGURE 8. At Sc=100, the spanwise two-point correlation coefficients at  $y^+=1.17$ . Solid line: Present study, with fringe region technique. Dashed lines: Present study, without fringe region technique.

minimum, the correlation coefficient oscillates slightly about zero. Defining the distance to the first local minimum as half of the the mean streak spacing, the concentration streak spacing can be estimated to 100. This value is in good agreement with that obtained by Calmet *et al.* [16].

### 4. Conclusions

In this work, results from large eddy simulations of a model for mass transfer in a turbulent channel flow are presented. All predictions are computed at Schmidt number equal to 100. The fringe region technique is used to diminish the numerical domain of computation. Good agreement is obtained between LES made with and without the fringe region technique. Previous studies are also found to be in good agreement with the predictions of the present study for the mean and the instantaneous concentration field.

## References

- F. Walsh, A first course in electrochemical engineering, The Electrochemical Consultancy, 16 Queens Close, Romsey, Hants SO51 8EG, England, ISBN 0 9517307 1 1
- [2] C.S. Lin, R.W. Moulton and G.L. Putnam (1953), Industrial and Engineering Chemistry, Vol.45 No.3, 636

- [3] P.R. Spalart, Direct numerical study of leading edge contamination in fluid dynamics of three-dimensional turbulent shear flows and transition, AGARD-CP-438, (1988), pp.5.1-5.13.
- [4] P.R. Spalart & J.H. Watmuff, J. Fluid Mech., 249 (1993) 337.
- [5] S. Berlin, A. Lundbladh & D.S. Henningson, *Phys. Fluids*, Vol.2 (1994) No.6, 1949.
- [6] J.Nordström, N. Nordin and D. Henningson, The fringe technique and the Fourier-method used in the direct numerical simulation of spatially evolving viscous flows, SIAM J. Sci. Comp. 20 (1999), 1365.
- [7] D. Givoli, J. Comp. Phys., 94 (1991) 1.
- [8] S. Zahrai, F.H. Bark and R.I. Karlsson, Eur. J. Mech., B/Fluids, 14 (1995) 459.
- [9] Q. Wang & K.D. Squires, Int. J. Multiphase Flow 22 (1996) 667.
- [10] J. K. Ducowicz and J. D. Ramshaw, J. Comput. Phys. 32 (1979) 71.
- [11] B.J. Daky and M.D. Torrey, SOLA-PTS: A transient, three-dimensional alghorithm for fluid-thermal mixing and wall heat transfer in complex geometries NUREG/CR-3822, LA-10132-MS (1984).
- [12] B.P. Leonard, Comput. Meths. Appl. Mech. Eng. 19 (1979) 59.
- [13] F. Gurniki, S. Zahrai and F.H. Bark, *LES of Turbulent Channel Flow of a Binary Electrode*, accepted for publication Journal of Applied Electrochemistry (1999).
- [14] D.V. Papavassiliou and J. Thomas Hanratty, Int. J. Heat Mass Transfer, 40 (1997) 1303.
- [15] H. Tennekes and J.L. Lumley, A first course in turbulence, the MIT press (1972), ISBN 0 262 200 19 8.
- [16] I. Calmet and J. Magnaudet, Phys. Fluids 9 (1997) 438.
- [17] B.A. Kader, Int. J. Heat Mass Transfer 24 (1981) 1541.
- [18] H. Kawamura, K. Ohsaka, H. Abe and K. Yamamoto, Int. J. Heat and Fluid Flow 19 (1998) 482.

# Paper 4

P4

## LARGE-EDDY SIMULATION OF ELECTROCHEMICAL MASS TRANSFER

François Gurniki<sup>1</sup>, Said Zahrai<sup>2</sup> and Fritz H. Bark<sup>1</sup>

<sup>1</sup>Faxén Laboratory, KTH, S-100 44, Stockholm, Sweden

 $^2\mathrm{ABB}$ Corporate Research, SE-721 78, Västerås, Sweden

**Abstract.** Large-eddy simulations of mass transfer in a channel flow working as an electrochemical cell are considered. Schmidt number is equal to 3000 and the turbulent Reynolds number, based on the half-width channel, to 180. The computational domain is reduced to the diffusive boundary layer with the help of a numerical technique. Very good agreement is found with data from previous studies for the mean, the fluctuating field, and the wall-mass-transfer.

### 1. Introduction

The turbulent process of mass transfer in the diffusive boundary layer along an electrode of an electrochemical cell is very complex. In absence of other effects such as buoyancy, the velocity field induces fluctuations in the concentration field, and thereby influences also the rate of wall-mass-transfer. The thickness of the diffusive layer, being inversely proportional to Schmidt number to a certain fractional power, makes experimental investigations on the fluctuations of mass transfer very difficult. Recent advances in computing science have created the possibility of performing numerical experiments instead of physical ones. Turbulent flows involve different length scales. In large-eddy simulations, one models only the smallest, that are likely to have a universal dynamics, and can be modelled with simple models.

The paper is organized in the following way: the mathematical problem and the numerical procedure are formulated in section 2. Results from numerical studies are presented in section 3 and summed up in section 4.

## 2. Theory

In this study, turbulent flow of a binary electrolyte outside the double layers in an infinitely large channel flow, working as an electrochemical cell, is considered. The solution is also assumed to contain a support electrolyte so that the variations of the electrical potential can be neglected. The walls are assumed to be at a distance of  $2\delta$  (see figure 1) and the flow is driven by a constant pressure gradient, strong enough to make gravitational effects negligible. The coordinate system is chosen so that the walls will be located at  $y=\pm\delta$ .

The flow can be described by the Navier-Stokes equations for an incompressible fluid, the continuity equation, and a mass-transport equation. The equations

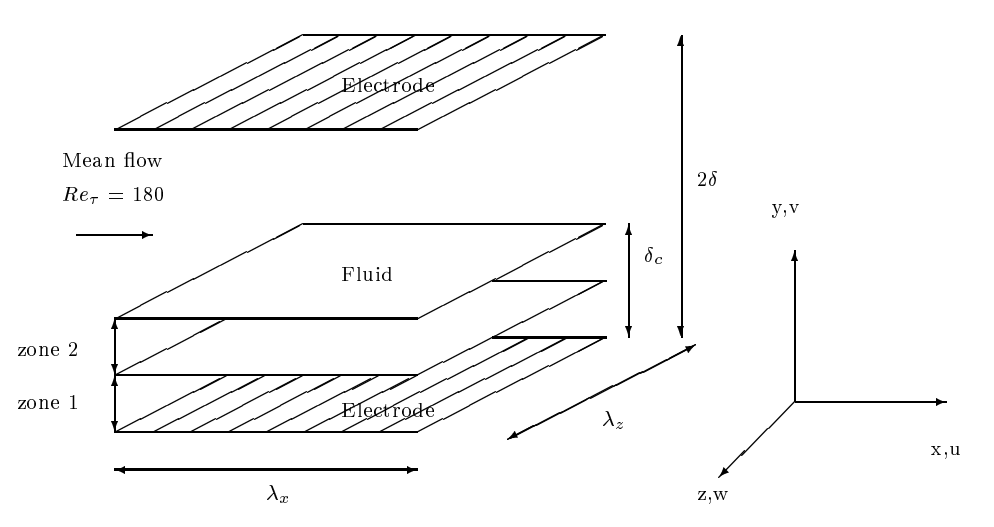


FIGURE 1. The geometry of the cell, the chosen coordinate system and the three regions of computations.

are adimensionalized by  $u_{\tau}$ , the friction velocity,  $l^* = \nu/u_{\tau}$ , the typical length scale in wall units, and  $l^*/u_{\tau}$ , the typical time scale. At very high Schmidt number, the diffusive boundary layer is located very near the wall. It is therefore useless to compute the concentration everywhere in the channel flow. For that reason, it is proposed below a method to reduce the mathematical and the numerical domain of investigation to the near-wall region. The domain, as shown in figure 1, lies between the wall and an imaginary plane surface in the fluid, parallel to the wall and at a distance of  $\delta_c$  from it.  $\delta_c$  is the approximated thickness of the diffusive boundary layer, and is equal to  $\delta_h/Sc^{1/3}$  [1]. The domain is divided into one conservative region (zone 1), and one region (zone 2) where a source term is added to the mass conservation-equation, as shown below

$$\frac{\partial c^{+}}{\partial t^{+}} + \left(\mathbf{u}^{+} \cdot \nabla^{+}\right) c^{+} = \frac{1}{Sc} \nabla^{+,2} c^{+} - \lambda^{+} (y^{+}) \cdot (c^{+} - c_{o}^{+}), \tag{1}$$

where  ${\bf u}^+$  denotes the instantaneous velocity field,  $c_o^+$  is a constant, and Sc is the Schmidt number. The concentration field can be made dimensionless by using the mass flux at the wall, i.e.  $c^* = -\frac{D}{u_\tau} \left(\frac{\partial \overline{c}}{\partial y}\right)_{wall}$ , where  $\overline{c}$  corresponds to the averaged value of the instantaneous concentration. Using the electrical neutrality and given that the present study considers a binary electrolyte, the mass transport-equations can be reduced to equation (1) only. All quantities are scaled in wall units. The superscript '+' can therefore be dropped throughout the remainder of this paper. Equation (1) can be used for both regions by choosing properly the function  $\lambda$ . The source term works as a forcing function, imposing to the intantaneous concentration the fixed value of  $c_o$  in zone 2.

The use of 2 zones as described above is a solution to the problem caused by the boundary condition for the instantaneous concentration at the domain

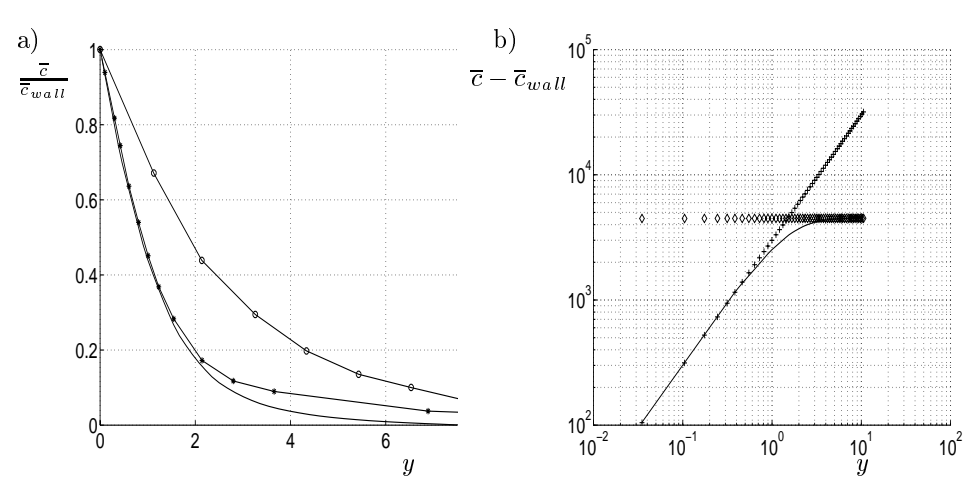


FIGURE 2. The mean concentration in the wall-normal direction. a) Solid line: Present study, LES, at Sc = 3000 and  $Re_{\tau} = 180$ . -\*-\*-: Papavassiliou [3], DNS at Sc = 2400,  $Re_{\tau} = 150$ , Lagrangian method.  $-\circ -\circ -$ : Lin et al. [1], experiments at Sc = 900 and Re = 4850. b) + + ++:  $Sc \cdot y^+$ . diamonds:  $3.0 \cdot ln(y^+) + 4485$ .

boundary that lies in the velocity boundary layer. At this boundary, the velocity field induces turbulence to concentration. The fluctuating part of concentration must then be modelled. In order to avoid this fastidious and hazardous task, the fringe region technique allows to damp to zero the fluctuating part of the concentration in the vicinity of the boundary of the domain lying in the fluid. For the hydrodynamical equations, a no-slip condition is used at the walls. The velocity field is always computed in a computational domain that contains both walls of the turbulent channel, and whose width in non-viscous units is  $2\delta$ , see figure 1. As a first step, in order to make comparisons with earlier numerical and experimental investigations, the case of mass transfer when the concentration is set to a given value at the wall is considered. This case corresponds to an electrochemical cell working at the limiting current. In this large eddy simulation, averaging over the volume of the computational cells is used as the filtering function. The Sub-Grid Scale model is here an anisotropic version of the Smagorinsky model, and has been validated in a previous work. For more detailed information the interested reader is referred to Gurniki et al [2].

## 3. Results

The mean concentration profile in the direction normal to the walls is presented in figure 2. Figure 2a) shows also results from direct numerical simulations by Papavassiliou et al. [3] at Sc = 2400, and experiments done at Sc = 900 by Lin et al. [1]. The viscous units reported in Lin et al. are corrected to correspond to the same velocity profile used in the present study. Figure 2b) shows the mean

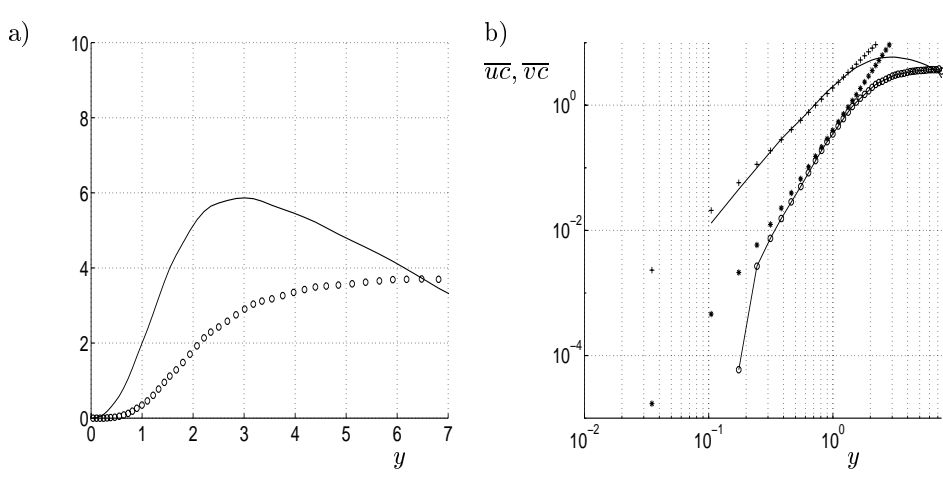


Figure 3. At Sc=3000, the turbulent mass-fluxes. a) Solid line: the streamwise flux  $(\frac{100\cdot \overline{uc}}{Sc})$ .  $\circ \circ \circ$ : The wall-normal flux. b) Solid line:  $\frac{100\cdot \overline{uc}}{Sc}$ .  $-\circ -\circ -: \overline{vc}$ .  $+++: \overline{uc}(y)=1.9\cdot y^2$ . \*\*\*:  $\overline{vc}(y)=1.33\cdot Sc\cdot y^3$ .

concentration profile in a logarithmic diagram. With increasing y, the concentration profile exhibits a buffer layer character, followed by a logarithmic region. As shown in figure 2b), the concentration profile fits well with the logarithmic law  $\overline{c} = 3.0 \cdot ln(y) + 4485.0$ . At Schmidt number equal to 3000 the logarithmic law lies between  $y^+ = 2$  and  $10 \ (\frac{30}{Sc^{1/3}} \le y^+ \le \frac{150}{Sc^{1/3}})$ . As found by Kader *et al.* [4], at very high Schmidt number, the logarithmic law is damped by the constant value of the concentration in the core of the channel.

The mean eddy diffusivity, defined as  $E_c = -\overline{vc}\left(\frac{d\overline{c}}{dy}\right)^{-1}$ , is calculated. Good agreement is found between the predictions of the present study, the DNS results of Papavassiliou et al. [3], and the empirical profile proposed by Shaw et al. [5], stating that  $E_c(y) = 0.000463 \cdot y^3$ . The eddy diffusivity obtained by Papavassiliou et al. was computed with a Lagrangian method by tracking particles and deriving the mean diffusion in time of the particles in the normal-wall direction.

The average mass transfer coefficient is calculated. The result of the present study at Schmidt number equal to 3000 is found to be in good agreement with the DNS of Papavassiliou et al. [3], and the theoretical profile found by Shaw et al. [5] for Schmidt numbers between 600 and 32000 ( $K^+(y) = 0.0889 \times Sc^{-0.704}$ ). The present study found the intensity of the fluctuations for the wall mass-transfer coefficient  $\left(\overline{k^2}\right)^{1/2}/\overline{K}$  equal to 0.197. This result is in good agreement with Campbell et al. [6] at the same Schmidt number, where  $\left(\overline{k^2}\right)^{1/2}/\overline{K}$  was found equal to 0.23.

Streamwise and wall-normal turbulent mass fluxes are presented in figure 3. The streamwise mass-flux is found 30 times larger than in the wall-normal direction. Between Schmidt number 0.05 and 5, Kawamura et al. [7] predicted

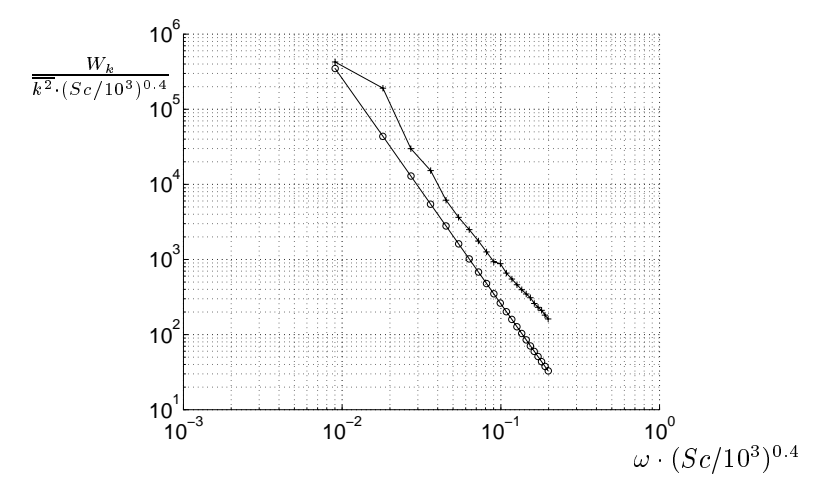


FIGURE 4. Mass transfer spectra versus the non-dimensional time-frequency.  $-\circ-\circ-:$  The theoretical relation  $(4\overline{K}^2W_{\beta}(0))/(\omega^3Sc\cdot\overline{k^2})$  [6].

also a higher streamwise mass-flux than the wall-normal. Figure 3b) shows the asymptotic behaviours of the turbulent mass-fluxes. Good agreement is found with the asymptotic laws found by Kawamura *et al.* [7] for Schmidt number between 0.05 and 5.

The presence of well-known streaky structures elongated in the streamwise direction are clearly observed in (x-z) planes at the interface between the diffusive and the buffer sublayers. Such "concentration-streaks" were also observed by Calmet *et al.* [8].

Figure 4 shows the spectral function of the mass transfer coefficient at the anode. Among the large frequencies, the present study finds a dependency of the spectra proportional to the frequency to the power -3. This result is in very good agreement with an analytical result of Campbell *et al.* [6] based on a linear assumption for the mass-conservation equation.  $\beta$  is here the first coefficient in the Taylor expansion of the wall-normal velocity, see [9].

Particle tracking of fluid particles reveal that, in average, no particle from the outside of the viscous domain travelling towards, enters in it. This result suggests an important contribution of streamwise vortices in wall-mass-transfer fluctuations.

## 4. Conclusions

In this work, results from large-eddy simulations of a model for mass transfer in an electrochemical cell are presented. All predictions are computed at Schmidt number equal to 3000. The fringe region technique is successively used to diminish the numerical domain of computation. Good agreement is obtained with previous studies for the mean and the instantaneous concentration field.

#### References

- [1] Lin C.S.R., Moulton R.W. and Putnam G.L. (1953) Mass Transfer between Solid Wall and Fluid Streams, *Ind. Eng. Chem.* **45**, 636-640.
- [2] Gurniki F., Zahrai S. and Bark F.H. (2000) Validation of the Fringe Region Technique in LES of Turbulent Mass Transfer at High Schmidt Number, 3<sup>rd</sup> Symposium on Turbulence, Heat and Mass Transfer 431-438, Nagoya, april 2-6 2000, Y.Nagano, K.Hanjalić and T.Tsuji (Editors), ©Aichi Shuppan.
- [3] Papavassiliou D.V. and Thomas J. Hanratty (1997) Transport of a Passive Scalar in a Turbulent Channel Flow, Int. J. Heat Mass Transfer 40, 1303-1311.
- [4] Kader B.A. (1981) Temperature and Concentration Profiles in Fully Turbulent Boundary Layers, *Int. J. Heat Mass Transfer* **24**, 1541-1544.
- [5] Shaw D.A. and Hanratty T.J. (1977) Influence of Schmidt Number on the Fluctuations of Turbulent Mass Transfer to a Wall, A. I. Ch. E. Journal 23, 160-168.
- [6] Campbell J.A. and Hanratty T.J. (1983) Mechanism of Turbulent Mass Transfer at a Solid Boundary, A. I. Ch. E. Journal 29, 221-229.
- [7] Kawamura H., Ohsaka K., Abe H. and Yamamoto K. (1998) DNS of Turbulent Heat Transfer in Channel Flow with Low to Medium-high Prandtl Number Fluid, Int. J. Heat Mass Transfer 19 (1998) 482-491.
- [8] Calmet I. and Magnaudet J. (1997) Large-eddy Simulation of High-Schmidt Number Mass Transfer in a Turbulent Channel Flow, *Phys. Fluids* 9, 438-455.
- [9] Hallbäck M., Henningson D.S., Johansson A.V. and Alfredsson P.H. (1996)
   Turbulence and Transition Modelling, ERCOFTAC Series, kluwer Academic Publishers.

# Paper 5

P5

# ON NEAR-WALL TURBULENT PASSIVE-SCALAR TRANSFER AT HIGH SCHMIDT NUMBER

François Gurniki<sup>1</sup>, Said Zahrai<sup>2</sup> and Fritz H. Bark<sup>1</sup>

<sup>1</sup>Faxén Laboratory, KTH, S-100 44, Stockholm, Sweden

<sup>2</sup>ABB Corporate Research, SE-721 78, Västerås, Sweden

Abstract. Large-eddy simulation (LES) of turbulent passive-scalar transfer at the walls of a three-dimensional channel flow was carried out for various Schmidt numbers ranging from 1 to 3000. The turbulent Reynolds number based on the channel half-width was 180. The budgets for the Reynolds-flux vector, the scalar variance-rate and the scalar dissipation-rate were studied. Good agreement was found with previous studies at Schmidt number around unity. The terms in the budgets for the Reynolds-flux vector and the scalar variance-rate were shown to be influenced by Schmidt number, but, somewhat surprisingly, not the budget of the dissipation-rate. Approximate versions for the budgets are given.

#### 1. Introduction

Turbulent transport of a passive scalar at high Schmidt number plays an important role in many engineering applications, like in the field of electrochemistry. Most of these applications involve turbulent flows at such high Reynolds numbers that they cannot be directly simulated. One must then face the tricky problem of modeling the Reynolds fluxes. The eddy-diffusivity approach is unable to give a correct prediction of  $\overline{u_i\theta}$ , where  $u_i$  and  $\theta$  are the fluctuating part of the velocity and the passive-scalar, respectively. As an example, the streamwise mass flux  $\overline{u\theta}$  in a fully developed channel flow is in that way predicted equal to zero. To involve more of the physics, algebraic scalar-flux models in a two-equation model can be obtained from the transport equations for the Reynolds fluxes. The formulation of these models are obtained with the help of some equilibrium assumptions in the budget of the transport equations. In transport-equation modeling of the passive scalar flux, the scalar variance  $\overline{\theta}^2$  and the scalar dissipation rate  $\epsilon_{\theta}$  are also needed, because algebraic models require the dynamical and the scalar time-scales [1].

In documented literature, budgets of streamwise and wall-normal turbulent scalar flux have been computed for different Schmidt numbers between 0.025 and 5 [2, 3]. At Schmidt number around unity, it was found that the dominating terms in the budgets for the wall-normal and the streamwise scalar fluxes were the production term and the sum,  $\psi_i$ , of the scalar pressure-gradient term and the dissipation. In the near-wall region the transport terms, also called molecular and turbulent diffusion, were balancing  $\psi_i$  and the production term was negligible. For the transport equation of the scalar variance, dissipation was

balancing production, except in the near-wall region where the transport terms were balancing dissipation. To the knowledge of the present authors, there are no published studies of the budget for Reynolds flux at Schmidt numbers higher than 5. With the help of a Lagrangian method, Papavassiliou *et al.* [20] predicted the eddy conductivity but did not study the Reynolds flux.

In a previous study, Gurniki et al. [5] checked the accuracy of large-eddy simulations in a channel flow with mass transfer at Schmidt number equal to 100. The simulation used a numerical technique to reduce the computational domain for the passive-scalar field to the diffusive boundary layer. This so called fringe region technique had been previously used for computations of more difficult flows, like an increasing hydrodynamic boundary layer along a flat plate [6, 7, 8]. At high Schmidt number, the diffusion process is very slow. If the mass flux is due to reactions at the wall, even the convective transport is very slow because the mass transfer occurs close to the wall. If one used a computational domain larger than the diffusive boundary layer, it would need a very long computational time in order to obtain acceptable statistics at equilibrium.

The goal of the present work is to provide a study of the equation for the Reynolds-flux vector, the scalar-variance rate and the dissipation-rate, at Schmidt number (Sc) equal to 100 and 3000. Computations at Sc = 1 and an analytic study of the near-wall region are also made for validation. The paper is organized in the following way: the mathematical problem is formulated in section 2 and the numerical procedure is detailed in section 3. Results from numerical studies are presented in section 4 and conclusions presented in section 5.

#### 2. Theory

In this study, turbulent flow in an infinitely large channel flow is considered. The walls are assumed to be at a distance of  $2\delta$  (see figure 1) and the flow is driven by a constant pressure gradient, strong enough to make gravitational effects negligible. The coordinate system is chosen so that the walls are located at  $y=\pm\delta$ .

The flow can be described by the Navier-Stokes equations for an incompressible fluid, the continuity equation, and a transport equation for the passive scalar. The equations are nondimensionalized by  $u_{\tau}$ , the friction velocity,  $l^* = \nu/u_{\tau}$ , the length scale in wall units, and  $l^*/u_{\tau}$ , the time scale. The scalar field  $\theta$  can be made dimensionless by using the mean scalar flux at the wall, i.e.  $-\frac{D}{u_{\tau}}\left(\frac{\partial \Theta}{\partial y}\right)_{wall}$ , where  $\Theta$  is the mean value of the dimensional instantaneous scalar, and D the scalar diffusivity.

At very high Schmidt number, the diffusive boundary layer is located very close to the walls. Outside this layer, the distribution of the mean passive-scalar  $\theta$  is almost uniform. It is therefore useless to compute the scalar everywhere in the channel. For that reason, a method to reduce the mathematical and the numerical domain of investigation to the near-wall region is outlined below. For

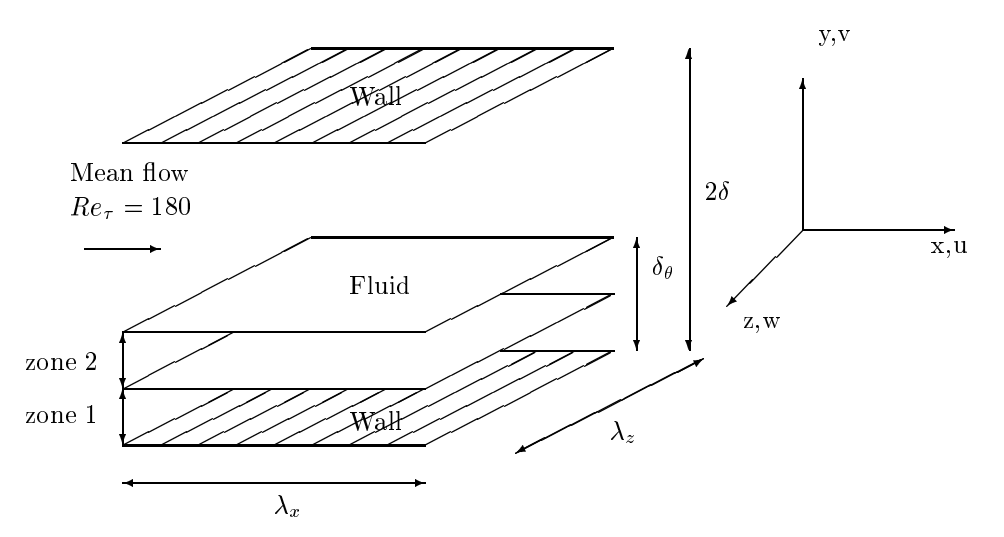


FIGURE 1. The geometry of the channel flow, the three regions of computation, and the chosen coordinate system.

details, the reader is referred to [5, 8]. The domain, as shown in figure 1, lies between the wall and an imaginary plane surface in the fluid, parallel to the wall and at a distance of  $\delta_{\theta}$  from it.  $\delta_{\theta}$  is sufficiently larger than the diffusive and the logarithmic sublayers for mass, and can be estimated as  $\delta_h/Sc^{1/3}$  [9], where  $\delta_h$  is the thickness of the hydrodynamic boundary layer. Here, since the flow is fully developed,  $\delta_h$  can be approximated as  $\delta^+=180$ , and  $\delta^+_{\theta}=12.5$ . The domain is divided into the conservative region 1 where  $|\nabla\theta^+|\neq 0$ , and region 2 where a source term is added to the scalar conservation-equation to force  $\theta$  to approach a given value. This can be done as follows

$$\frac{\partial \theta^{+}}{\partial t^{+}} + \left(\mathbf{u}^{+} \cdot \nabla^{+}\right) \theta^{+} = \frac{1}{Sc} \nabla^{+,2} \theta^{+} - \lambda^{+} (y^{+}) \cdot (\theta^{+} - \theta_{o}^{+}), \tag{1}$$

where  $\mathbf{u}^+$  and  $\theta^+$  denote the instantaneous velocity and scalar fields, respectively.  $\theta_o^+$  is a constant, and Sc is Schmidt number. Equation (1) can be used for both regions by choosing properly the function  $\lambda^+$ , as shown in figure 2. The slope of the ramp function  $\lambda^+$  is here taken equal to 0.13 in wall-units. The source term works as a forcing function, imposing to the intantaneous scalar the fixed value of  $\theta_o^+$  in region 2. Throughout the remainder of this paper, the domain containing only regions 1 and 2 will be called the reduced domain. The height of region 1 is equal to 63% of  $\delta_\theta^+$ .

The fringe technique is here used in order to formulate a boundary condition for the instantaneous scalar at the edge of the diffusive boundary layer. At this boundary, the turbulent velocity field induces fluctuations to the scalar. The fluctuating part of the scalar must then be modelled. In order to simplify this fastidious and hazardous task, a very crude model is chosen. The fringe region

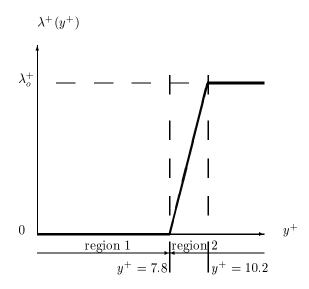


Figure 2. The  $\lambda$  function versus the wall-normal direction.

technique annihilates the fluctuating part of the passive scalar in the vicinity of the boundary of the reduced domain. It is bluntly assumed that the non-physical phenomena occuring in the fringe region do not invalidate the solution in the remaining part of the computational domain [10] (region 1 in figures 1 and 2). This assumption has been verified by numerical experiments in [5]. Hereforth, all variables are nondimensionalized in wall-units. The '+' supersripts are therefore dropped for notational simplicity. As a first step, in order to make comparisons with earlier numerical and experimental investigations, the case of a scalar set constant at the wall is considered. The other boundary is set in the fluid at the limit of region 2, with a mixed condition

$$\frac{\partial \theta}{\partial y}(x, \delta_{\theta}, z, t) = \theta(x, \delta_{\theta}, z, t) - \theta_{o}. \tag{2}$$

Equation (2) is a non-reflecting boundary condition. It guarantees that error waves travelling from the wall to the centre of the channel are damped, and are not reflected towards the wall [11].

For the hydrodynamical equations, a no-slip condition is used at the walls. The velocity field is always computed in a computational domain that contains both walls of the turbulent channel, and whose width in dimensional units is  $2\delta$ , see figure 1.

#### 3. Numerical Procedure

In this large-eddy simulation, averaging over the volume of the computational cells is used as the filtering function. The SGS model is here an anisotropic version of the Smagorinsky model, and has been validated in a previous work [12].

A rectangular computational cell, numbered M, has the width in i-direction,  $\Delta x_i^M$ , the area of surface normal to i-direction,  $\Delta s_i^M = \Delta x_j^M \Delta x_k^M$ , and a volume size,  $\Delta v^M = \Delta x_1^M \Delta x_2^M \Delta x_3^M$ . The modelled Navier-Stokes equation averaged over the volume using the cell M, which gives the dynamics of large eddies resolved on the given mesh, can be expressed as

 $\begin{array}{l} \Delta v^M \, \frac{\partial \overline{u}_i^M}{\partial t} = \\ \sum_{j=1}^3 \Delta s_j^M \, \left[ - \left( u_i^{(+j)M} \, u_j^{(+j)M} - u_i^{(-j)M} \, u_j^{(-j)M} \right) - \left( p^{(+j)M} - p^{(-j)M} \right) \delta_{ij} \right] \\ + \sum_{j=1}^3 \Delta s_j^M \, \left[ \left( \tau_{ij}^{(+j)M} - \tau_{ij}^{(-j)M} \right) \right] \\ + \sum_{j=1}^3 \Delta s_j^M \, \left[ \frac{1}{\sqrt{2}} C^2 L_j^2 \left( \left| \overline{s}_{ij}^M \right|^{(+j)M} \cdot s_{ij}^{(+j)M} - \left| \overline{s}_{ij}^M \right|^{(-j)M} \cdot s_{ij}^{(-j)M} \right) \right] , \\ \text{where } \tau_{ij} \text{ is the resolved stress tensor, and } s_{ij} \text{ twice the instantaneous strain rate tensor, } \left( \frac{\partial u_i}{\partial x_j} + \frac{\partial u_j}{\partial x_i} \right) \cdot \left| \overline{s}_{ij}^M \right| \text{ denotes the magnitude of twice the strain rate tensor, } \left( \sqrt{\sum_{i=1}^3 \sum_{j=1}^3 \overline{s}_{ij}^M} \right), \text{ and } L_j^2 \text{ is the length-scale related to the mesh sizes according to } \left( \Delta x_1^M \Delta x_2^M \Delta x_3^M \right)^{2/9} (\Delta x_j^M)^{4/3}. \text{ Considering an instantaneous function } f(\underline{x}), \overline{f}^M \text{ stands for the filtered version of } f \text{ at the center of cell } M, \text{ whose volume is } \Delta v^M. \text{ The superscript } (\pm j)M \text{ denotes that the considered filtered quantity is evaluated on the cell surface whose center is located at the vector } \underline{x}^M \pm \frac{1}{2} \Delta x_j^M \underline{e}_j \text{ and whose normal direction is } \underline{e}_j. \text{ The model constant } C \text{ was set to } 0.08, \text{ as suggested in } [12]. \text{ The scalar transport equation is similarly filtered at each cell } M. \text{ For more detailed information the interested reader is referred to Gurniki } et al. [13]. \end{array}$ 

The computational domain is periodic in the streamwise and the spanwise directions with corresponding periodicity lengths,  $\lambda_x$  and  $\lambda_z$ . The distance between the channel walls is  $2Re_{\tau}$  in wall-units.  $\lambda_x$  and  $\lambda_z$  are respectively  $4 \times \pi \times Re_{\tau}$ and  $2 \times \pi \times Re_{\tau}$  in wall-units, see figure 1. Periodic boundary conditions are applied for the velocity, the fluctuations of pressure and the passive scalar, in the streamwise and spanwise directions. As a feature of this study, the use of different mesh systems for the fluid velocity field and the scalar field should be pointed out. Table 1 shows the characteristics of two meshes. The first mesh, denoted as Mesh  $1 \times 1 \times 1$ , has a computational domain extended from a wall to the other and considers the whole cross-section of the channel flow. It is used to compute the fluid velocity field and the mass transfer at Sc = 1. The mesh used to compute the passive scalar at higher Schmidt numbers is denoted as Mesh  $1 \times 6 \times 1$ , and is limited to zone 1 and 2 in figures 1 and 2. The grids are uniform in the mean flow direction, and are stretched in the direction normal to the wall, with the finest spacing at the walls. The turbulent velocity and the scalar are computed successively in the following way: the Navier-Stokes equation is advanced one step in time, and then the fluid velocity field and the eddy diffusivity are interpolated onto the mesh system used for the scalar field. With the known velocity field, the volume average scalar transport-equation is solved.

Table 1. Specifications of the meshes.

	$N_x$	$N_y$	$N_z$	$\Delta x$	$\Delta z$	$\Delta y_{min}$	$\Delta y_{max}$
$Mesh 1 \times 1 \times 1$	32	42	96	70.7	11.8	1.41	18.9
$Mesh \ 1 \times 6 \times 1$	32	54	96	70.7	11.8	0.03	0.42

This procedure is repeated by returning to the first step and computation for the next time step.

A fourth order Lagrangian interpolation scheme is used to ensure a sufficient accuracy in interpolation of turbulent velocity field, see e.g. Wang & Squires [14]. The filtered scalar transport-equation is integrated using a three step, third order tensor viscosity scheme, [15, 16]. The advection term in the right hand side of the filtered equation was approximated with QUICK scheme [17] to keep a second order spatial accuracy and a numerical stability at the same time. The diffusion term was discretized using a central differentiation.

The initial profile in a cross section for the velocity was set parabolic. The passive scalar calculation was not added until the hydrodynamic simulation had reached statistically equilibrium state. The initial profile in a cross section for the scalar was set linear at Sc=1, and was set proportional to  $y^{-1/5}$  for the calculations made at Sc=100. It was set identical to the profile obtained at Sc=100 for the calculations made at Sc=3000. The calculated variables were considered to be at equilibrium when variation of the statistical properties in time was small.

#### 4. Results

In this section results from simulations are given at Schmidt numbers equal to 1, 100 and 3000. The flow Reynolds number is 180. The present work checks first that the asymptotic behaviours of the budgets for the Reynolds-flux vector are properly predicted by the computations. If the computational method is not asymptotically correct, it would fail to yield a correct prediction of the flow in the near-wall region [18].

In a second part, the influence of Schmidt number on the Reynolds-flux budget, the scalar variance-rate budget and the scalar dissipation-rate budget is studied. The results obtained at Schmidt number equal to one are used to validate the present computations with the help of previous studies.

At Schmidt number equal to 100 and 3000, Gurniki et al. [5, 19] already validated the present computational method for the prediction of the budget for the passive-scalar. Figures 3a-b show the mean passive-scalar in the diffusive and the logarithmic sublayers at these two Schmidt numbers. One can see that  $\Theta$  tends to a logarithmic profile in the logarithmic layer of the boundary layer for mass transfer.



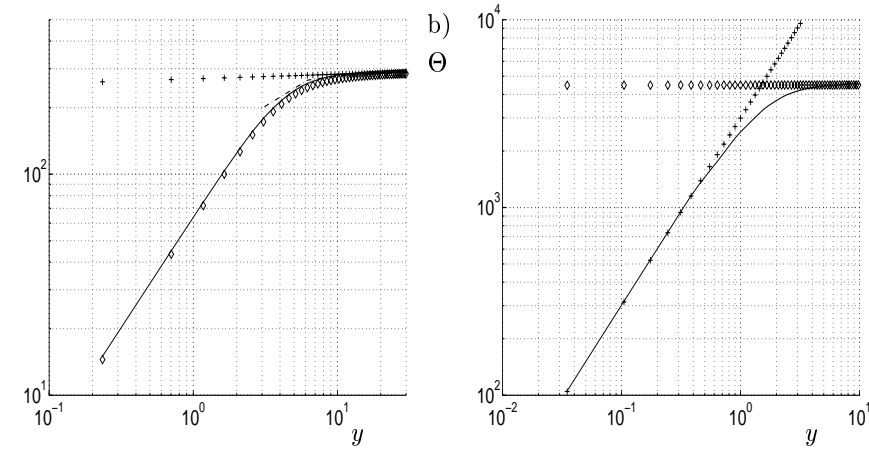


FIGURE 3. The mean passive-scalar along the wall-normal direction. a) At Sc=100. \_ . \_: Papavassiliou [20], DNS,  $Re_{\tau}=150$ , without fringe region technique. Solid line: Present study, LES,  $Re_{\tau}=180$ , with fringe region technique. : Present study, LES,  $Re_{\tau}=180$ , without fringe region technique. + + + +:  $\Theta=3.0 \cdot ln(y)+285.0$ . b) At Sc=3000. Solid line: Present study, LES,  $Re_{\tau}=180$ , with fringe region technique. ++++:  $Sc \cdot y^+$ .  $\diamond \diamond \diamond \diamond : \Theta=3.0 \cdot ln(y)+4485$ .

**4.1. Near-wall behaviour of the budgets.** In a fully developed channel flow, the mean velocity  $(U_i)$  and the passive scalar  $(\Theta)$  vary only with the wall-normal direction y

$$0 = -\frac{\partial P}{\partial x} + \frac{\partial}{\partial y} \left\{ \frac{\partial U}{\partial y} - \overline{uv} \right\},$$

$$0 = -\frac{\partial P}{\partial y} + \frac{\partial}{\partial y} \left\{ -\overline{v^2} \right\},$$
(3)

where  $\frac{\partial P}{\partial x} = \Gamma_o = -\frac{1}{Re}$ . Integrating these two equations, one obtains

$$P = P_o - \overline{v^2}(y) + \Gamma_o x,$$

$$\frac{\partial U}{\partial y} - \overline{uv} = \Gamma_o y + R_{o1},$$
(4)

where  $R_{o1} = 1$ . Similarly as above, the mass-conservation equation can be simplified when the flow in the channel is fully developed

$$0 = \frac{\partial}{\partial y} \left\{ \frac{1}{Sc} \frac{\partial \Theta}{\partial y} - \overline{v\theta} \right\},$$
which gives, 
$$\frac{1}{Sc} \frac{\partial \Theta}{\partial y} - \overline{v\theta} = \tau_o = -1,$$
(5)

where  $\tau_o = \frac{1}{Sc} (\frac{\partial \Theta}{\partial y})_{wall}$ . To analyse the near-wall behaviour of the different terms in the budget equations, we will expand the instantaneous velocity and the scalar in Taylor series as follows

$$u = u_1 = b_1 y + c_1 y^2 + d_1 y^3 + \dots$$

$$v = u_2 = c_2 y^2 + d_2 y^3 + \dots$$

$$w = u_3 = b_3 y + c_3 y^2 + d_3 y^3 + \dots$$

$$\theta = Sc(b_\theta y + c_\theta y^2 + d_\theta y^3 + \dots)$$

$$p = a_p + b_p y + c_p y^2 + d_p y^3 + \dots$$

where the coefficients  $a_p$ ,  $b_1$ ,  $b_2$ ,... are functions of x, z and t. The indices 1, 2 and 3 correspond to the x-, y- and z-direction, respectively. The coefficient  $c_2$  in the  $u_2$  expansion is related to the coefficients  $b_1$  and  $b_2$  through the continuity equation

$$2c_2 = -(b_{1,1} + b_{3,3}). (6)$$

The following asymptotic behaviours for  $\Theta$  and U are known

$$\Theta = \Theta_{wall} - y \cdot Sc + O(y^2),$$
  

$$U = y + O(y^2).$$

From equations (4) and (5), and the Taylor series of the velocity and the passive scalar, one obtains

$$\Theta = \Theta_{wall} - y \cdot Sc + \frac{Sc^{2}\overline{c_{2}b_{\theta}}}{4}y^{4} + O(y^{5}),$$

$$U = y + \frac{\Gamma_{o}}{2}y^{2} + \frac{\overline{b_{1}c_{2}}}{4}y^{4} + O(y^{5}).$$

In analogy with the transport equations for the Reynolds stresses, a transport equation of the scalar-flux vector can be written in symbolic form as

$$\frac{D\overline{u_i\theta}}{Dt} = P_{\theta i} + \Pi_{\theta i} - \epsilon_{\theta i} + D_i, \tag{7}$$

where  $D/Dt = \partial/\partial t + U_k \partial/\partial x_k$ , and the terms in the right-hand-side of are

$$P_{\theta i} = -\left[\overline{u_i u_k}\Theta_{,k} + \overline{u_k \theta}U_{i,k}\right]$$
 production rate,

 $\Pi_{\theta i} = \overline{p\theta_{,i}}$  pressure scalar-gradient term,

$$\epsilon_{\theta i} = \left(1 + \frac{1}{Sc}\right) \overline{\theta_{,k} u_{i,k}}$$
 diffusive destruction rate,

$$D_i = -\left(\overline{u_i u_k \theta} + \overline{p \theta \delta_{ik}} - \frac{1}{Sc} \overline{u_i \theta_{,k}} - \overline{\theta u_{i,k}}\right)_{,k}$$
transport term.

Kawamura et al. [3] consider  $\Pi_{\theta i}$  equal to  $-\overline{\theta p_{,i}}$ . The two expressions are equivalent since the flow is fully developed.

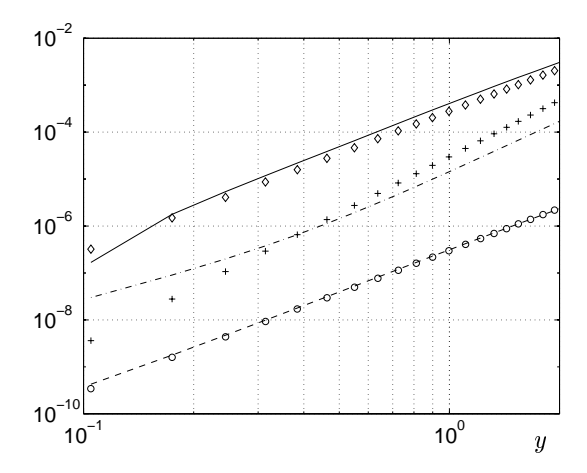


FIGURE 4. At Sc=3000, the production rates in the near-wall region.  $-P_{\theta 1}$ : \_\_ numerical,  $P_{\theta 2}$ : \_\_ . \_ numerical ,  $-P_{\theta 3}$ : \_\_ . \_ numerical,  $-P_{\theta 1}$ :  $\diamond \diamond \diamond \diamond$  analytic  $(2.8 \cdot 10^{-4} \cdot y^3)$ ,  $P_{\theta 2}$ : + + ++: analytic  $(3.0 \cdot 10^{-5} \cdot y^4)$ ,  $-P_{\theta 3}$ :  $\circ \circ \circ \circ$  analytic  $(3.0 \cdot 10^{-7} \cdot y^3)$ .

Using the Taylor series above,  $P_{\theta i}$ ,  $\Pi_{\theta i}$ ,  $\epsilon_{\theta i}$  and  $D_i$  can be expanded as follows

$$P_{\theta 1} = Sc(\overline{b_1 c_2} - \overline{c_2 b_{\theta}})y^3 + O(y^4),$$

$$P_{\theta 2} = Sc \cdot \overline{c_2^2} \cdot y^4 + O(y^5),$$

$$P_{\theta 3} = Sc \cdot \overline{b_3 c_2} \cdot y^3 + O(y^4).$$
(8)

Figure 4 compares expressions (8) with the numerical predictions.

The coefficients of proportionality in these expressions, so as in all the following Taylor series of the budgets, are determined graphically. Good agreement is obtained. The slope of the computed wall-normal production has an order slightly lower than the theoretical in the region described by the three nodes nearest to the wall. The linear interpolation of the velocity field between the two mesh systems is believed to be responsible for this discrepancy. Since the streamwise and the spanwise component of the velocity vector vary linearly in the near-wall region, the production terms in these two directions are correctly predicted.

Similarly, from the Taylor series of the velocity components, of pressure and the passive scalar, one finds for the pressure scalar-gradient terms

$$\Pi_{\theta 1} = Sc \cdot \overline{a_p b_{\theta, x}} \cdot y + O(y^2),$$

$$\Pi_{\theta 2} = Sc \left[ \overline{a_p b_{\theta}} + (2\overline{a_p c_{\theta}} + \overline{b_p b_{\theta}}) y \right] + O(y^2),$$

$$\Pi_{\theta 3} = Sc \cdot \overline{a_p b_{\theta, z}} \cdot y + O(y^2).$$
(9)

Figure 5 compares the analytic behaviours in the three directions with the numerical predictions of the present study. Good agreement is found.

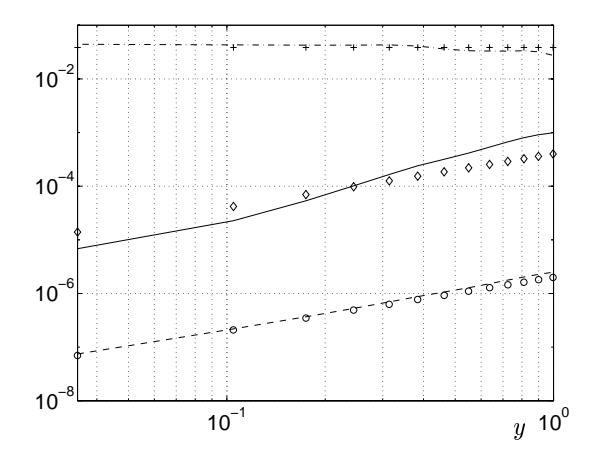


FIGURE 5. At Sc = 3000, the pressure scalar-gradient terms in the near-wall region.  $\Pi_{\theta 1}$ : \_\_ numerical,  $-\Pi_{\theta 2}$ : \_ . \_ numerical,  $-\Pi_{\theta 3}$ : \_ \_ numerical,  $\Pi_{\theta 1}$ :  $\diamond \diamond \diamond \diamond$  analytic  $(4.0 \cdot 10^{-4} \cdot y)$ ,  $-\Pi_{\theta 2}$ : + + + + analytic  $(3.86 \cdot 10^{-2})$ ,  $-\Pi_{\theta 3}$ :  $\circ \circ \circ \circ$  analytic  $(2.0 \cdot 10^{-6} \cdot y)$ .

The near-wall limits of the diffusive destruction rates in the three directions are

$$\epsilon_{\theta 1} = (Sc + 1) \left[ \overline{b_1 b_{\theta}} + 2(\overline{c_1 b_{\theta}} + \overline{b_1 c_{\theta}}) y \right] + O(y^2),$$

$$\epsilon_{\theta 2} = 2(Sc + 1) \overline{c_2 b_{\theta}} \cdot y + O(y^2),$$

$$\epsilon_{\theta 3} = (Sc + 1) \left[ \overline{b_3 b_{\theta}} + 2(\overline{c_3 b_{\theta}} + \overline{b_3 c_{\theta}}) y \right] + O(y^2).$$
(10)

Figure 6 shows a good agreement between the large-eddy simulations of the present study and the Taylor series.

In the streamwise direction, the first order approximation is found to be correct until  $y^=1$ , while it is correct only until y=0.8 in the wall-normal direction. In the spanwise direction, the zero order approximation is valid only when y is less than 0.35. Levich [21], and later Lin *et al.* [9], proposed that the thickness of the diffusive boundary layer,  $\delta_{\theta}$ , would be of the order of magnitude of  $\delta_h \cdot Sc^{-1/3}$ . According to this result,  $y \leq 0.35 = 5/Sc^{1/3}$  corresponds to the limit of the diffusive sublayer.

The Taylor-series of the transport terms in the three directions are presented below

$$D_{1} = (1 + Sc)\overline{b_{1}b_{\theta}} + 6(\overline{b_{1}c_{\theta}} + \overline{c_{1}b_{\theta}})y + O(y^{2}),$$

$$D_{2} = -Sc \cdot \overline{a_{p}b_{\theta}} + 2\left[(1 + Sc)\overline{c_{2}b_{\theta}} - Sc(\overline{a_{p}c_{\theta}} + \overline{b_{p}b_{\theta}})\right]y + O(y^{2}),$$

$$D_{3} = (1 + Sc)\overline{b_{3}b_{\theta}} + 6(\overline{b_{3}c_{\theta}} + \overline{c_{3}b_{\theta}})y + O(y^{2}).$$
(11)

Figure 7 shows good agreement between the large-eddy simulations and the Taylor series. The zero order approximation of the wall-normal and streamwise transport terms are found to be valid also in the buffer layer of the diffusive

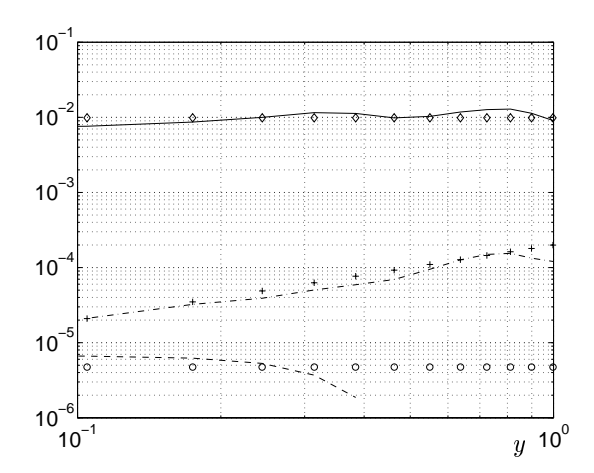


FIGURE 6. At Sc = 3000, the diffusive destruction rates in the nearwall region.  $-\epsilon_{\theta 1}$ : \_\_ numerical,  $\epsilon_{\theta 2}$ : \_\_ . \_ numerical,  $-\epsilon_{\theta 3}$ : \_\_ \_ numerical,  $-\epsilon_{\theta 1}$ :  $\diamond \diamond \diamond \diamond$  analytic  $(1.0 \cdot 10^{-2})$ ,  $\epsilon_{\theta 2}$ : + + ++ analytic  $(2.0 \cdot 10^{-4} \cdot y)$ ,  $-\epsilon_{\theta 3}$ :  $\circ \circ \circ \circ$  analytic  $(4.2 \cdot 10^{-6})$ .

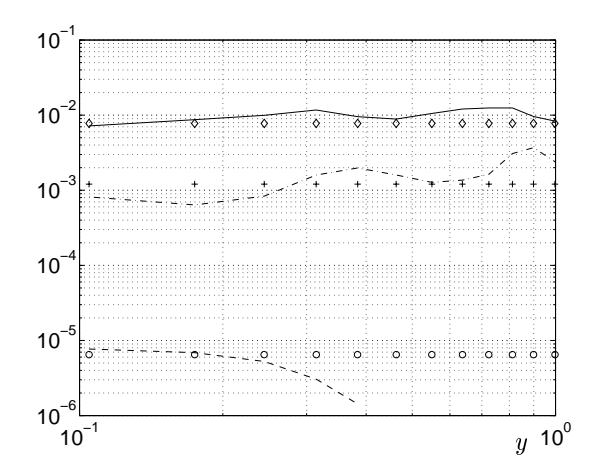


FIGURE 7. At Sc=3000, the transport terms in the near-wall region.  $-D_1$ : \_\_ numerical,  $D_2$ : \_ . \_ numerical,  $-D_3$ : \_ \_ numerical,  $-D_1$ :  $\diamond \diamond \diamond \diamond$  analytic  $(7.8 \cdot 10^{-3})$ ,  $D_2$ : ++++ analytic  $(1.2 \cdot 10^{-3})$ ,  $-D_3$ :  $\circ \circ \circ \circ$  analytic  $(6.5 \cdot 10^{-6})$ .

boundary layer. The zero order approximation of the spanwise term is valid only in the viscous sublayer, as it was found for the diffusive destruction rate. A close study of the spanwise transport term shows that  $-(\overline{\theta w_{,y}})_{,y}$  dominates  $D_3$ . Since the Taylor series of  $\epsilon_{\theta 3}$  and  $D_3$  have the same behaviour, it is reasonable to conclude that  $w_{,y}$  can be approximated by a constant only when  $y \leq 0.35$ .

**4.2. Reynolds-flux budget.** Rogers et al. [22], and later Wikström et al. [23], considered  $\psi_i$ , the difference between the pressure scalar-gradient correlation term and the diffusive destruction rate. At Sc = 0.71 and  $Re_{\tau} = 265$ , Wikström et al. found that  $\psi_i$  and the production term are the dominating terms in the transport equation for the streamwise flux. Kawamura et al. [3] obtained the same result at Sc = 0.6 and  $Re_{\tau} = 180$ . The computations of the present study at Sc = 1 show the same behaviour for y > 50, see figure 8c.

At Sc=0.71 and  $Re_{\tau}=265$ , for the streamwise component of the flux-vector, Wikström et~al. also found an approximate balance between pressure scalar-gradient correlation and production except in the near-wall region. This result is in good agreement with the present computations.

When Schmidt number increases, the production term is found to diminuish, and at Sc = 3000, the budget for the transport equation of the streamwise flux is dominated mainly by the diffusive destruction rate and the transport term, see figure 8a.

Figure 8 shows that at a high Schmidt number, the diffusive destruction rate is the dominant term in  $\psi_x$ . Instead,  $\psi_y$  is dominated by the pressure scalar gradient-term, see figure 9a-b. For both the streamwise and the wall-normal flux, the production term decreases when Schmidt number increases and is greater than one. This result is expected because production of turbulence energy is maximum in the buffer layer of the hydrodynamic layer. Moreover  $-\overline{u_i u_k}\Theta_{,k}$  is dominant in the production rate. When the diffusive boundary layer lies entirely in the viscous sublayer, the turbulence energy produced in the buffer layer of the hydrodynamic boundary layer is only partly transmitted to the passive scalar in the near-wall region. As Wikström et al. report it in [23], the present study found that  $\psi_y$  and the production term dominate the budget for the wall-normal flux component. Near the wall, the transport terms and  $\psi_y$  are dominant, see figure 9.

In the spanwise flux budget, the balance is dominated by transport and the diffusive destruction rates at Schmidt number 3000, see figure 10a. Near the wall the destruction rate is positive, instead of being negative, as in the budget for the streamwise flux.

In general, for the three components of the scalar flux-vector, and at Sc = 3000, the transport terms and  $\psi_i$  are found to dominate the budget.

**4.3. Scalar variance-rate budget.** The transport equation for half the scalar variance,  $k_{\theta} = \overline{\theta^2}/2$ , a quantity akin to the turbulent kinetic energy, is obtained by multiplying the transport equation for the scalar fluctuations with the fluctuating scalar  $\theta$ , and then taking the ensemble average of the resulting equation. This yields

$$\frac{Dk_{\theta}}{Dt} = P_{\theta} - \epsilon_{\theta} + D_{k_{\theta}}. \tag{12}$$

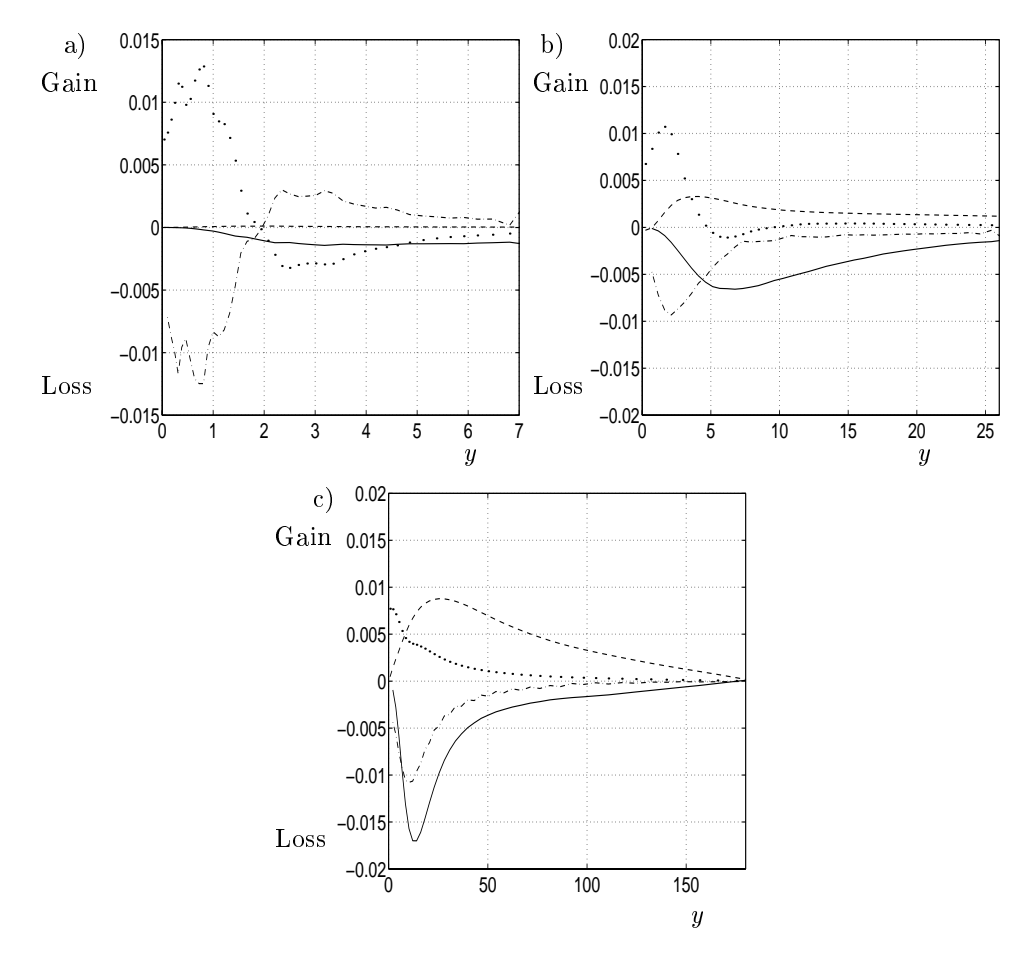


FIGURE 8. Terms in the budget of the streamwise flux  $\overline{u\theta}$ .  $P_{\theta 1}$ : \_\_\_,  $D_1$ : \_\_\_,  $\Pi_{\theta 1}$ : \_\_\_,  $-\epsilon_{\theta 1}$ :  $\cdots$ . a) At Sc=3000. b) At Sc=100. c) At Sc=1.

The terms of the right-hand-side are

$$\begin{split} P_{\theta} &= -\overline{u_i\theta}\Theta_{,i} & \text{production rate,} \\ \epsilon_{\theta} &= \frac{1}{Sc}\overline{(\theta_{,k})^2} & \text{dissipation rate,} \\ D_{k_{\theta}} &= \left(\frac{1}{Sc}k_{\theta,i} - \frac{1}{2}\overline{u_i\theta^2}\right)_{,i} & \text{molecular and turbulent diffusion term.} \end{split}$$

At Sc=0.71 and  $Re_{\tau}=265$ , Wikström et al. [24], and at Sc=1 and  $Re_{\tau}=180$ , Kawamura et al. [2] found that there is an approximate balance between production and dissipation for the scalar variance budget except in the nearwall region. Both the turbulent diffusion and the molecular diffusion terms are negligible except near the wall. At the wall there is a balance between

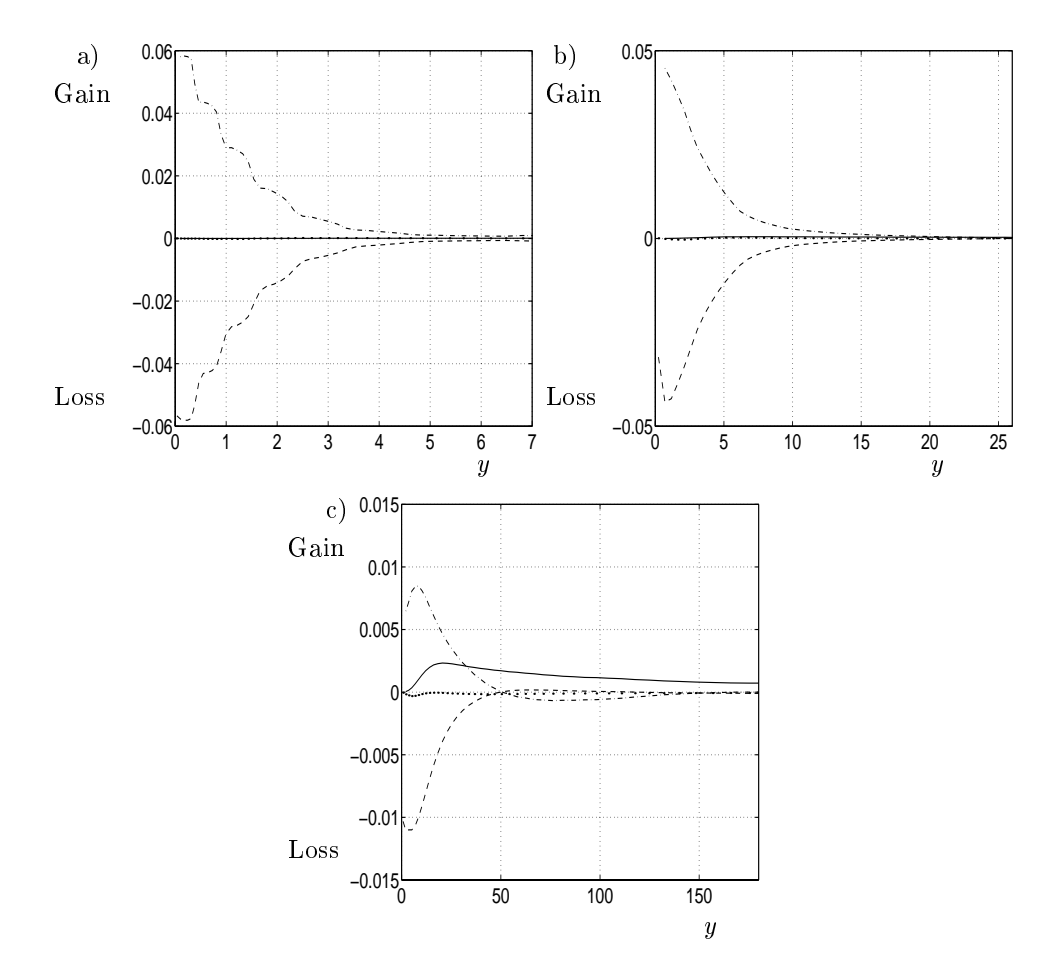


FIGURE 9. Terms in the budget of the wall-normal flux  $\overline{v\theta}$ .  $P_{\theta 2}$ : \_\_\_,  $D_2$ : \_\_\_,  $\Pi_{\theta 2}$ : \_\_\_,  $-\epsilon_{\theta 2}$ :  $\cdots$ . a) At Sc=3000. b) At Sc=100. c) At Sc=1.

molecular diffusion and dissipation. These results are in good agreement with the predictions of the present study at Sc=1, see figure 11c. Here, molecular and turbulent diffusion are compiled in  $D_{k_{\theta}}$ . In the centre of the channel,  $D_{k_{\theta}}$  is not found to be exactly equal to zero. This is due to some lack of convergence of the present statistics. The same defect was obtained at higher Schmidt numbers, see figures 11a and 11b. At high Schmidt number the budget is dominated by the molecular and the diffusion terms, and the production term, see figure 11a. Figure 11 shows that the relative importance of the dissipation rate decreases, and of the diffusion rates increase, when Schmidt number increases.

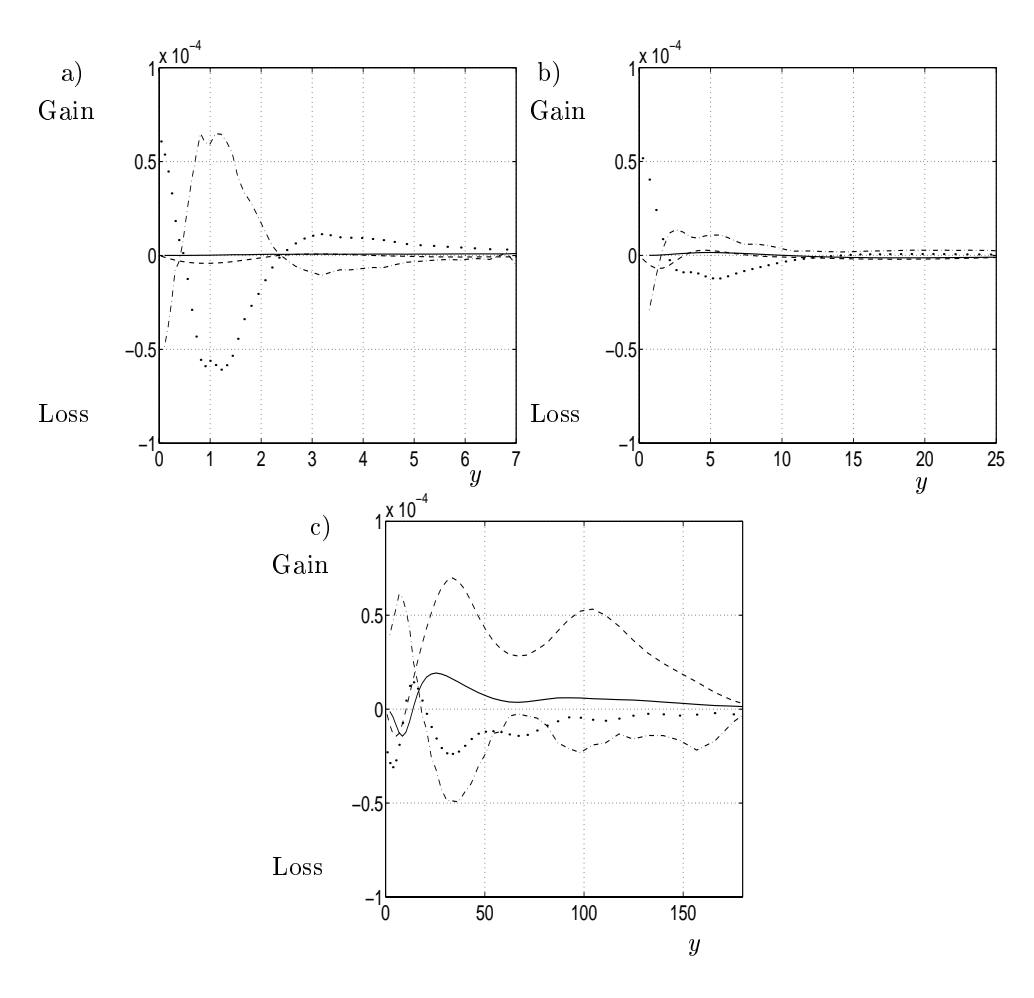


Figure 10. Terms in the budget of the spanwise flux  $\overline{w\theta}$ .  $P_{\theta 3}$ : \_\_\_,  $D_3$ : \_\_\_,  $\Pi_{\theta 3}$ : \_\_\_,  $-\epsilon_{\theta 3}$ :  $\cdots$ . a) At Sc=3000. b) At Sc=100. c) At Sc=1.

**4.4. Scalar dissipation-rate budget.** The transport equation for the scalar dissipation rate  $\epsilon_{\theta} = \frac{1}{Sc}(\theta_{,k})^2$  is

$$\frac{D\epsilon_{\theta}}{Dt} = D_{\epsilon_{\theta}} + P_{\epsilon_{\theta}}^{1} + P_{\epsilon_{\theta}}^{2} + P_{\epsilon_{\theta}}^{3} - Y, \tag{13}$$

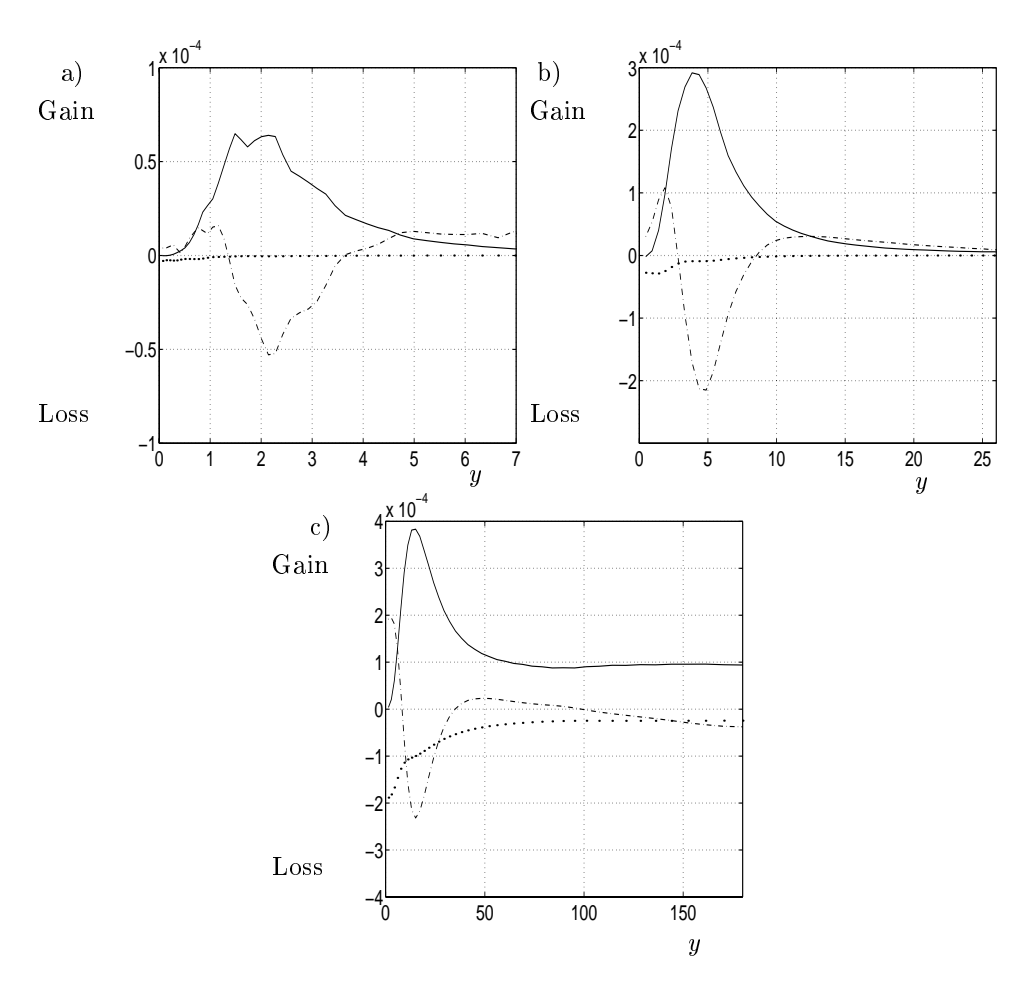


FIGURE 11. Terms in the budget of the scalar variance-rate budget.  $P_{\theta}$ : \_\_,  $D_{k_{\theta}}$ : \_\_,  $-\epsilon_{\theta}$ : ...,  $-\epsilon_{\theta}$ : .... a) At Sc=3000. b) At Sc=100. c) At Sc=1.

where the terms on the right-hand-side of the above equation are

$$\begin{split} D_{\epsilon_{\theta}} &= \left(\frac{1}{Sc}\epsilon_{\theta,k} - \overline{u_k\epsilon_{\theta}'}\right)_{,k} \quad \text{molecular and turbulent diffusion term,} \\ P_{\epsilon_{\theta}}^1 &= -\frac{2}{Sc}\left(\overline{\theta_{,j}\theta_{,k}}U_{j,k} + \overline{u_{j,k}\theta_{,k}}\Theta_j\right) \qquad \qquad \text{production rate,} \\ P_{\epsilon_{\theta}}^2 &= -\frac{2}{Sc}\overline{u_j\theta_{,k}}\Theta_{,kj} \qquad \qquad \text{gradient production term,} \\ P_{\epsilon_{\theta}}^3 &= -\frac{2}{Sc}\overline{u_{j,k}\theta_{,k}\theta_{,j}} \qquad \qquad \text{turbulent production term,} \\ Y &= \frac{2}{Sc^2}\overline{(\theta_{,jk})^2} \qquad \qquad \text{dissipation rate,} \end{split}$$

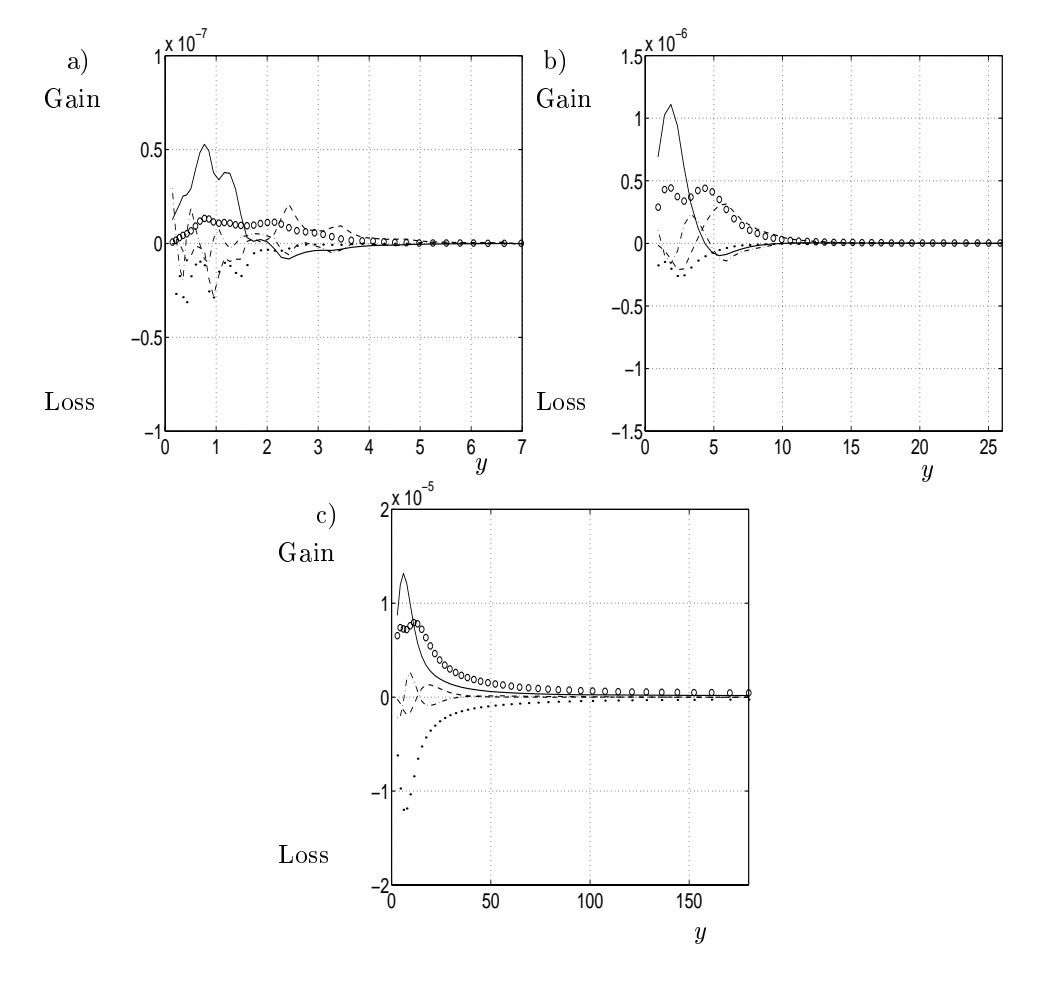


FIGURE 12. Terms in the budget of the scalar dissipation-rate budget.  $P^1_{\epsilon_{\theta}}$ : \_\_\_, Y:  $\cdots$ ,  $P^3_{\epsilon_{\theta}}$ : o o oo,  $D_{\epsilon_{\theta}}$ : \_\_\_,  $P^2_{\epsilon_{\theta}}$ : \_\_\_ a) At Sc = 3000. b) At Sc = 100. c) At Sc = 1.

where  $\epsilon_{\theta}^{'} = \frac{1}{Sc}(\theta_{,k})^2$ . As shown in figure 12, no qualitative changes in the structure of the budget for the dissipation-rate are found when Schmidt number varies. At Schmidt number equal to one, the dissipation rate (Y) and the turbulent production term  $(P_{\epsilon_{\theta}}^3)$ , corresponding to vortex stretching energy [24]) dominate the budget, except in the near-wall region. This result is in good agreement with the scalar dissipation-rate budget found by Wikström et al. [24] at Schmidt number equal to 0.71. In the near-wall region, the production rate  $(P_{\epsilon_{\theta}}^1)$  is significant. At high Schmidt number, the scalar gradient and its derivative are very large. A high order in space is then required for the precision of their derivatives. The obtained wiggles for the diffusion and the dissipation terms in figure 12a are consequently expected, since  $D_{\epsilon_{\theta}}$  and Y contain a second order derivative of the

computed scalar. The present result is nevertheless interesting because it allows a qualitative analysis of the dissipation-rate budget, but one should keep in mind that the accuracy of this result remains to be improved.

#### 5. Conclusions

Large-eddy simulations for turbulent transport of a passive scalar were made at Schmidt numbers equal to 1, 100 and 3000. The purpose of this work was to provide knowledge about the physics of the transport process as input to simplified models for the Reynolds-flux vector at high Schmidt number. The flow Reynolds number was 180. The accuracy of the present computations in the near-wall region was validated by comparisons with analytic expressions in the near-wall-region.

At Schmidt number equal to one, good agreement was found between previous studies and the predictions of the present study. At Schmidt number equal to 3000, the balance in the transport equations of the Reynolds-flux vector is dominated by  $\psi_i$  (the difference between the pressure scalar-gradient term and the diffusive destruction rate) and the transport term  $D_i$ .  $\psi_x$  and  $\psi_z$  are dominated by the diffusive destruction rate and  $\psi_y$  by the pressure scalar-gradient term.

The transport equation for half the scalar variance and the corresponding dissipation were studied. At high Schmidt number the budget is dominated by the molecular and the turbulent diffusion term, and the production term. For transport equation of the scalar dissipation, no qualitative changes in the structure of the budget were found when Schmidt number varies. The dissipation rate and the turbulent production term dominate the budget, except in the nearwall region.

The numerical experiments made in this study showed that several useful simplifications can be made in the near-wall region for the budgets of the Reynolds-flux, the variance and the dissipation rate. They can be summarized as shown below

$$\begin{array}{ll} \frac{D\overline{u_1\theta}}{Dt} & = & -\epsilon_{\theta 1} + D_1, \text{ when } y \leq 2. \\ \\ \frac{D\overline{u_2\theta}}{Dt} & = & \Pi_{\theta 2} + D_2. \\ \\ \frac{D\overline{u_3\theta}}{Dt} & = & -\epsilon_{\theta 3} + D_3. \\ \\ \frac{Dk_{\theta}}{Dt} & = & P_{\theta} + D_{k_{\theta}}. \\ \\ \frac{D\epsilon_{\theta}}{Dt} & = & D_{\epsilon_{\theta}} + P_{\epsilon_{\theta}}^1 + P_{\epsilon_{\theta}}^2 + P_{\epsilon_{\theta}}^3 - Y, \text{ no simplification.} \end{array}$$

#### References

- [1] P.M. Wikström, S. Wallin and A.V. Johansson, Phys. Fluid, 12 (2000) 688.
- [2] H. Kawamura, K. Ohsaka, H. Abe and K. Yamamoto, Int. J. of Heat and Fluid Flow, 19 (1998) 482.
- [3] N. Kawamoto, H. Abe, Y. Matsuo and K. Yamamoto, Proceedings of 11th IHTC, 4 (1998), Kyongju, Korea.
- [4] D.V. Papavassiliou and T.J. Hanratty, Int. J. Heat Mass Transfer 40 (1997) 1303.
- [5] F. Gurniki, S. Zahrai and F.H. Bark,  $3^{rd}$  Symposium on Turbulence, Heat and Mass Transfer, Nagoya, april 2-6 2000, Y.Nagano, K.Hanjalić and T.Tsuji (Editors), ©Aichi Shuppan.
- [6] P.R. Spalart, Direct numerical study of leading edge contamination in fluid dynamics of three-dimensional turbulent shear flows and transition, AGARD-CP-438, (1988), pp.5.1-5.13.
- [7] P.R. Spalart & J.H. Watmuff, J. Fluid Mech., 249 (1993) 337.
- [8] S. Berlin, A. Lundbladh & D.S. Henningson, Phys. Fluids, Vol.2 (1994) No.6, 1949.
- [9] C.S. Lin, R.W. Moulton and G.L. Putnam (1953), Industrial and Engineering Chemistry, Vol.45 No.3, 636
- [10] J.Nordström, N. Nordin and D. Henningson, The fringe technique and the Fourier-method used in the direct numerical simulation of spatially evolving viscous flows, SIAM J. Sci. Comp. 20 (1999), 1365.
- [11] D. Givoli, J. Comp. Phys., 94 (1991) 1.
- [12] S. Zahrai, F.H. Bark and R.I. Karlsson, Eur. J. Mech., B/Fluids, 14 (1995) 459.
- [13] F. Gurniki, S. Zahrai and F.H. Bark, LES of Turbulent Channel Flow of a Binary Electrode, accepted for publication in Journal of Applied Electrochemistry (2000).
- [14] Q. Wang & K.D. Squires, Int. J. Multiphase Flow 22 (1996) 667.
- [15] J. K. Ducowicz and J. D. Ramshaw, J. Comput. Phys. 32 (1979) 71.
- [16] B.J. Daly and M.D. Torrey, SOLA-PTS: A transient, three-dimensional alghorithm for fluid-thermal mixing and wall heat transfer in complex geometries NUREG/CR-3822, LA-10132-MS (1984).
- [17] B.P. Leonard, Comput. Meths. Appl. Mech. Eng. 19 (1979) 59.
- [18] R.M.C. So and T.P. Sommer, Int. J. Heat Mass Transfer, 39/3 (1996) 455.
- [19] F.Gurniki, S.Zahrai and F.Bark, 'Large-eddy simulation of electrochemical mass transfer' 4th Int. Conf. on Hydromagnetic Phenomena and Applications, Sept. 12-18 2000, Giers, France.
- [20] D.V. Papavassiliou and J. Thomas Hanratty, Int. J. Heat Mass Transfer, 40 (1997) 1303.
- [21] V.G. Levich, Physicochemical hydrodynamics Ed. Prentice-Hall (1962) 293.

- [22] M.M. Rogers, N.N. Mansour and W.C. Reynolds, J. Fluid Mech., 203 (1989)
- [23] P.M. Wikström, M. Hallbäck and A.V. Johansson, Int. J. of Heat and Fluid Flow, 19 (1998) 556.
- [24] P.M. Wikström and A.V. Johansson, On the modelling of the transport equation for the passive scalar dissipation rate, 4<sup>th</sup> Int. Symp. on Eng. Turbulence Modelling and Measurements, May 24-26 1999, Corsica, France.

# Paper 6

P6

# ON MODELLING THE REYNOLDS-FLUX VECTOR AT HIGH SCHMIDT NUMBER

#### François Gurniki

Faxén Laboratory, KTH, S-100 44, Stockholm, Sweden

Abstract. Large-eddy simulation (LES) of turbulent passive-scalar transfer in a three-dimensional channel flow was carried out for various Schmidt numbers ranging from 1 to 3000. The turbulent Reynolds number based on the channel half-width was 180. Two explicit algebraic models for the Reynolds-flux vector, validated in previous studies at Schmidt number around unity, are examined. At high Schmidt number, good agreement is found with the predictions of the present study. A wall-function for the mean passive-scalar is proposed on the basis of the simplest tested algebraic model. A new explicit algebraic model for the turbulent flux of the passive scalar is proposed for high Schmidt number. Very good agreement is obtained with the present LES computations at Schmidt numbers equal to 100 and 3000.

#### 1. Introduction

Turbulence in wall-bounded flows with mass transfer has been widely studied during the last decades. Early models are based on zero-order models for velocity field and the assumption of a constant turbulent Schmidt number,  $Sc_t$ , to relate the Reynolds-fluxes,  $\overline{u_i\theta}$ , to the Reynolds stresses,  $\overline{u_iu_j}$ . At a higher order closure-level, two-equation models have been used for the velocity field, while the assumption of a constant  $Sc_t$  is still invoked to model the mass fluxes. Most of these approaches consist of using wall-functions to bridge the gap between the region in which the model is valid and the wall [1]. For simple flows this method was shown to give good results [2, 3]. It appears to be much more difficult to derive wall-functions and models for the Reynolds-flux vector for more complex flows, such as flows at very high Schmidt number.

Algebraic models for the Reynolds-flux vector have been derived by various reseachers [1, 4, 5, 6]. At Schmidt numbers around unity, the transport equation for  $\overline{u_i\theta}$  is reduced to an algebraic equation by assuming that the convective and diffusive transport of the Reynolds-flux vector are proportional to the transport of the turbulent kinetic energy, k, and the variance of the passive scalar,  $\overline{\theta}^2$ . If equilibrium turbulence is assumed, the obtained system of equations for  $\overline{u_i\theta}$  can be linearized.

In a previous study, Gurniki *et al.* [7] used large-eddy simulations in a channel flow with mass transfer at Schmidt number equal to 3000, and a numerical technique to reduce the computational domain for the passive-scalar field to the diffusive boundary layer. This so called fringe region technique had been

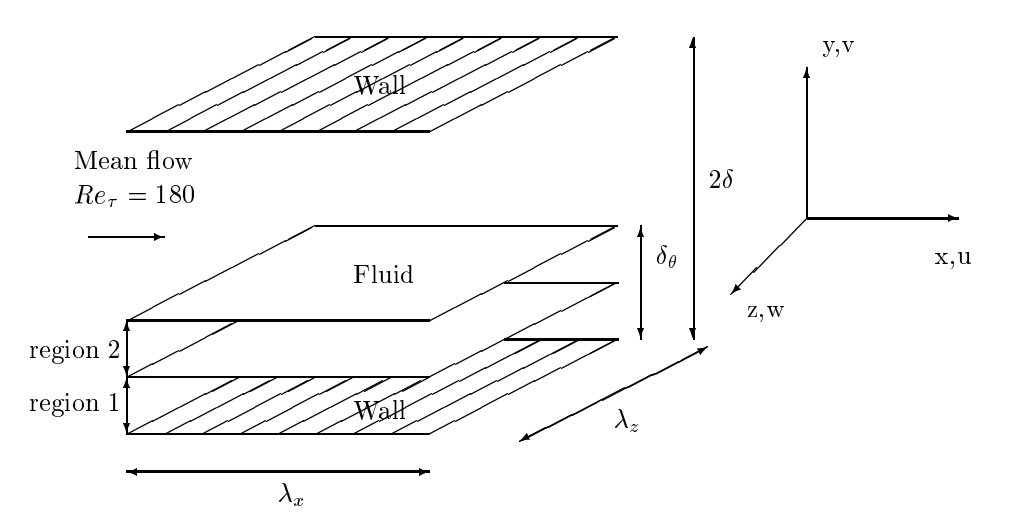


FIGURE 1. The geometry of the channel flow, the three regions of computation, and the chosen coordinate system.

previously used for computations of more difficult flows, like an increasing hydrodynamic boundary layer along a flat plate [8, 9, 10].

The goal of the present work is to test and validate explicit algebraic models for the Reynolds-flux vector at high Schmidt number with the help of LES computations. The paper is organized in the following way: the mathematical problem and the numerical procedure are formulated in section 2. Results from numerical studies are presented in section 3 and conclusions presented in section 4.

#### 2. Theory

In this study, turbulent flow in an infinitely large channel is considered. The walls are assumed to be at a distance of  $2\delta$  (see figure 1) and the flow is driven by a constant pressure gradient, strong enough to make gravitational effects negligible. The coordinate system is chosen so that the walls are located at  $y=\pm\delta$ .

The flow can be described by the Navier-Stokes equations for an incompressible fluid, the continuity equation, and a transport equation for the passive scalar. The equations are nondimensionalized by  $u_{\tau}$ , the friction velocity,  $l^* = \nu/u_{\tau}$ , the length scale in wall units, and  $l^*/u_{\tau}$ , the time scale. The scalar field  $\theta$  can be made dimensionless by using the mean scalar flux at the wall, i.e.  $-\frac{D}{u_{\tau}}\left(\frac{\partial\Theta}{\partial y}\right)_{wall}$ , where  $\Theta$  is the mean value of the dimensional instantaneous scalar, and D the scalar diffusivity.

At very high Schmidt number, the diffusive boundary layer is located very close to the walls. Outside this layer, the distribution of the mean passive-scalar  $\theta$  is almost uniform. It is therefore useless to compute the scalar everywhere

in the channel. For that reason, a method to reduce the mathematical and the numerical domain of investigation to the near-wall region is outlined below. For details, the reader is referred to [10, 11].

The domain, as shown in figure 1, lies between the wall and an imaginary plane surface in the fluid, parallel to the wall and at a distance of  $\delta_{\theta}$  from it.  $\delta_{\theta}$  is sufficiently larger than the diffusive and the logarithmic sublayers for mass, and can be estimated as  $\delta_h/Sc^{1/3}$  [12], where  $\delta_h$  is the thickness of the hydrodynamic boundary layer. Here, since the flow is fully developed,  $\delta_h$  can be approximated as  $\delta^+=180$ , and  $\delta^+_{\theta}=12.5$ . The domain is divided into the conservative region 1 where  $|\nabla\theta^+|\neq 0$ , and region 2 where a source term is added to the scalar conservation-equation to force  $\theta$  to approach a given value. This can be done as follows

$$\frac{\partial \theta^{+}}{\partial t^{+}} + \left(\mathbf{u}^{+} \cdot \nabla^{+}\right) \theta^{+} = \frac{1}{Sc} \nabla^{+,2} \theta^{+} - \lambda^{+} (y^{+}) \cdot (\theta^{+} - \theta_{o}^{+}), \tag{1}$$

where  $\mathbf{u}^+$  and  $\theta^+$  denote the instantaneous velocity and scalar fields, respectively.  $\theta_o^+$  is a constant, and Sc is Schmidt number. Equation (1) can be used for both regions by choosing properly the function  $\lambda^+$ , as shown in figure 2. The slope of the ramp function  $\lambda^+$  is here taken equal to 0.13 in wall-units. The source term works as a forcing function, imposing to the intantaneous scalar the fixed value of  $\theta_o^+$  in region 2. Throughout the remainder of this paper, the domain containing only regions 1 and 2 will be called the reduced domain. The height of region 1 is around the two thirds of  $\delta_\theta^+$ .

The fringe technique is here used in order to be able to formulate a boundary condition in region 2 for the instantaneous scalar at the edge of the diffusive boundary layer. It annihilates with the help of a source term the fluctuating part of the passive scalar in the vicinity of the boundary of the reduced domain. It is bluntly assumed that the non-physical phenomena occuring in the fringe region do not invalidate the solution in the remaining part of the computational domain [13] (region 1 in figures 1 and 2). This assumption has been verified by numerical experiments in [11]. Hereforth, all variables are nondimensionalized in wall-units. The '+' supersripts are therefore dropped for notational simplicity. As a first step, in order to make comparisons with earlier numerical and experimental investigations, the case of a scalar set constant at the wall is considered. The other boundary is set in the fluid at the limit of region 2, with a mixed condition

$$\frac{\partial \theta}{\partial y}(x, \delta_{\theta}, z, t) = \theta(x, \delta_{\theta}, z, t) - \theta_{o}. \tag{2}$$

Equation (2) is a non-reflecting boundary condition. It guarantees that error waves travelling from the wall to the centre of the channel are damped, and are not reflected towards the wall [14]. Note that the source term in equation (1) forces  $\theta$  to approach  $\theta_o$  in the fringe region.

For the hydrodynamical equations, a no-slip condition is used at the walls. The velocity field is always computed in a computational domain that contains

Table 1. Specifications of the meshes.

	$N_x$	$N_y$	$N_z$	$\Delta x$	$\Delta z$	$\Delta y_{min}$	$\Delta y_{max}$
$Mesh \ 1 \times 1 \times 1$	32	42	96	70.7	11.8	1.41	18.9
$Mesh 1 \times 6 \times 1$	32	54	96	70.7	11.8	0.03	0.42

both walls of the turbulent channel, and whose width in dimensional units is  $2\delta$ , see figure 1.

In this large-eddy simulation, averaging over the volume of the computational cells is used as the filtering function. The SGS model is here an anisotropic version of the Smagorinsky model, and has been validated in a previous work [15]. The scalar transport equation is filtered at each cell M with the same methodology as for the velocity. For more detailed information the interested reader is referred to Gurniki  $et\ al.$  [16].

The computational domain is periodic in the streamwise and the spanwise directions with corresponding periodicity lengths,  $\lambda_x$  and  $\lambda_z$ . The distance between the channel walls is  $2Re_{\tau}$  in wall-units.  $\lambda_x$  and  $\lambda_z$  are respectively  $4 \times \pi \times Re_{\tau}$ and  $2 \times \pi \times Re_{\tau}$  in wall-units, see figure 1. Periodic boundary conditions are applied for the velocity, the fluctuations of pressure and the passive scalar, in the streamwise and spanwise directions. As a feature of this study, the use of different mesh systems for the fluid velocity field and the scalar field should be pointed out. Table 1 shows the characteristics of two meshes. The first mesh, denoted as Mesh  $1 \times 1 \times 1$ , has a computational domain extended from a wall to the other and considers the whole cross-section of the channel flow. It is used to compute the fluid velocity field and the mass transfer at Sc = 1. The mesh used to compute the passive scalar at higher Schmidt numbers is denoted as Mesh  $1 \times 6 \times 1$ , and is limited to regions 1 and 2 in figures 1 and 2. The grids are uniform in the mean flow direction, and are stretched in the direction normal to the wall, with the finest spacing at the walls. The turbulent velocity and the scalar are computed successively in the following way: the Navier-Stokes equation is advanced one step in time, and then the fluid velocity field and the eddy diffusivity are interpolated onto the mesh system used for the scalar field. With the known velocity field, the volume average scalar transport-equation is solved. This procedure is repeated by returning to the first step and computation for the next time step.

A fourth order Lagrangian interpolation scheme is used to ensure a sufficient accuracy in interpolation of turbulent velocity field, see e.g. Wang & Squires [17]. The filtered scalar transport-equation is integrated using a three step, third order tensor viscosity scheme, [18, 19]. The advection term in the right hand side of the filtered equation was approximated with QUICK scheme [20] to keep a second order spatial accuracy and a numerical stability at the same time. The diffusion term was discretized using a central differentiation.

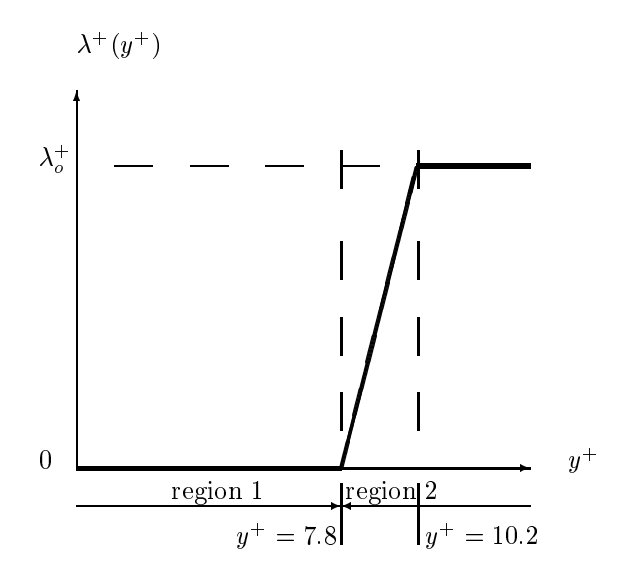


Figure 2. The  $\lambda$  function versus the wall-normal direction.

The initial profile in a cross section for the velocity was set parabolic. The passive scalar calculation was not added until the hydrodynamic simulation had reached statistically equilibrium state. The initial profile in a cross section for the scalar was set linear at Sc=1, and was set proportional to  $y^{-1/5}$  for the calculations made at Sc=100. It was set identical to the profile obtained at Sc=100 for the calculations made at Sc=3000. The calculated variables were considered to be at equilibrium when variation of the statistical properties in time was small.

#### 3. Results

In this section results from large eddy-simulations for turbulent transport of a passive scalar are presented at Schmidt numbers (Sc) equal to 1, 100 and 3000. The flow Reynolds number is 180. At Schmidt number equal to 3000, the present work examines two explicit algebraic models for the Reynolds-flux vector validated in previous studies at Sc = 0.71 and 1 [21, 22]. A theoretical profile for the mean passive-scalar is derived on the basis of one of these models. The present study tests also a new explicit algebraic model derived on the basis of a simplification in the budget of the Reynolds-flux vector as in [7].

Kawamura et al. [23] studied the asymptotic behaviour of the nondimensional ratio r of the thermal time-scale,  $\frac{\overline{\theta^2}}{2\epsilon_{\theta}}$ , and the dynamical time-scale,  $\frac{k}{\epsilon}$ , where  $\epsilon_{\theta}$  is the dissipation term of temperature variance. r is an important parameter, since it is part of many algebraic models for the Reynolds-flux vector. The study of its magnitude is also of importance because it gives an estimation of the relative importance of the two time-scales. Kawamura et al. showed that r tends

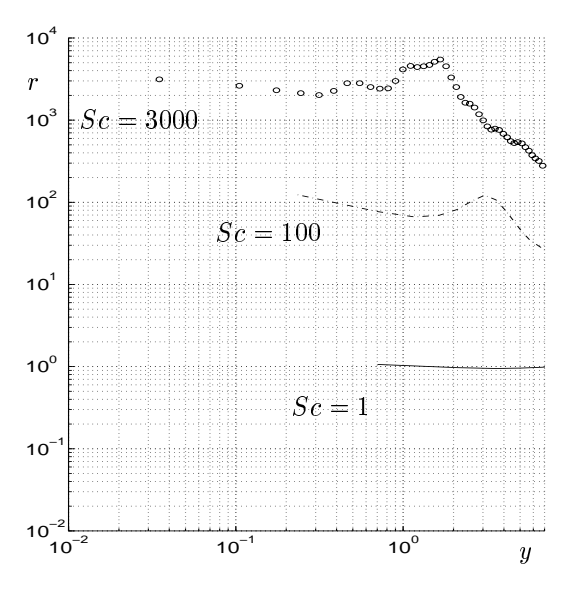


Figure 3. At Sc=3000, the time-scale ratio r along the wall-normal direction.

exactly to Sc as the wall is approached. The present LES agree with this theoretical result, as shown in figure 3, for Schmidt number equal to 1, 100 and 3000. These three computations of both dynamical and heat fundamental statistical quantities, indicate that the present code reproduces correctly the physics in the near-wall region. As shown in figure 3, it is not possible to consider r constant in this region.

At Sc = 0.71 and for a two-dimensional flow around a cylinder, Wikström et al. [6] reported a model for the Reynolds-flux vector. It is a truncation of the more general expression developed by Shih et al. [24] with the help of dimensional analysis and invariant theory. The scalar-flux can be described as following

$$\overline{u_i \theta} = a_v \cdot k \cdot \tau \Theta_{,i} + \frac{k^2}{\epsilon} \tau \left( a_2 U_{i,j} + a_3 U_{j,i} \right) \Theta_{,j}, \tag{3}$$

where  $\tau$  is a turbulent time-scale. Wikström et~al. found that the Reynolds-flux vector was best captured using a mixed time-scale between the dynamical and the heat time-scale,  $\tau = \sqrt{\frac{k\bar{\theta}^2}{2\epsilon\epsilon_{\theta}}}$ . For the channel flow at Sc=1, 100 and 3000 the present study found that the wall-normal component was correctly predicted by equation (3), when the streamwise component was not. A modified model, correcting the above equation with damping functions in the near-wall region, was developed by So et~al. [1] for fully developed channel flows, and Schmidt number around unity. Fairly good results were obtained at Sc=3000 with this model, as shown in figure 4. The Reynolds-flux vector was here modelled as

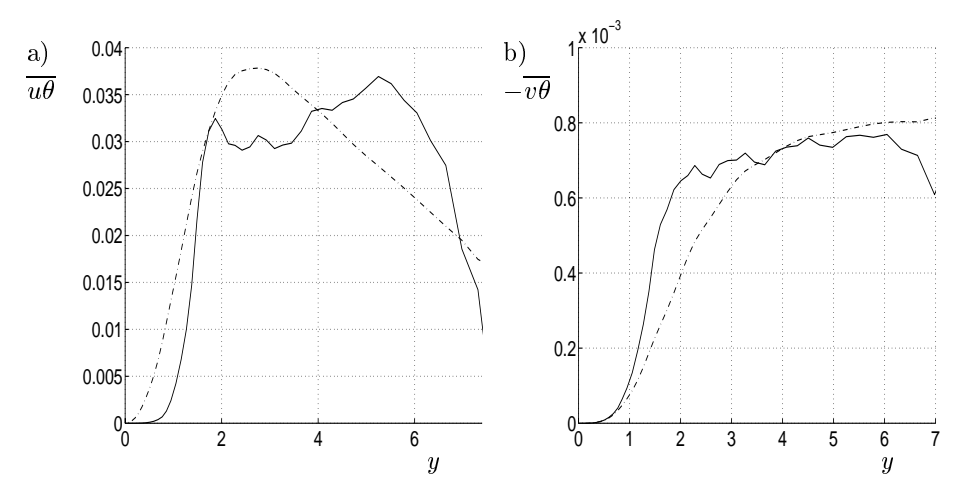


FIGURE 4. At Sc = 3000, model for  $\overline{u_i\theta}$  proposed by So *et al.* [1]. Solid line:  $\overline{u_i\theta}^{\mathrm{model}}$  computed with the mixed time-scale. Dashed line:  $\overline{u_i\theta}^{\mathrm{LES}}$ . a)  $u_i = u_1 = u$ . b)  $u_i = u_2 = v$ .

follows

$$-\overline{u_i\theta} = \alpha_t \frac{\partial \Theta}{\partial x_i} - \frac{\tau}{c_{T1}} \times \left\{ [2\nu_t + (1 - c_{T2})\alpha_t] S_{ik} + (1 - c_{T2})\alpha_t \Omega_{ik} \right\} \frac{\partial \Theta}{\partial x_k} ,$$

$$\nu_t = c_{T3} \frac{k^2}{\epsilon} \left( 1 + \frac{3.45}{\sqrt{Re_t}} \right) \tanh\left(\frac{y}{9}\right) , \qquad (4)$$

$$\alpha_t = c_\lambda \cdot k \cdot \tau \left[ \left( 1 - \left( 1 - e^{-\frac{y}{A}} \right)^2 \right) \frac{c_{\lambda 1}}{Re_t^{1/4}} + \left( 1 - e^{-\frac{y}{A}} \right)^2 \right] .$$

where  $S_{ik}$  is here the mean strain rate,  $\Omega_{ik}$  the mean rotation rate,  $c_{T1}(Sc=3000)=3.28$ ,  $c_{T2}(Sc=3000)=0.4$ ,  $c_{T3}(Sc=3000)=-4.5\times10^{-3}$ ,  $c_{\lambda}(Sc=3000)=-9.5\times10^{-5}$ ,  $c_{\lambda 1}(Sc=3000)=0.3$ , A(Sc=3000)=3 and  $a_v(Sc=3000)=0.0017=-a_{\theta}$ .  $Re_t=\frac{k^2}{\epsilon}$ . Note the simplicity of the model for the Reynolds flux in equation (3) in the wall-normal direction, which is usually found to be easier to model than the streamwise component [1].

At lower Schmidt numbers, Sc = 1 and 100, equation (3) does not give acceptably accurate results for the wall-normal component of the Reynolds-flux vector, because it drastically underpredicts the flux at the center of the channel. Noting that model (3) was tested for a cylinder wake, this result is expected since only the wall-normal component of the fluctuating velocity in the near-wall regions of a channel flow has similar structure with the wall-normal fluctuating velocity close to the axis of symmetry of a two-dimensional cylinder wake.

Equation (3) is constituted by the first two terms of a constitutive relation developed by Shih *et al.* [24]. The present study considered also the complete

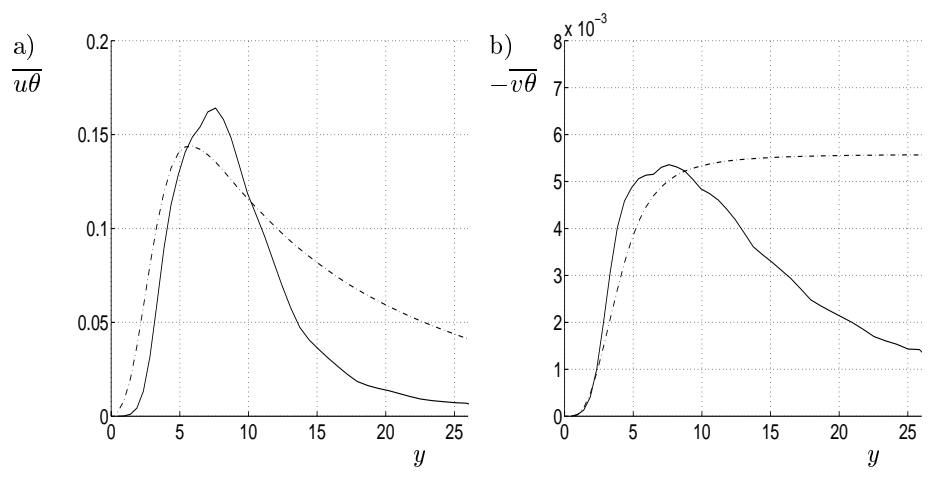


FIGURE 5. At Sc=100, model for  $\overline{u_i\theta}$  proposed by So et~al. [1]. Solid line:  $\overline{u_i\theta}^{\mathrm{model}}$  computed with the mixed time-scale. Dashed line:  $\overline{u_i\theta}^{\mathrm{LES}}$ . a)  $u_i=u_1=u$ . b)  $u_i=u_2=v$ .

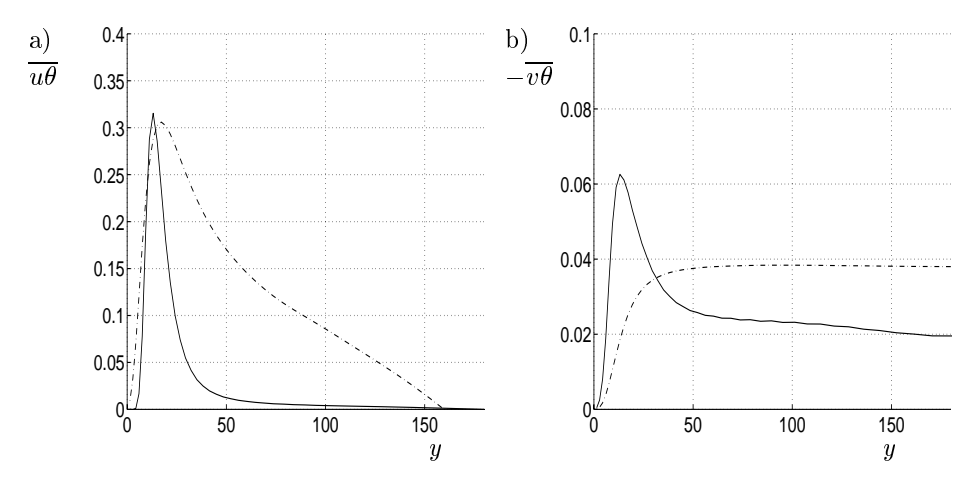


Figure 6. At Sc=1, model for  $\overline{u_i\theta}$  proposed by So et~al. [1]. Solid line:  $\overline{u_i\theta}^{\mathrm{model}}$  computed with the mixed time-scale. Dashed line:  $\overline{u_i\theta}^{\mathrm{LES}}$ . a)  $u_i=u_1=u$ . b)  $u_i=u_2=v$ .

relation for the streamwise component of the Reynolds-flux vector. No improvement was obtained.

At Schmidt number equal to 1 and 100, the model developed by So et al. [1] gives reasonable results for  $\overline{u\theta}$ , but quite poor for  $\overline{v\theta}$ , see figures 5 and 6. So et al. validated the model by setting a constant passive-scalar-flux at the walls. With these boundary conditions, the y-component of the Reynolds-flux vector must be zero at the centre of the channel. The damping function of the thermal

diffusivity  $\alpha_t$  of equation (4) has been calibrated according to these boundary conditions.

Wikström et al. [22] derived an algebraic relation for the Reynolds-flux vector, and the performance of the model was investigated in a homogeneous shear flow, a channel flow and a heated cylinder wake. Very good predictions were found in all cases. For the channel flow, the considered turbulent Reynolds and Schmidt numbers were equal to 265 and 0.71, respectively. The model can be described as following

$$\frac{\overline{u_i\theta}}{\sqrt{kk_{\theta}}} = -(1 - c_{\theta 4})A_{ij}^{-1} \frac{\overline{u_j u_l}}{k} \Theta_{,l}, \tag{5}$$

where the inverse of the matrix  $\mathbf{A}$  is given by

$$\mathbf{A}^{-1} = \frac{(G^2 - \frac{1}{2}Q_1)\mathbf{I} - G(c_S\mathbf{S} + c_\Omega\Omega) + (c_S\mathbf{S} + c_\Omega\Omega)^2}{G^3 - \frac{1}{2}GQ_1 + \frac{1}{2}Q_2},\tag{6}$$

and  $c_S = 1 - c_{\theta 2} - c_{\theta 3}$ ,  $c_{\Omega} = 1 - c_{\theta 2} + c_{\theta 3}$ ,  $S_{ij} = \frac{1}{2} \frac{k}{\epsilon} \left( \frac{\partial U_i}{\partial x_j} + \frac{\partial U_j}{\partial x_i} \right)$  and  $\Omega_{ij} = \frac{1}{2} \frac{k}{\epsilon} \left( \frac{\partial U_i}{\partial x_j} - \frac{\partial U_j}{\partial x_i} \right)$ .

In the case of a fully developed flow in a channel, equations (5) and (6) become

$$\begin{split} \overline{u\theta} &= \sqrt{kk_{\theta}} c_{\theta 4} \frac{\partial \Theta}{\partial y} \left[ A_{11}^{-1} \frac{\overline{uv}}{k} + A_{12}^{-1} \frac{\overline{v^2}}{k} \right] \quad , \\ \overline{v\theta} &= \sqrt{kk_{\theta}} c_{\theta 4} \frac{\partial \Theta}{\partial y} \left[ A_{21}^{-1} \frac{\overline{uv}}{k} + A_{22}^{-1} \frac{\overline{v^2}}{k} \right] \quad , \\ A_{11}^{-1} &= \frac{1}{G} + \frac{k^2}{4\epsilon^2} (U_{,y})^2 \frac{(c_S^2 - c_{\Omega}^2 - 2c_S c_{\Omega})}{G^3 - \frac{1}{2} G Q_1} \quad , \\ A_{12}^{-1} &= -\frac{k}{2\epsilon} U_{,y} \frac{(c_S + c_{\Omega})}{G^2 - \frac{1}{2} Q_1} \quad , \\ A_{21}^{-1} &= -\frac{k}{2\epsilon} U_{,y} \frac{(c_S - c_{\Omega})}{G^2 - \frac{1}{2} Q_1} \quad , \\ A_{22}^{-1} &= \frac{1}{G} + \frac{k^2}{4\epsilon^2} (U_{,y})^2 \frac{(c_S^2 - c_{\Omega}^2 + 2c_S c_{\Omega})}{G^3 - \frac{1}{2} G Q_1} \quad , \end{split}$$

where  $G = \frac{1}{2} \left( 2c_{\theta 1} - 1 - \frac{1}{r} + \frac{P_k}{\epsilon} \right)$ ,  $P_k = -\overline{uv} \frac{\partial U}{\partial y}$ ,  $Q_1 = \frac{k^2}{2\epsilon^2} (U_{,y})^2 (c_S^2 - c_\Omega^2)$ ,  $c_{\theta 1} = 1.6(1+1/r)$  and  $Q_2 = 0$ . As shown in figures 7 and 9, good agreement is found between this model and the present computations, at Sc = 1 and 3000, but the wall-normal Reynolds-flux is underpredicted in the logarithmic region of the diffusive boundary layer at Sc = 100. This result can be explained by the values chosen for the constants  $c_{\theta 2}$  and  $c_{\theta 3}$  in the present study, that account for the effect of the rapid pressure in  $\psi_i$  (see equation (10)). The effect is not well understood and Wikström et al. took these constants equal to zero in order

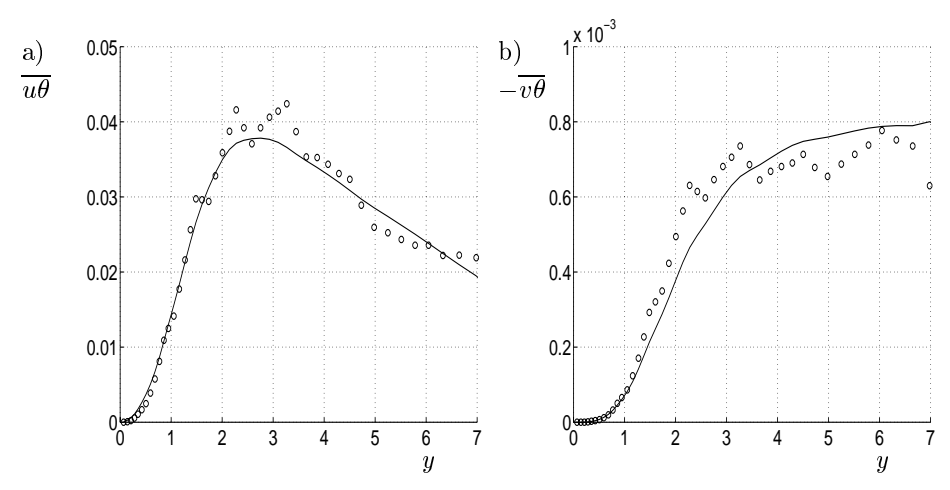


FIGURE 7. At Sc=3000, the mean Reynolds-flux vector along the wall-normal distance. Model proposed by Wikström et~al.~[22]. Solid line:  $\overline{u_i\theta}^{\rm LES}$ .  $\circ\circ\circ\circ:\overline{u_i\theta}^{\rm model}$ . a) i=1, streamwise direction.  $c_{\theta 1}=3.2,~c_{\theta 2}=1,~c_{\theta 3}=0.5$  and  $c_{\theta 4}=4.0\times10^2$ . b) i=2, wall-normal direction.  $c_{\theta 1}=3.2,~c_{\theta 2}=1,~c_{\theta 3}=0.5$  and  $c_{\theta 4}=2.0\times10^1$ .

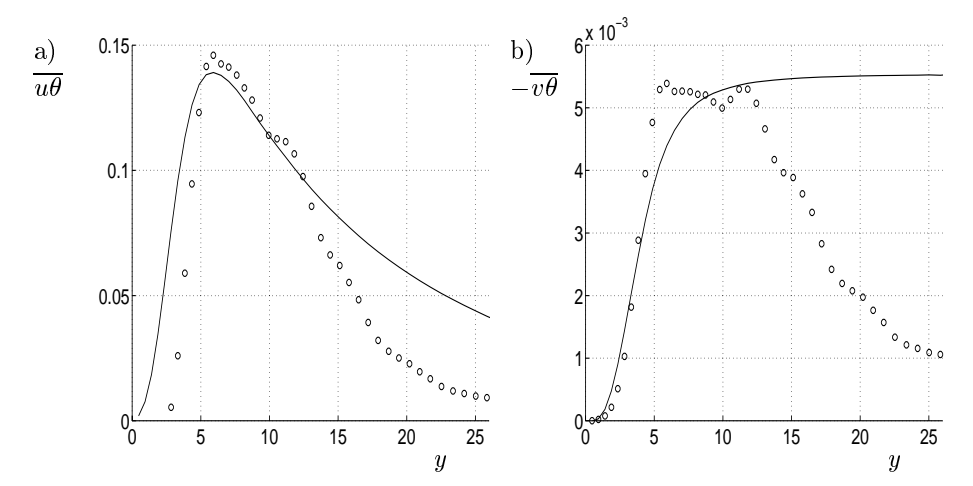


FIGURE 8. At Sc=100, the mean Reynolds-flux vector along the wall-normal distance. Model proposed by Wikström et~al.~[22]. Solid line:  $\overline{u_i\theta}^{\rm LES}$ .  $\circ \circ \circ \circ : \overline{u_i\theta}^{\rm model}$ . a) i=1, streamwise direction.  $c_{\theta 1}=3.2,~c_{\theta 2}=0.05,~c_{\theta 3}=0.05$  and  $c_{\theta 4}=4\times 10^2$ . b) i=2, wall-normal direction.  $c_{\theta 1}=3.2,~c_{\theta 2}=0.05,~c_{\theta 3}=0.05$  and  $c_{\theta 4}=2.0\times 10^1$ .

to eliminate their contribution. At higher Schmidt number than unity, the zero values for  $c_{\theta 2}$  and  $c_{\theta 3}$  produce results in less agreement than in figure 8.

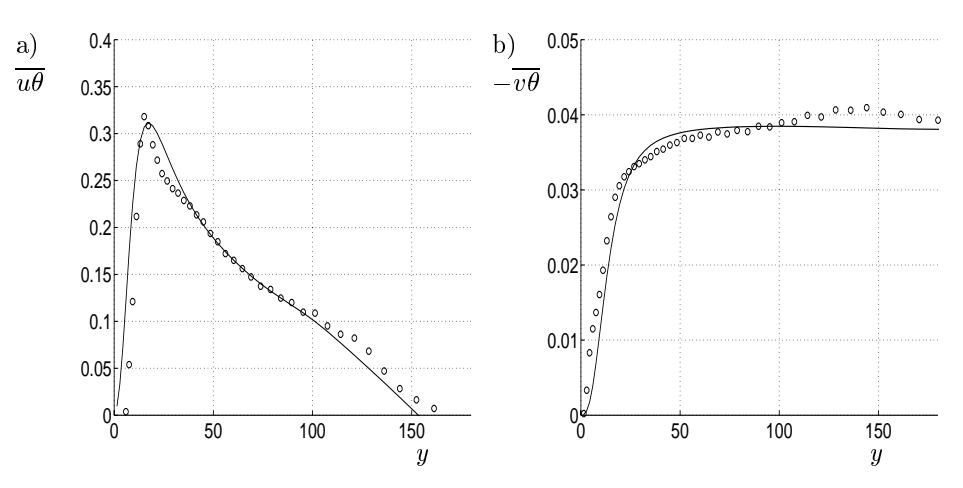


FIGURE 9. At Sc=1, the mean Reynolds-flux vector along the wall-normal distance. Model proposed by Wikström et al. [22]. Solid line:  $\overline{u_i\theta}^{\mathrm{LES}}$ .  $\circ \circ \circ \circ : \overline{u_i\theta}^{\mathrm{model}}$ . a) i=1, streamwise direction.  $c_{\theta 1}=3.2$ ,  $c_{\theta 2}=0.5$ ,  $c_{\theta 3}=0.5$  and  $c_{\theta 4}=1.5\times 10^4$ . b) i=2, wall-normal direction.  $c_{\theta 1}=3.2$ ,  $c_{\theta 2}=0.5$ ,  $c_{\theta 3}=0.5$  and  $c_{\theta 4}=8.5\times 10^2$ .

The improvement of prediction for the Reynolds-flux vector is very good compared with the predictions of the previous model.  $c_{\theta 4}$  could not be found identical for the two components of the Reynolds-flux vector.

In analogy with the transport equations for the Reynolds stresses, a transport equation of the scalar-flux vector can be written in symbolic form as

$$\frac{D\overline{u_i\theta}}{Dt} = P_{\theta i} + \prod_{\theta i} -\epsilon_{\theta i} + D_i = P_{\theta i} + \psi_i + D_i, \tag{7}$$

where  $D/Dt = \partial/\partial t + U_l\partial/\partial x_l$ , and the terms on the right-hand-side of the above equation are identified as follows

$$P_{\theta i} = -\left[\overline{u_i u_l} \Theta_{,l} + \overline{u_l \theta} U_{i,l}\right] \qquad \text{production rate,}$$
 
$$\prod_{\theta i} = \overline{p \theta_{,i}} \qquad \text{pressure scalar-gradient term,}$$
 
$$\epsilon_{\theta i} = \left(1 + \frac{1}{Sc}\right) \overline{\theta_{,l} u_{i,l}} \qquad \text{viscous diffusion rate,}$$
 
$$D_i = -\left(\overline{u_i u_l \theta} + \overline{p \theta \delta_{il}} - \frac{1}{Sc} \overline{u_i \theta_{,l}} - \overline{\theta u_{i,l}}\right)_l \qquad \text{turbulent transport term.}$$

At high Schmidt number in the near-wall region, Gurniki *et al.* [7] showed that the budget for the Reynolds-flux vector (7) can by simplified by neglecting the production rate. Assuming equilibrium for the flow, equation (7) becomes

$$\psi_i + D_i = 0 \tag{8}$$

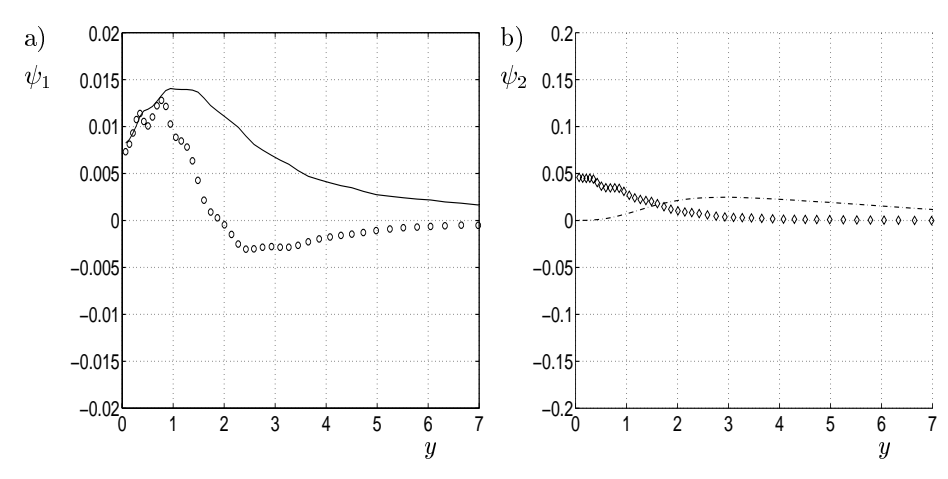


FIGURE 10. At Sc=3000,  $\psi_i$  along the wall-normal distance. Model proposed by Wikström *et al.* [22].  $c_{\theta 1}=3.8$ ,  $c_{\theta 2}=-3.5$ ,  $c_{\theta 3}=-0.65$ ,  $c_{\theta 4}=15$ . a) Solid line:  $\psi_1^{\rm model}$ .  $\circ \circ \circ : \psi_1^{\rm LES}$ . b) Model prediction of  $\psi_2$ . Dashed line:  $\psi_2^{\rm model}$ .  $\diamond \diamond \diamond : \psi_2^{\rm LES}$ .

This equation will be used below as the basis of an algebraic model for the Reynolds-flux vector.

Wikström et al. [22] validated a model for the difference of the pressure scalar-gradient term,  $\prod_{\theta i}$ , and the viscous diffusion rate,  $\epsilon_{\theta i}$ 

$$\psi_i = \overline{p\theta_{,i}} - \left(1 + \frac{1}{Sc}\right)\overline{\theta_{,k}u_{i,k}} = \prod_{\theta_i} -\epsilon_{\theta_i}.$$
 (9)

A linear model was considered, but a more performant version including a non-linear term was chosen. For simplicity, only the linear has been used here. The model term reads as

$$\psi_i = -c_{\theta 1} \frac{1}{\tau} \overline{u_i \theta} + c_{\theta 2} \overline{u_l \theta} U_{i,l} + c_{\theta 3} \overline{u_l \theta} U_{l,i} + c_{\theta 4} \overline{u_i u_l} \Theta_{,l}, \tag{10}$$

where  $c_{\theta i}$  have been considered constants and tested with different values for a 2D and a 3D geometry (a heated cylinder and a channel flow).  $\tau$  is the mixed time-scale used in the previous chapter.

Figure 10 compares the above model with the present LES computations. The agreement is not excellent, but better than the one reported by Wikström et al. [22]. They explained this discrepancy by the linearity of model (10) for  $\psi_i$ , when the physical phenomena in the near-wall region are non-linear. Before solving equation (8) for  $\overline{u_i\theta}$ , that states  $\psi_i + D_i = 0$ , one must provide a model for the turbulent transport term  $D_i$ . As shown in figure 11,  $-\left(-\overline{u_{i,y}\theta}\right)_{,y}$  is the dominant term in  $D_i$  in the streamwise and the wall-normal direction. As the first step in the development of a new model for the Reynolds-flux vector, a model for  $D_i$  based on equation (4) is considered. Deriving this equation in the wall-normal direction,  $\overline{u_{i,y}\theta}$  can be identified as the terms of  $(\overline{u_i\theta})_{,y}$  that do not

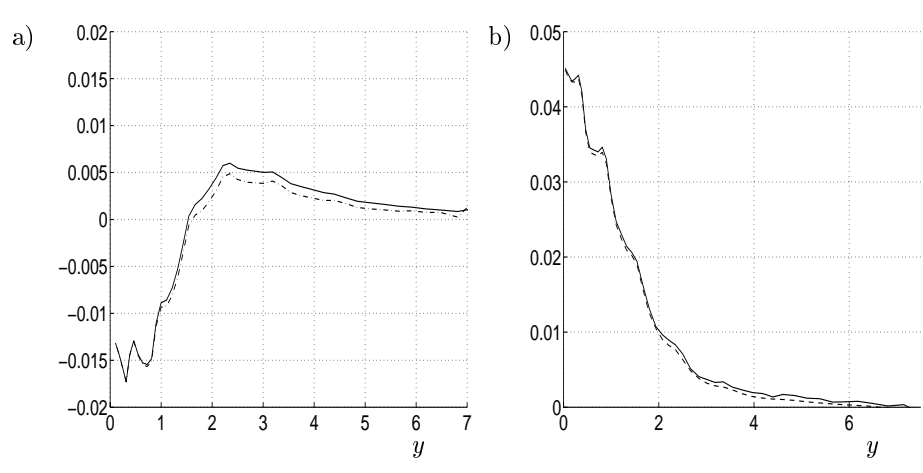


FIGURE 11. At Sc=3000, The turbulent transport term  $D_i$  in the budget. a) For the streamwise flux. Dashed line:  $-\left(\overline{uv\theta}-\frac{1}{Sc}\overline{u\theta_{,y}}-\overline{\theta u_{,y}}\right)_{,y}$ . Solid line:  $-\left(-\overline{\theta u_{,y}}\right)_{,y}$ . b) For the wall-normal flux. Dashed line:  $-\left(\overline{v^2\theta}+\overline{p\theta}-\frac{1}{Sc}\overline{v\theta_{,y}}-\overline{\theta v_{,y}}\right)_{,y}$ . Solid line:  $-\left(-\overline{\theta v_{,y}}\right)_{,y}$ .

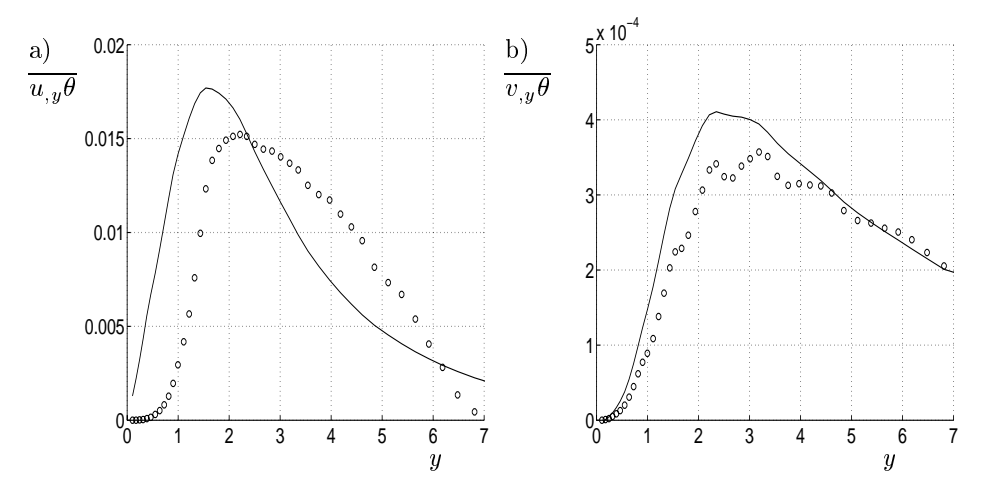


Figure 12. At Sc=3000, model proposed by the present study for  $\overline{u_{i,y}\theta}$ . Solid line:  $\overline{u_{i,y}\theta}^{\mathrm{LES}}$ .  $\circ \circ \circ : \overline{u_{i,y}\theta}^{\mathrm{model}}$ . a) i=1. b) i=2.

depend on the second derivative for the mean passive-scalar. Here, it is assumed that  $\overline{u_i\theta_{,y}}$  are proportional to  $\frac{d^2\Theta}{dy^2}$ .  $\overline{u_{i,y}\theta}$  can then be modelled as follows

$$-\overline{u_{i,y}\theta} = \alpha_t' \frac{\partial \Theta}{\partial x_i} - \frac{\tau'}{c_{T1}} \left\{ [2\nu_t + (1 - c_{T2})\alpha_t] S_{ik} + (1 - c_{T2})\alpha_t \Omega_{ik} \right\} \frac{\partial \Theta}{\partial x_k}$$

$$- \frac{\tau}{c_{T1}} \left\{ [2\nu_t + (1 - c_{T2})\alpha_t] S_{ik} + (1 - c_{T2})\alpha_t \Omega_{ik} \right\}' \frac{\partial \Theta}{\partial x_k}. \tag{11}$$

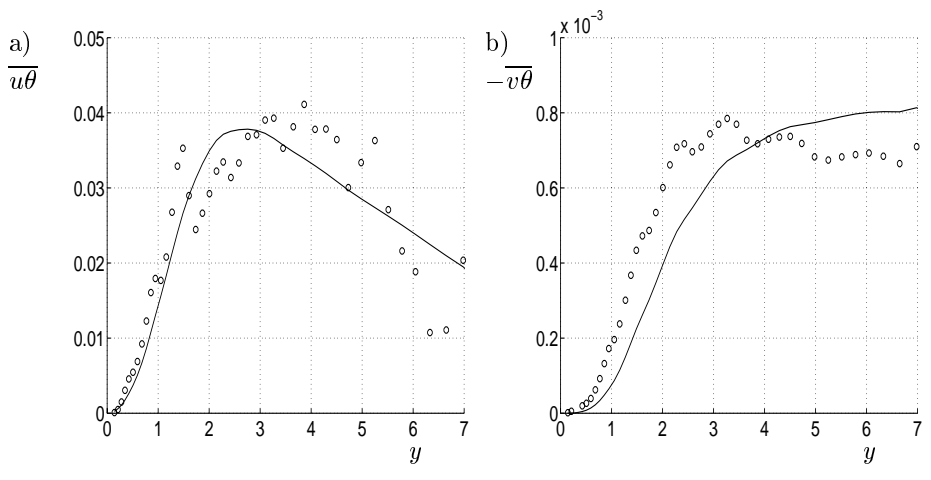


FIGURE 13. At Sc = 3000, model proposed by the present study for  $\overline{u_i\theta}$ . Solid line:  $\overline{u_i\theta}^{\rm LES}$ .  $\circ \circ \circ$ :  $\overline{u_i\theta}^{\rm model}$ . a) i = 1,  $c_{\theta 1} = 3.8$ ,  $c_{\theta 2} = -3.5$ ,  $c_{\theta 3} = -0.65$ ,  $c_{\theta 4} = 15$  and  $c_{\theta 5} = 7$ . b) i = 2,  $c_{\theta 1} = 3.8$ ,  $c_{\theta 2} = -3.5$ ,  $c_{\theta 3} = -0.65$ ,  $c_{\theta 4} = 15$  and  $c_{\theta 6} = 0.21$ .

The superscript ' is equivalent to the first derivative in the wall-normal direction. Good agreement was obtained between the present LES computations and this model, see figure 12. The wall-normal component was slightly better predicted. Equations (10) and (11) are then inserted in (8). The obtained equation system for the Reynolds-flux vector is linear and can be described as following

$$\begin{bmatrix} \frac{-c_{\theta 1}}{\tau} & c_{\theta 2} \cdot U' \\ c_{\theta 3} \cdot U' & \frac{-c_{\theta 1}}{\tau} \end{bmatrix} \begin{bmatrix} \overline{u\theta} \\ \overline{v\theta} \end{bmatrix} = \begin{bmatrix} -(\overline{u}, \underline{y}\theta)' - c_{\theta 4}\overline{uv} \cdot \Theta' \\ -(\overline{v}, \underline{y}\theta)' - c_{\theta 4}\overline{v^2} \cdot \Theta' \end{bmatrix}$$
(12)

The solution of equation (12) is straightforward

$$\begin{cases} \overline{u\theta} = \frac{-c_{\theta 5}}{\tau^2 c_{\theta 2} c_{\theta 3} (U')^2 - c_{\theta 1}^2} \times \\ \left[ c_{\theta 1} \tau \left( \frac{d}{dy} (\overline{u}_{,y} \overline{\theta}) + c_{\theta 4} \overline{u} \overline{v} \cdot \Theta' \right) + c_{\theta 2} \tau^2 U' \left( \frac{d}{dy} (\overline{v}_{,y} \overline{\theta}) + c_{\theta 4} \overline{v}^2 \cdot \Theta' \right) \right] \\ \overline{v\theta} = \frac{-c_{\theta 6}}{\tau^2 c_{\theta 2} c_{\theta 3} (U')^2 - c_{\theta 1}^2} \times \\ \left[ c_{\theta 3} \tau^2 U' \left( \frac{d}{dy} (\overline{u}_{,y} \overline{\theta}) + c_{\theta 4} \overline{u} \overline{v} \cdot \Theta' \right) + c_{\theta 1} \tau \left( \frac{d}{dy} (\overline{v}_{,y} \overline{\theta}) + c_{\theta 4} \overline{v}^2 \cdot \Theta' \right) \right], \end{cases}$$
The coefficients  $c_{\theta 5}$  and  $c_{\theta 6}$  are added to correct the model. Figure 13 compares at  $S_{\theta 1} = 3000$  the above model with the present LFS computations. Also, we have model with the present LFS computations.

The coefficients  $c_{\theta 5}$  and  $c_{\theta 6}$  are added to correct the model. Figure 13 compares at Sc=3000 the above model with the present LES computations. Although some wiggles found in the logarithmic region of the diffusive boundary layer, it clearly shows an improvement in comparison to model (4) for the streamwise component of the Reynolds-flux vector. These wiggles are probably due to the second derivative of the dissipation rate  $\epsilon$  contained in equation (12). The

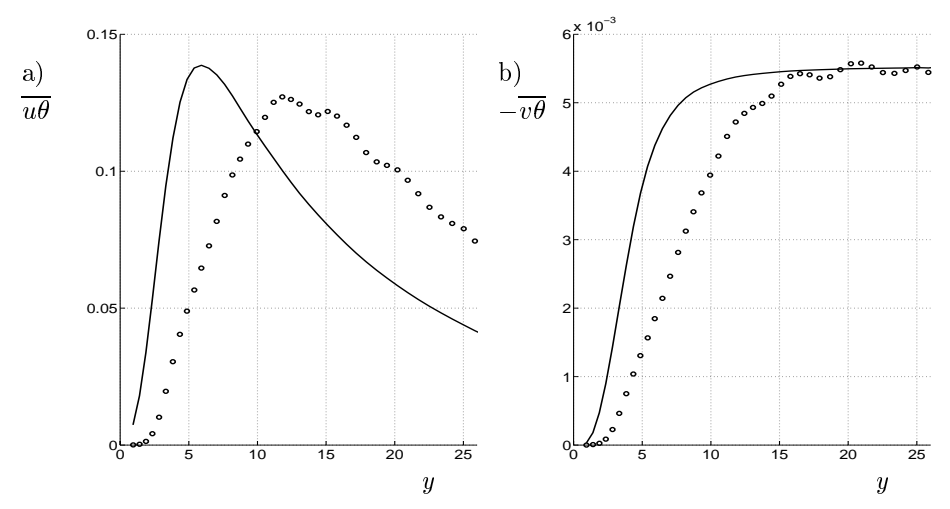


Figure 14. At Sc = 100, model proposed by the present study for  $\overline{u_i\theta}$ . Solid line:  $\overline{u_i\theta}^{\mathrm{LES}}$ .  $\circ \circ \circ : \overline{u_i\theta}^{\mathrm{model}}$ . a)  $i = 1, \ c_{\theta 1} = 380, \ c_{\theta 2} = -3.5, \ c_{\theta 3} = -0.065, \ c_{\theta 4} = 15 \ \mathrm{and} \ c_{\theta 5} = 7.$  b)  $i = 2, \ c_{\theta 1} = 380, \ c_{\theta 2} = -3.5, \ c_{\theta 3} = -0.065, \ c_{\theta 4} = 15 \ \mathrm{and} \ c_{\theta 6} = 0.68.$ 

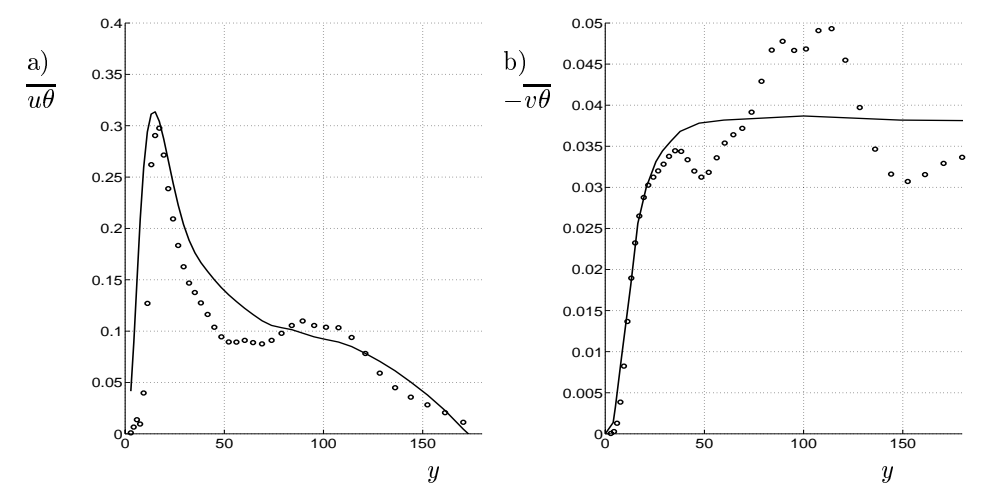


FIGURE 15. At Sc = 1, model proposed by the present study for  $\overline{u_i\theta}$ . Solid line:  $\overline{u_i\theta}^{\rm LES}$ .  $\circ \circ \circ : \overline{u_i\theta}^{\rm model}$ . a) i = 1,  $c_{\theta 1} = 392.8$ ,  $c_{\theta 2} = -3.5$ ,  $c_{\theta 3} = -0.045$ ,  $c_{\theta 4} = 15$  and  $c_{\theta 5} = 8$ . b) i = 2,  $c_{\theta 1} = 392.8$ ,  $c_{\theta 2} = -3.5$ ,  $c_{\theta 3} = -0.045$ ,  $c_{\theta 4} = 15$  and  $c_{\theta 6} = 0.5$ .

good behaviour of equation (12) is also the confirmation that assumption (8), setting that the production rate is negligible at high Schmidt numbers in the budget for the Reynolds-flux vector, is valid.

Figures 14 and 15 show the predictions of the same model at Sc = 1 and 100. At Sc = 1, its behaviour is worse than the previous model but this is not surprising, since it has been developed for a flow at Sc = 3000. Note however, the

relative good result for the streamwise component of the Reynolds-flux vector. On the other hand, it shows a better agreement with LES at Sc = 100, see figures 8 and 14. As shown in figures 13, 14 and 15,  $c_{\theta 2}$  and  $c_{\theta 4}$  are found to be constant, and  $c_{\theta 1}$  and  $c_{\theta 3}$  vary linearly with Schmidt number as following

$$c_{\theta 1}(Sc) = 392.93 - 0.1297 \cdot Sc,$$

$$c_{\theta 3}(Sc) = -0.0448 - 2.02 \times 10^{-4} \cdot Sc.$$

The coefficients of correction,  $c_{\theta 5}$  and  $c_{\theta 6}$ , are found almost constant. In conclusion, the model proposed in the present study seems to be more performant at high Schmidt numbers than the model examined by Wikström *et al.* [22].

In the previous chapter, a simple model for the Reynolds-flux vector has been developed for channel flows at high Schmidt numbers, and has been successfully tested at Sc=100 and 3000. In order to obtain a complete model for the passive-scalar-transfer, one needs a proper boundary condition for  $\Theta$ . Wall-functions have the function of boundary conditions situated at a certain distance from the wall.

At high Schmidt number, although equation (3) does not give a very satisfactory prediction of the streamwise Reynolds-flux, it remains quite useful because it makes the formulation of a more general wall-function for the mean passive scalar possible. If one considers the mass-conservation equation for a fully developed flow, it is obtained

$$\frac{1}{Sc}\frac{\partial\Theta}{\partial y} - \overline{v\theta} = \tau_o,\tag{13}$$

where  $\tau_o = \frac{1}{Sc} (\frac{\partial \Theta}{\partial y})_{wall}$ . Using equation (3), equation (13) becomes

$$\frac{\partial \Theta}{\partial y} = \left(\frac{\partial \Theta}{\partial y}\right)_{wall} - a_{\theta} \cdot k \cdot \tau \frac{\partial \Theta}{\partial y} \quad , \tag{14}$$

where  $a_{\theta}$  is a positive constant, possibly dependent on Schmidt number. One can then derive an integral function for the mean passive scalar as a function of the wall-normal distance

$$\Theta(y_o) = \Theta_{wall} + \left(\frac{\partial \Theta}{\partial y}\right)_{wall} \cdot \int_0^{y_o} \frac{dy}{1 + a_\theta k \tau} . \tag{15}$$

This equation can be integrated in the near-wall region if the Taylor series of the turbulent kinetic energy and the time scale  $\tau$  are considered. It can easily be shown that  $a_{\theta} \cdot k \cdot \tau = A_{\theta}(Sc) \cdot y^4 + O(y^5)$  when the wall is approached. This result is obtained when one considers the limiting behaviour near the wall, of the velocity components and the temperature fluctuations [23]. Equation (15)

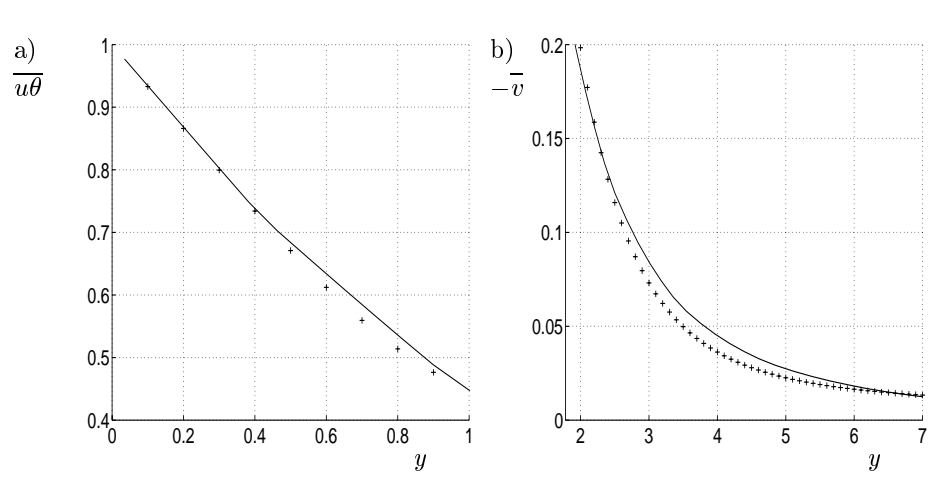


FIGURE 16. At Sc=3000, the mean profile of the passive scalar along the wall-normal distance. Solid line:  $\Theta^{\text{LES}}$ .  $++++:\Theta^{\text{model}}$ . a) In the diffusive and the buffer region.  $A_{\Theta}=3/2$ . b) In the 'logarithmic' region of the diffusive boundary layer.  $A_{\Theta}=0.12$ .

can then be integrated with the help of this approximation, and  $\Theta$  is found as a function of y as follows

$$\Theta(y) = \Theta_{wall} + \frac{(\partial \Theta/\partial y)_{wall}}{A_{\theta}^{1/4} 2\sqrt{2}} \left[ \frac{1}{2} ln \left( \frac{z^2 + z\sqrt{2} + 1}{z^2 - z\sqrt{2} + 1} \right) + arctan \left( \frac{z\sqrt{2}}{1 - z^2} \right) \right], \tag{16}$$

where  $z=yA_{\theta}^{1/4}$ . Using the same methodology, Gersten et al. [25] developed also an analytic solution for the passive scalar but used a different model for the wall-normal component of the Reynolds flux, where  $\overline{v\theta}=-\nu_t\frac{\partial\Theta}{\partial y}$  and the turbulent Schmidt number is considered constant. Since it has been shown previously (see [23]) that  $Sc_t$  is not constant, the present study considers in equation (4)  $\overline{v\theta}=-\alpha_t\frac{\partial\Theta}{\partial y}$ . Equation (16) gives good results in the near-wall region, and surprisingly, even in the logarithmic region of the diffusive boundary layer, provided that another value for  $A_{\theta}$  is chosen, see figure 16. This result tends to prove that the asymptotic behaviour of  $k \cdot \tau$  as  $y^4$  is valid even outside the diffusive sublayer.

#### 4. Conclusions

Large-eddy simulations for turbulent transport of a passive scalar were made at Schmidt numbers equal to 1, 100 and 3000. The flow Reynolds number was 180. The purpose of this work was to provide explicit algebraic models for the Reynolds-flux vector at high Schmidt number.

Two models from previous studies [21, 22] were tested, and one was developed on the basis of a previous work [7] for the budget of the scalar flux. At Sc = 3000

and 100, the model developed in the present study was shown to give better results than the two other models.

At Schmidt number equal to 3000, a wall-function for the mean passive-scalar was developed on the basis of the simplest tested algebraic model [21]. Very good agreement is found with the LES computations. This wall-function can be used with the present model for the Reynolds-flux vector and a low Reynolds  $k - \epsilon$  model, in order to model mass transport at high Schmidt number.

### References

- [1] R.M.C. So and T.P. Sommer, Int. J. Heat Mass Transfer, 39 (1996) 455.
- [2] Y.G. Lai and R.M.C. So, Int. J. Heat Mass Transfer Vol.33 (1990) 1429.
- [3] A. Lai Yoshizawa, J. Fluid Mech. Vol. 195 (1988) 541.
- [4] S. Tavoularis and S. Corrsin, Int. J. Heat Mass Transfer Vol.28 (1985) 265.
- [5] M.M. Rogers, N.N. Mansour and W.C. Reynolds, J. Fluid Mech., 203 (1989) 77
- [6] P.M. Wikström, Measurement, Direct Numerical Simulation and Modelling of Passive Scalar Transport in Turbulent Flows, Doctoral Thesis, ISRN KTH/MEK/TR-98/11-SE (1998), Royal Institute of Technology, Department of Mechanics, S-10044 Stockholm, Sweden.
- [7] F. Gurniki, S. Zahrai and F.H. Bark, On near-wall turbulent passive-scalar transfer at high Schmidt number, Submitted to Journal of Applied Electrochemistry (2000).
- [8] P.R. Spalart, Direct numerical study of leading edge contamination in fluid dynamics of three-dimensional turbulent shear flows and transition, AGARD-CP-438, (1988), pp.5.1-5.13.
- [9] P.R. Spalart & J.H. Watmuff, J. Fluid Mech., 249 (1993) 337.
- [10] S. Berlin, A. Lundbladh & D.S. Henningson, Phys. Fluids, Vol.2 (1994) No.6, 1949.
- [11] F. Gurniki, S. Zahrai and F.H. Bark,  $3^{rd}$  Symposium on Turbulence, Heat and Mass Transfer, Nagoya, april 2-6 2000, Y.Nagano, K.Hanjalić and T.Tsuji (Editors), ©Aichi Shuppan.
- [12] C.S. Lin, R.W. Moulton and G.L. Putnam (1953), Industrial and Engineering Chemistry, Vol.45 No.3, 636
- [13] J.Nordström, N. Nordin and D. Henningson, The fringe technique and the Fourier-method used in the direct numerical simulation of spatially evolving viscous flows, SIAM J. Sci. Comp. 20 (1999), 1365.
- [14] D. Givoli, J. Comp. Phys., 94 (1991) 1.
- [15] S. Zahrai, F.H. Bark and R.I. Karlsson, Eur. J. Mech., B/Fluids, 14 (1995) 459.
- [16] F. Gurniki, S. Zahrai and F.H. Bark, *LES of Turbulent Channel Flow of a Binary Electrode*, accepted for publication in Journal of Applied Electrochemistry (2000).

- [17] Q. Wang & K.D. Squires, Int. J. Multiphase Flow 22 (1996) 667.
- [18] J. K. Ducowicz and J. D. Ramshaw, J. Comput. Phys. 32 (1979) 71.
- [19] B.J. Daly and M.D. Torrey, SOLA-PTS: A transient, three-dimensional alghorithm for fluid-thermal mixing and wall heat transfer in complex geometries NUREG/CR-3822, LA-10132-MS (1984).
- [20] B.P. Leonard, Comput. Meths. Appl. Mech. Eng. 19 (1979) 59.
- [21] P.M. Wikström, M. Hallbäck and A.V. Johansson, Int. J. of Heat and Fluid Flow, 19 (1998) 556.
- [22] P.M. Wikström, S. Wallin and A.V. Johansson, Phys. Fluids, 12 (2000) 688.
- [23] H. Kawamura, K. Ohsaka, H. Abe and K. Yamamoto, Int. J. of Heat and Fluid Flow, 19 (1998) 482.
- [24] T.H. Shih and J.L. Lumley, Mathl. Comput. Modelling, 18 (1993) 9.
- [25] K. Gersten and H. Herwig, Strömungsmechanik, Ed. Vieweg (1992).